

Connectivity of the Outer Plexiform Layer of the Mouse Retina

Dissertation

zur Erlangung des Grades eines
Doktors der Naturwissenschaften

der Mathematisch-Naturwissenschaftlichen Fakultät
und
der Medizinischen Fakultät
der Universität Tübingen

vorgelegt
von
Christian Heinrich Behrens
aus Göttingen
Dezember 2018

Tag der mündlichen Prüfung: 27.05.2019

Dekan der Math.-Nat.-Fakultät: Prof. Dr. Wolfgang Rosenstiel

Dekan der Medizinischen Fakultät: Prof. Dr. Ingo B. Authenrieth

1. Berichterstatter: Prof. Dr. Philipp Berens

2. Berichterstatter: Prof. Dr. Thomas Euler

Prüfungskommission: Prof. Dr. Philipp Berens

Prof. Dr. Thomas Euler

Prof. Dr. Philipp Henning

Prof. Dr. Aristides Arrenberg

Erklärung / Declaration

Ich erkläre, dass ich die zur Promotion eingereichte Arbeit mit dem Titel “Connectivity of the Outer Plexiform Layer of the Mouse Retina” selbständig verfasst, nur die angegebenen Quellen und Hilfsmittel benutzt und wörtlich oder inhaltlich übernommene Stellen als solche gekennzeichnet habe. Ich versichere an Eides statt, dass diese Angaben wahr sind und dass ich nichts verschwiegen habe. Mir ist bekannt, dass die falsche Abgabe einer Versicherung an Eides statt mit Freiheitsstrafe bis zu drei Jahren oder mit Geldstrafe bestraft wird.

I hereby declare that I have produced the work entitled “Connectivity of the Outer Plexiform Layer of the Mouse Retina”, submitted for the award of a doctorate, on my own (without external help), have used only the sources and aids indicated and have marked passages included from other works, whether verbatim or in content, as such. I swear upon oath that these statements are true and that I have not concealed anything. I am aware that making a false declaration under oath is punishable by a term of imprisonment of up to three years or by a fine.

Tübingen, 20. Dezember 2018

Christian Heinrich Behrens

Und doch wäre es, um die notwendige anatomische Grundlage für das Verständnis der physiologischen Vorgänge zu gewinnen, dringend wünschenswert, einmal von irgend einem Organismus das Nervensystem in seiner gesamten Zusammensetzung kennen zu lernen, also in seinen sämtlichen Ganglienzellen, deren Fortsätzen und Verbindungen, den zum Centrum gelangenden und vom Centrum abgehenden Bahnen. (Goldschmidt 1909)

Contents

Synopsis	9
Abstract	11
List of Abbreviations	13
Theoretical background	15
Motivation and aims of the present work	23
Project overview and summary of results	24
Discussion	27
References	32
Statement of Contributions	39
Manuscripts	43
Study A) Connectivity map of bipolar cells and photoreceptors in the mouse retina	45
Study B) Local Signals in Horizontal Cell Dendrites	86
Study C) Connectomics of synaptic microcircuits: lessons from the outer retina	105
Study D) Horizontal cells use different synaptic sites for global and local signaling	113
Acknowledgements	139

Synopsis

Abstract

The retina has two synaptic layers: In the outer plexiform layer (OPL), signals from the photoreceptors (PRs) are relayed to the bipolar cells (BCs) with one type of horizontal cell (HC) as interneuron. In the inner plexiform layer (IPL), the retinal ganglion cells (RGCs) receive input from the bipolar cells, modulated by multiple types of amacrine cells. The axons of the retinal ganglion cells form the optic nerve which transmit the visual signal to the higher regions of the brain (Masland 2012).

Studies of signal processing in the retina usually focus on the inner plexiform layer. Here, the main computations take place such as direction selectivity, orientation selectivity and object motion detection (Gollisch and Meister 2010). However, to fully understand how these computations arise, it is also important to understand how the input to the ganglion cells is computed and thus to understand the functional differences between BC signals. While these are shaped to some extent in the IPL through amacrine cell feedback (Franke et al. 2017), they are also influenced by computations in the OPL (Drinnenberg et al. 2018). Accordingly, it is essential to understand how the bipolar cell signals are formed and what the exact connectivity in the OPL is.

This thesis project aims at a quantitative picture of the mouse outer retina connectome. It takes the approach of systematically analyzing connectivity between the cell types in the OPL based on available high-resolution 3D electron microscopy imaging data (Helmstaedter et al. 2013). We reconstructed photoreceptor axon terminals, horizontal cells and bipolar cells, and quantified their contact statistics. We identified a new structure on HC dendrites which likely defines a second synaptic layer in the OPL below the PRs. Based on the reconstructed morphology, we created a biophysical model of a HC dendrite to gain insights into potential functional mechanisms.

Our results reveal several new connectivity patterns in the mouse OPL and suggest that HCs perform two functional roles at two distinct output sites at the same time. The project emphasizes how large-scale EM data can boost research on anatomical connectivity and beyond and highlights the value of the resulting data for detailed biophysical modeling. Moreover, it shows how the known amount of complexity increases with the level of detail with which we can study a subject. Beyond that, this thesis project demonstrates the benefits of data sharing and open science which only enabled our studies.

List of Abbreviations

AC	amacrine cell
BC	bipolar cell
CBC	cone bipolar cell
CNN	convolutional neural network
EM	electron microscopy
HC	horizontal cell
IPL	inner plexiform layer
OPL	outer plexiform layer
PR	photoreceptor
RBC	rod bipolar cell
RGC	retinal ganglion cell
SBEM	serial block-face electron microscopy
TEM	transmission electron microscopy

Theoretical background

The retina is the first stage of the visual system. It not only transforms light into electrical signals but also already performs complex computations to extract a variety of features from the visual input (Gollisch and Meister 2010). Knowing how the signal is processed in the retina is essential for a full understanding of the visual system and it is a great model system for neural signal processing due to its clear input-output structure. The outer plexiform layer (OPL) is the first synaptic layer along the visual pathway (Fig. 1), so computations here determine everything happening further down stream. Most of the current knowledge about neural connectivity in the outer retina has been acquired through electrophysiological recordings and electron microscopy (EM) images of vertical retinal sections and underlies a trade-off between limited resolution and limited sample size. Thus an exhaustive analysis of OPL connectivity is still missing. In this project we use large scale EM data and biophysical modeling to gain new insights into the structure and function of the OPL in the mouse retina.

Anatomy

The photoreceptors

The mouse has three types of photoreceptors (PR), two types of cone PRs (cones) primarily responsible for higher acuity photopic (daylight) vision and one type of rod PR (rods) primarily responsible for scotopic (low light) vision. The cones divide in 3- 5% short wavelength selective S-cones expressing (only) the UV-sensitive S-opsin and 95% medium wavelength selective M-cones which express the green sensitive M-opsin (Haverkamp et al. 2005). However, in the ventral retina the majority of M-cones co-express S-opsin and are mostly UV sensitive (Baden et al. 2013). Each cone has on average ten ribbon synapses (Tsukamoto et al. 2001) providing input to equally many different CBC types. The rods are also sensitive to green light, but they are specialized for low light vision. They saturate at higher light intensities but recover at

Synopsis

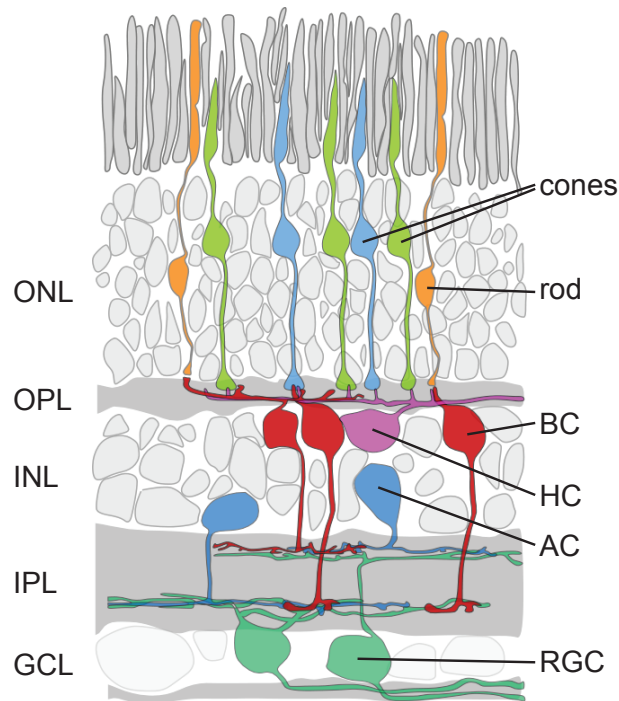


Figure 1: Schematic of a vertical section through the mouse retina.

high photopic light levels (Tikidji-Hamburyan et al. 2017). They outnumber the cones by roughly a factor of 20 (Masland 2012; Behrens et al. 2016), but each rod has only one ribbon synapse and provides input to only one or two BCs.

The bipolar cells

The bipolar cells pick up the signal from the PR and relay it to the IPL, where it is further processed. The mouse has 14 types of BC grouping into 13 types of cone bipolar cells (CBCs) which all get their main input from the cone PR plus one type of rod bipolar cell (RBC) which mainly gets input from rod PR (Euler et al. 2014; Shekhar et al. 2016). The CBCs can again be grouped into five types of OFF-CBCs responding to light offset and eight types of ON-CBCs responding to light onset. The dendritic arbors of bipolar cell form a mosaic with each type uniformly covering the retina (Wässle et al. 2009). The CBCs stratify in five different layers in the IPL. The central ones have more transient response properties while the ones stratifying more towards the boundaries of the IPL have more sustained properties. At their axon terminals where the BCs connect to the retinal ganglion cells, they also receive inhibitory input from amacrine cells further shaping their output signals. There are two known chromatic bipolar cell pathways: The type 9 ON-CBC selectively contacts S-cones while the type 1 OFF-CBC is thought to contact only M-cones (Haverkamp et al. 2005; Breuninger et al. 2011). For the other CBC

no wavelength selectivity is known. The RBC is also an ON BC and its axon terminals stratify below (more or less) all CBC. As the rods developed later evolutionary than the cone pathway in the mammalian retina, the signal from the RBC is picked up in the IPL by the AII amacrine cell and fed into the cone pathway in the IPL (Bloomfield and Dacheux 2001). Besides this primary rod pathway, there are two more: via gap junctions two cones and via certain OFF-CBC types also contacting rods (Euler et al. 2014).

The classical picture of the OPL sees rod and cone pathway rather separated with CBCs primarily involved in daylight vision while RBCs which exclusively get rod input only play a role during scotopic vision. A few years ago, one study showed electrophysiological recordings that hinted at a closer interconnection between rod and cone pathway (Pang et al. 2010). While it had been shown before that some types of OFF-CBCs receive direct input from rods, Pang et al. claim that this holds for some types of ON-CBCs as well. In addition, they find two types of RBCs of which one gets direct input from cone photoreceptors. Both findings had not been confirmed based on anatomy so far.

The horizontal cells

Besides PR and BC dendrites, there is one type of axon bearing horizontal cell as GABAergic interneuron in the mouse OPL. Its dendrites contact the cone pedicle and form a triad with the ON-BC dendritic tips at the cones' ribbon synapse, while the axon contacts rod axon terminals and forms a triad with the RBC dendritic tips. It provides lateral feedback to modulate signaling at the photoreceptor axon terminal (Thoreson and Mangel 2012). As horizontal cells form a strongly electrically coupled network throughout the whole retina, the classical picture sees their functional role in global processing, i.e. for contrast enhancement and adaption to overall light levels. However, recent studies suggest that they might provide local feedback as well (Jackman et al. 2011; Vroman et al. 2014).

Investigating connectivity: Large-scale electron microscopy imaging

Until recently, studying neuronal connectivity was always limited by the trade-off between precision and scale. One common approach is the use of optical imaging combined with fluorescent markers in cells. This can be based on dyes injected in single cells, transgenic mouse lines expressing fluorescent reporter genes, antibodies labelling certain cell types or other sparse staining of cells. While optical imaging

Synopsis

allows analyzing large volumes of tissue, resulting in the high cell count necessary for statistical analysis, its resolution is limited to a few hundred nanometers. Specific synaptic connections usually remain invisible and can only be inferred from proximity. In addition, it requires sparse labeling to be able to distinguish single cells and not for every cell type exists a suitable marker. Hence higher resolution techniques such as electron microscopy (EM) are required in order to allow dense reconstructions of all neurons (Briggman and Denk 2006).

EM techniques, for instance classical transmission EM (TEM), allow high resolution images revealing synaptic connections and even single synaptic vesicles. However, tissue preparation, collection of sections and finally the reconstruction of cells is a cumbersome, time-consuming process which restricts this method to small tissue volumes or low cell counts. In addition, TEM usually reaches a maximum resolution of a few nm only in two dimensions while the section thickness is on the order of 90 nm which can limit reconstruction of fine neuronal structures.

With the development of serial block-face scanning electron microscopy (SBEM, Denk and Horstmann 2004), three-dimensional large-scale high-resolution imaging became available. Compared to TEM at that time, the cutting and scanning process was more automatized, the section alignment became easier and the z-resolution was improved. This type of data is the ideal basis for analyzing connectomics as it contains significant numbers of highly detailed cells including their synaptic connectivity and allowed the discovery of new functional circuits in the retina (Briggman, Helmstaedter, and Denk 2011).

With methods for large scale EM datasets at hand, the limiting problem for connectivity analysis beyond single cells becomes the reconstruction of the cells, specifically the segmentation of the EM data. Reconstructing only a single cell already means coloring the area belonging to this cell in hundreds to thousands of single EM sections while keeping track of each single dendrite or axon. Trading full volume reconstruction for speed, a faster solution is to just trace a skeleton through the cell instead of labeling the whole cell volume. Combined with a consensus approach to circumvent the need of expert tracers, this also allows to distribute the resulting workload (Helmstaedter, Briggman, and Denk 2011). However, with skeletons alone, all contacts must be identified manually as one can't extract contact points between cell volumes. As the datasets contain hundreds to thousands of neurons and thus easily tens of thousands of contacts, this is also prohibitive.

Fully automatic volume segmentation of EM data for neuron reconstruction is a challenging task. While the diameter of dendritic or axonal structures often is on the

order of 100 nm which corresponds to only a few pixels, their total length is many orders of magnitude larger. Small errors on the scale of a few voxels lead to disconnected segments within one neuron. Only recent advances in segmentation algorithms allow at least partially automatic segmentation (Jain, Seung, and Turaga 2010). The first successful approach, given the error rate of available segmentation algorithms was still too high for fully automated segmentation, was to use the skeletonization method (Helmstaedter, Briggman, and Denk 2011) to combine the output segments of the segmentation algorithm presented in Turaga et al. (2010). The resulting publication defines the base for this thesis project: Helmstaedter et al. (2013) recorded an SBEM stack of a $114 \times 80 \mu\text{m}$ piece of mouse retina and densely reconstructed all neurons making connections in the inner plexiform layer.

At that point, in order to simplify automatic reconstruction of cell volumes, a staining of the tissue was used that does not reveal any intracellular structure which also means no synapses. In the meantime, techniques have been further developed to also be applicable to EM with classical staining including e.g. synapses and to further reduce the necessary amount of human labor. This also includes specific algorithms for automatic synapse detection. In addition, developments such as the automated tape ultramicrotron (ATUM, Hayworth et al. 2006; Kasthuri et al. 2015) also allow large scale imaging and reconstruction based on TEM.

Basics of image segmentation and cell reconstruction from EM data

In recent years, (semi-) automated approaches for segmentation of EM data have been developed. A major aim in designing these algorithms is to reduce post-hoc manual corrections to a minimum while maintaining high precision. Post-hoc human correction of errors splitting cells (i.e. joining to segments) is usually much easier than the correction of errors merging two cells, where a new boundary must be defined manually. Therefore, most approaches aim for oversegmentation in the automated part of the reconstruction pipeline.

One segmentation algorithm also used in parts of this thesis project and state of the art at the time comes from Turaga et al. (2010). Its starting point are affinity graphs, a common approach in image segmentation: Each pixel or voxel is defined as a node in an undirected weighted graph. It is connected to each neighboring node and the weights of the edges correspond to the probability of the connected nodes to belong to the same segment. For a perfect separation between segments this would mean that edges between nodes belonging to the same segments are one and edges between nodes

Synopsis

belonging to different segments have a weight of zero. Translated to EM data, this means that all voxels within one cell should be connected to each other with weight one while voxels on the cell boundary are disconnected (edge weight zero).

What is new is the use of a convolutional neural network (CNN) (Turaga et al. 2009) with three hidden layers to generate the edge weights of the affinity graph for all three directions. To train such a network, a certain amount of manually labeled ground truth volume from the same EM stack is required. In this case, cell boundaries are labeled by experts and used to generate the ground truth affinity graphs.

One way to generate a segmentation from the affinity graphs generated by the CNN is to prune them by removing all edges below a certain threshold generate segments with a connected component analysis. This tends to result in undersegmentation as a single edge erroneously above the threshold is sufficient to result in merging segments belonging. A different approach is based on watershed segmentation (Vincent and Soille 1991). Local minima are chosen as seeds and segments are then grown by “flooding” the area around the seeds until either segments meet or a certain threshold is reached. For the affinity graphs, seeds are clusters of nodes interconnected with very high edge values (e.g. >0.999). As this usually leads to oversegmentation it can be combined with other methods to merge the resulting segments (Jain et al. 2011).

In the segmentation algorithm finally used in Helmstaedter et al. (2013), both approaches are combined. First, a watershed segmentation algorithm is used to generate a basic segmentation. This is followed by a two stage merging procedure to reduce oversegmentation. In the first stage, strongly connected segments are merged while in the second stage, small objects are merged with significantly larger ones within certain bounds. For these merging steps, a new affinity graph is computed on this segmentation: The segments correspond to nodes; adjacent segments with a boundary surface above a certain threshold are connected. The weight of the new edges is defined as the average weight of edges connecting the two segments in the voxel based affinity graph. For several merging iterations, connected component analysis is used to merge nodes connected by edges over a certain weight threshold that is gradually lowered, following a recomputation of the affinity graph. To distribute the computational load and to limit the size of the affinity graphs, the dataset is divided into overlapping subcubes for the segmentation. In the end, the final cell volume is computed by gathering all segments that overlap with a manually traced cell skeleton (Helmstaedter, Briggman, and Denk 2011).

To analyze connectivity in the OPL of the dataset from Helmstaedter et al. (2013), we applied the algorithm published together with the dataset and originally trained

specifically on its IPL area to the OPL. Here, the lack of robustness of such a specialized neural network came into play: Although still in the same EM dataset, the quality of the resulting segmentation was worse in the OPL. Potential reasons are the larger volume of single cell segments in the OPL or maybe also slightly different cell boundary contrasts, which led to numerous mergers between large segments. To prevent this, I added an additional constraint in the first merging stage of the segmentation algorithm. In the connected components analysis, the clusters can consist of several dozens of segments of varying sizes. Gathering segments above a certain size is usually well accomplished in the final step based on the cell skeletons. As it is not necessary to go beyond that size when merging segments beforehand, I limited the number of segments per connected component above a size threshold to one. Therefore, whenever more than one segment above that voxel count is in a connected component, the affinity graph of that component is split such that the weights of the cut edges are minimal to divide the segment along the most probable boundary. This effectively reduces the amount of (large) mergers between large diameter dendrites (e.g. horizontal cells near the soma) or photoreceptor axon terminals.

In the meantime, there have been multiple approaches to further improve segmentation algorithms (Zlateski and Seung 2015; Berning, Boergens, and Helmstaedter 2015; Januszewski et al. 2018). While the ultimate goal is a fully automated segmentation, the intermediate objective is to reduce the necessary amount of human labor as far as possible. A side step is taken by the eyewire project (<http://eyewire.org>, Kim et al. 2014). Based on data vastly oversegmented by a combination of a CNN for cell boundary detection and watershed segmentation, crowdsourcing is used to gather the segmentation of the complete cells. With an improved presegmentation and good specialized software for splitting and, this approach can also outperform the skeletonization method depending on the average segment size. The skeletonization based segmentation method has also been improved with better classifiers to work on EM data with conventional staining (SegEM, Berning, Boergens, and Helmstaedter 2015). An additional efficiency gain might be possible by specific algorithm for automated detection of morphological errors (Rolnick et al. 2017).

The most recently published and very promising approach is the segmentation by floodfilling networks (Januszewski et al. 2018). While also based on CNNs, instead of computing an edge classifier on a whole volume, it is done iteratively in small masked subvolumes. Starting from a seed inside a cell, the probability of voxels to belong to the same cell is computed within the field of view (FOV) of the network. Then, the FOV is successively moved within the area of high probability until the whole cell

Synopsis

segment is explored. Repeating this with many seeds within a volume combined with a consensus procedure whenever segmentations starting from different seeds disagree yield an average error-free pathlength as high as 1.1 mm according to the authors.

The final aim is not the volume reconstruction of the cells but the analysis of their connectivity. Given the volume reconstruction of the cells in an EM volume, one can compute all contact surfaces between them. However, identification of functional contacts needs knowledge about the synaptic connectivity. In datasets without intracellular structure, only indirect measures of connectivity such as the contact area can be considered (Helmstaedter et al. 2013; Kim et al. 2014). Another alternative is to use the special morphological structure around certain synapses for additional evidence as we did in the mouse OPL with the synapses at PR axon terminals. Due to limited training data we extracted handcrafted features for all contacts and applied SVM classification on those. For conventionally stained datasets including intracellular structure, there are advances towards automated synapse detection by classification of cell borders (Staffler et al. 2017). This method is also based on a set of handcrafted features extracted from the EM data, but with better suited raw data and – thanks to larger training data – more features and a more advanced classifier.

Biophysical modeling

Neuronal activity can be modelled on vastly different scales and levels of detail: Starting from exact simulations of biochemical processes involved in transmitter release over Hodgkin-Huxley like models incorporating channel dynamics up to simple LNP models or neural network models where each cell is reduced to not much more than a linear filter. Which level of detail is required or possible largely depends on the aims of a modeling project. Modeling detailed biochemical processes is intractable at the scale of a network involving dozens of neurons and the more parameters are involved in a model the more difficult it is to fit it to data and to interpret the contributions of particular parameters. On the other hand, LNP models can't capture and reveal the contribution of structural differences to the functional properties of cell types.

In this thesis project, the approach of relatively detailed multi-compartment models was chosen for modeling the activity of single neurons. When derived from real cell morphologies such as e.g. those recovered from 3D EM data these models allow to study localized signal processing in specific parts of the cell and signal transformation along the neuron. For these models, cell morphologies are converted to a set of electrically coupled compartments representing its structure. For each compartment voltage and calcium signals as well as the influence of different ion channels are modelled.

Besides the morphology, the connectivity between cells (in case of models containing multiple cells) and the way input is provided to the model, the electrical properties (intracellular resistance, membrane resistance and capacitance), the types of ion channels present and their densities on the different cell regions and the synapse types have to be specified. This makes efficient optimization of parameters and fitting the model to data challenging. First, the number of parameters and hence degrees of freedom of the model is on the order of a few dozens. Even if one fixes the majority of parameters to reasonable values based on previous (experimental) knowledge, there remain usually at least about ten parameters which have to be optimized. As the model is also highly non-linear it is a high-dimensional non-convex optimization problem. In addition, the runtime for a single simulation is on the order of a few minutes to half an hour so that running tens of thousands of simulations sequentially is prohibitive.

If functional data is available as it is the case e.g. for bipolar cells from two photon recordings (Franke et al. 2017), it is possible to fit the biophysical models using optimization procedures which efficiently use model runs. Promising approaches to this end are implementations of approximate Bayesian computation and Bayesian optimization (Gutmann and Corander 2016; Lueckmann et al. 2017) although these approaches also struggle with the high number of parameters and the highly nonlinear properties of the models. However, for the HC modeled as part of this thesis there is no experimental data available that allows direct model fits. Therefore, we relied on grid searches using a large CPU cluster to run about 500 simulations in parallel.

For all compartmental models in this thesis project, we opted for using the NeuronC neural circuit simulator (Smith 1992). Its advantage over the more widely used Neuron (Hines and Carnevale 1997) is that it comes with predefined models for all ion channels and synapse types commonly found in the mouse retina. The lacking support of parallelized computations in the simulator can often be compensated by simultaneous model runs.

Motivation and aims of the present work

An ultimate goal in many areas of neuroscience is to build a functional and structural model of the studied systems (Swanson and Lichtman 2016). This holds in particular for the retina which itself is often considered a model system due to its clear input and output structure. A necessary though not sufficient prerequisite for such a model is knowledge about the connectivity of the system (Denk, Briggman, and Helmstaedter 2012; Morgan and Lichtman 2013).

Synopsis

The recent advances in EM imaging and new algorithms for cell reconstructions from imaging data enable more extensive and detailed connectivity studies than ever before. A newly published SBEM dataset which spanned both IPL and OPL but only analyzed IPL connectivity posed a great opportunity to transfer these methods to the OPL.

The aim of this thesis project was to identify the detailed connectivity pattern in the OPL of the mouse retina and to gain insights into the first stage of signal processing in the mouse visual pathway. To this end, we wanted to compile an extensive quantitative connectivity analysis between PRs, BCs and HCs, identify new potential functional pathways. In addition, we wanted to use reconstructed morphologies for biophysical modeling to show potential mechanisms related to these pathways.

Project overview and summary of results

The thesis project consists of four studies that focused on different aspects of connectivity in the mouse OPL and signaling pathways in HC:

- A) Analysis of the connectivity between BCs and PRs, with a focus on the vertical pathway including chromatic channels and interconnections between rod and cone pathways
- B) Study of local signals in mouse HCs based on two-photon calcium imaging, involving biophysical modeling to show how HC morphology supports electrical isolation
- C) Review about connectomics in the outer retina
- D) Analysis of HC connectivity, with a focus on lateral signaling in the OPL and identification of new synaptic structures on HC dendrites

Study A) Connectivity map of bipolar cells and photoreceptors in the mouse retina

The aim of this project was to analyze the connectivity between BC and photoreceptors in mouse outer retina. A special focus was set on chromatic specificity of BCs, i.e. preference for short or medium wavelength sensitive cones as well as on the recently discovered type X CBC. The basis for this and the following connectivity projects was the EM dataset e2006. It was published in Helmstaedter et al. (2013) together with the skeletons of all BC, AC and RGC as well as the algorithms used for volume

reconstruction of neurons. We skeletonized and reconstructed the axon terminals of all cones in the dataset and all rods in half of the dataset and reconstructed the BCs based on the published skeletons. As the subdivision of type 5 BCs in the original publication did not result in proper cell types, we reclassified them along the lines of Greene, Kim, and Seung (2016). Instead of percentiles of the BC density profiles along the light axis, we applied principal component analysis to the density profiles and clustered them using a Gaussian mixture model approach. We ended up with three subtypes named 5T, 5O and 5I which match the properties described by Greene et al. Together with the CBCX they can be mapped to the four BC types 5a-d described by Shekhar et al. (2016).

To quantify the connectivity between BCs and PRs, we developed an automated approach to detect potential synaptic contacts at the PR axon terminals. There are two main problems we had to overcome for this. First, the synapses are not visible in the EM dataset used for this study, so it was necessary to find an alternative approach to distinguish between synaptic contacts and other random contacts between the volumes of two cells. The special morphology at PR-to-BC synapses allowed us to classify them purely based on the morphology. Second, the large number of contacts in the dataset renders manual classification of all contacts prohibitive. To overcome this, we classified a training set of contacts between cones and all BC types manually and then trained a SVM classifier based on a number of spatial and morphological features to automatically classify the majority of contacts. The S-cones in the dataset were identified based on their selective connectivity to type 9 CBC.

Making use of the recent advances in semi-automatic cell reconstruction from large scale EM data, we compiled for the first time a complete quantitative connectivity map of PR and BC in the OPL. Our analysis confirmed the existence of only two color specific BC types 1 (M-cone selective OFF-CBC) and 9 (S-cone selective ON-CBC). All other CBC types contacted both M- and S-cones. The CBCX first identified in this EM dataset has very few contacts to cones compared to all other CBC types. Contacts from CBC8 were also sparse in its dendritic field. However, the overall number of contacts matched the other CBC types due to the large dendritic field of CBC8. We found that a large fraction of the RBC contact cones as well, confirming the finding from Pang et al. but did not find any evidence for two separate RBC types.

Study B) Local Signals in Mouse Horizontal Cell Dendrites

Study B aims at challenging the classical picture of HCs as global feedback interneurons. Recent studies suggest that HCs might also provide local feedback at the cone synapse. While the local dendritic processing necessary for this is a commonly observed

Synopsis

phenomenon in several AC types, it has not been systematically shown in HCs.

The main focus of the study lies on the 2-photon recordings from horizontal cell slices of mice expressing GCaMP3 in HCs conducted by C. Chapot. She measured calcium responses in HC dendrites at the cone axon terminals in response to green, UV and (mouse) white light flashes. The responses show differing chromatic preferences in neighboring HC dendritic tips and hence locally contained signals. Pharmacological experiments indicate that the local HC feedback influences the temporal properties of the cones.

To complement this functional approach, we created a biophysically realistic model of a HC dendritic branch contacting ten cones. The aim was to show based on a model that the existence of localized signals and thus local feedback from HCs to cones and BCs does not require elaborate mechanism but can be replicated in a simple model using only a realistic morphology and known ion channels. Our model showed that L-type Ca^{2+} -channels and K^{+} -channels together with a moderately low membrane resistance are sufficient to reproduce localized signals in HC dendritic tips.

Study C) Connectomics of synaptic microcircuits: lessons from the outer retina

Study C aimed to provide a comprehensive overview on the recent advances and highlights open questions regarding the study of synaptic microcircuits. We discuss the current state of knowledge regarding the connectivity in the outer retina with a focus on our previous study on cone-BC connectivity.

In the last years, new developments in the field of large scale EM imaging opened up new approaches to studying neuronal connectivity. Containing larger ensembles of complete cells, the new datasets simplify the identification of whole circuit motifs. This combination of high resolution imaging and advanced analysis tools allowed the discovery of an increasing amount of circuit complexity in the outer retina. New interconnections between different sub circuits such as rod and cone pathway have been identified. Based on the new findings on the anatomical level, we suggest to experimentally challenge the functional role of these circuit motifs.

Study D) Horizontal cells use different synaptic sites for global and local signaling

With this study, we wanted to complete the analysis of the connectivity in the mouse OPL based on the EM dataset e2006 we started in study A by extending it onto the

horizontal cells to implement the connectivity of the only interneuron in the outer retinal circuitry. Besides the synapse at the cone axon terminals, we focused on newly discovered structures on the HC dendrites which form a potential second synaptic layer in the OPL closer to the INL. This structure consists of thickenings along the HC dendrites which we named bulbs and which contacts both other HCs as well as bipolar cells.

To examine the exact structural connectivity of HC in this dataset, we reconstructed the dendrites of the five HCs that are mostly contained in the EM dataset by manual tracing combined with automatic volume segmentation. HCs contact all cones in their dendritic field with number of contacts and volume contact area per cone decreasing with increasing distance from the HC soma. We confirmed that every BC-cone contact is accompanied by one or two HC-BC contacts at the same dendritic tip. Hence, regarding the number of contacts, HC input to BCs is proportional to cone input to BCs at the cone axon terminal.

Along the main dendrites of the HCs, several μm below the cone axon terminals, we found short segments of increased diameter we named bulbs. About 100 of these are evenly distributed on each HC. All of the bulbs are in contact either with a similar structure of a different HC or with the dendrites of one or two BCs in a way that differs from usual random volume contacts. Supported by immunolabeling and a second EM stack revealing vesicles inside the bulb structures we predict that the bulbs form a second synaptic layer in the OPL as second HC output site. Biophysical modeling of signals in a HC dendrite in response to fullfield and checkerboard noise suggests that at the bulbs HCs provide global feedforward signaling complementing the more localized feedback at the cone synapse.

Discussion

Wrapping up the different studies, my thesis project reveals and anatomically confirms several new connectivity patterns in the mouse outer plexiform layer. It emphasizes how large-scale EM data can boost research on anatomical connectivity and beyond and how known complexity increases with the level of detail with which we can study a subject. For the first time, we compiled an extensive connectivity map between all cell types present in the OPL based on a single consistent dataset. We identified a putative second synaptic output site on HC dendrites, which would imply that HCs perform two functional roles at two distinct output sites at the same time. Last but not least, this thesis project demonstrates the benefits of data sharing and open science. The

Synopsis

studies on OPL connectivity would not have been possible without the publication of the EM dataset e2006 as well as the corresponding algorithms. It maximizes the scientific output from a dataset which was expensive and effortful to acquire while at the same time promoting the techniques which form its basis.

A new level of connectivity analysis from EM

Our studies demonstrate the benefit of advances in imaging techniques as well as segmentation algorithms. Thanks to the recent availability of large-scale high-resolution SBEM data, we now have a single dataset combining superior resolution of 25 nm with a stack size large enough to contain several cells per type (about 30 for the more common CBC types). This allowed us to identify new connectivity patterns which could not be resolved with optical imaging. While optical imaging of immunolabelled CBC8 and cones suggest that CBC8 connect to all cones within their dendritic field, the EM data reveals that cone contacts from CBC8 are more sparse and its dendrites pass below more than half of the cones without making contact.

Beyond the increased resolution, we have the benefit that all cell types can be identified in a single piece of tissue and irrespective of the availability of immunomarkers. This also allowed for the proper classification of CBC 5 subtypes which turned out to be in line with results obtained via transcriptomics (Shekhar et al. 2016) as well as the identification of the CBC X in the original paper which we subsequently characterized regarding its special connectivity in the OPL. In addition, we could present anatomical evidence for a stronger interconnection between rod and cone pathway than commonly thought. We showed direct cone contacts from a majority of RBCs for which there was only physiological evidence so far (Pang et al. 2010).

With the bulb structures observed on horizontal cell signals we identified a putative second synaptic layer in the OPL. Our modeling shows that the signals in bulbs can be expected to be more correlated and dependent on the global component of the input signal as opposed to the more localized signals in dendritic tips. Interneurons performing different tasks sequentially, e.g. rod vision vs. approach detection depending on light conditions for the AII amacrine cell (Münch et al. 2009), or both global and local signaling in one cell type, e.g. in A17 amacrine cells (Hartveit 1999), are well known. However, such a dual function happening simultaneously at distinct output sites in one cell type has so far only been observed for one AC type (Lee et al. 2016; Tien, Kim, and Kerschensteiner 2016). Overall, our studies are in line with other recent studies discovering increasingly complex circuits and structures the "closer" one can look at it.

From anatomy to functional models

This whole thesis project focuses on connectivity as it is identified anatomically. However, the visibility of (synaptic) contacts in the EM data does not necessarily relate to functional relevant connectivity. In particular, when a cell's dendrites contact multiple other cells, it is not clear whether it gets significant input from all of them or at least at the same time. For example, according to our anatomical data, the RBCs get input from on average 30 rods but only from one cone. This does not reveal if the cone contact is functionally relevant or under which light conditions it might play a role. The retina needs to process input varying over a broad spectrum of input characteristics and light levels, which requires adaptation including circuits performing different tasks in different settings (Tikidji-Hamburyan et al. 2015). The existence of mechanisms such as synaptic scaling (Turrigiano 2008) prevents direct conclusions from the number of synapses to the signal strength. Synaptic plasticity can dramatically change the role of existing connections, even at very short time scales (O'Brien 2014; Mercer and Thoreson 2011).

Studying connectivity in an EM stack can be compared to taking a snapshot: One captures the whole anatomy at one fixed point in time and does not take any plasticity events into account. While not observed in the retina, in other brain regions neurons permanently grow and retract dendritic spines throughout their life and thus change their connectivity (Alvarez and Sabatini 2007). On the other hand, this snapshot approach has significant benefits: One can do the whole analysis in one dataset, for one specific mouse and in one specific location on the retina. This has the advantage of consistency within the data compared to studies done on different mouse lines with different immunomarkers for labelling of cell types. At the same time, given the technical advances simplifying future large-scale EM studies, it opens up the possibility of detailed comparative analyses.

Methodological considerations

While the EM dataset used as basis for our studies was the first large-scale high-resolution imaging stack to cover the whole retina from outer nuclear layer to ganglion cell layer, it had the major limitation of missing intracellular structure. The staining of the tissue is done in such a way that plasma-membrane visibility is enhanced in order to simplify tracing of cells and automated reconstructions. This means that synaptic contacts can only be inferred from the surrounding anatomy. While this is reasonably reliable at PR axon terminals due to their special and well known morphology, difficulty

Synopsis

increases for contacts along axons and dendrites as for HC-BC or HC-HC contacts in the OPL or even more for the majority of contacts in the IPL.

One particular limitation which relates to the absence of synaptic structures in the EM dataset is that we did not manage to automatically classify single contact sites at the cone axon terminals. While the specific morphology around those synapses allows reliable manual classification by experts, the limited amount of training data was not sufficient to train advanced algorithms such as a convolutional neural network. Based on a set of handpicked features derived from the cell reconstructions, we could train a SVM classifier to reliably decide whether or not a BC contacts a cone at all, but in the presence of several dendritic tips of one BC it was not possible to train an algorithm to classify each tip separately. This was even more difficult for HC BC contacts at the cone axon terminals.

Another limitation is the size of the EM stack of only $80 \times 140 \mu\text{m}$. Creating large EM stacks is costly and was especially very time consuming at the time of the recording. For small cells like PR and smaller BC types (CBC types 1-7, RBC) the stack size is sufficient to get full reconstructions of tens (BC) or even hundreds (PR) of cells for statistical analysis. However, for larger or rarer BC types (CBC8, CBC9, XBC) or HC this results in only a handful of cells that mostly lie within the EM stack which reduces the statistical power.

For future datasets, both limitations no longer exist or are at least reduced: In the meantime, advances in segmentation algorithms made it feasible to achieve similar or better reconstruction results in conventionally stained tissue (Berning, Boergens, and Helmstaedter 2015; Kornfeld et al. 2017) while also further reducing the necessary amount of human labor. In addition, some of the new algorithms allow the reconstruction of specific cells without the need for complete volume segmentation of the dataset (Januszewski et al. 2018) and also allow the automatic detection of synapses (Staffler et al. 2017). This releases the constraint on the staining of the tissue and makes handling larger datasets possible. On the technical side, current advances in EM technology such as a combination of ATUM and multi-beam scanning EM allow much faster and more reliable recordings of larger EM stacks (Kornfeld and Denk 2018). Another approach, focused ion beam scanning electron microscopy (FIB-SEM, Knott et al. 2008; Xu et al. 2017) further increases the resolution along all axes which helps for both reconstruction accuracy and synapse detection.

Conclusions and future directions

An ultimate goal in the modeling domain is to connect the knowledge of connectivity and morphology with informations about synapses and ion channels from electrophysiology and RNA sequencing (Shekhar et al. 2016) to create a complete functional model of a piece of outer retina or of certain retinal subcircuits. As a result of our connectivity studies we are now equipped with two important ingredients for detailed biophysical models: First, high resolution morphologies which are necessary to properly include anatomical influence such as electrical isolation between different cell regions through thinner and wider dendritic segments. Second, we know the detailed connectivity specifically matching the morphologies so that we can for example place photoreceptors at correct locations and estimate the number of synapses. With the modeling of the horizontal cell dendritic branch for studies B and D, we have shown how this can be used to model locally contained signals due to dendritic isolation. However, there is even more potential for biophysical modeling of BCs: In contrast to the horizontal cells, there is more functional data for BCs and more is known about their ion channels e.g. from electrophysiological recordings (Ivanova and Müller 2006; Hellmer et al. 2016). Both are needed for accurately tuned models. One potential follow-up project could be to study the origins of BC type differences on this level. Another interesting direction would be to include ACs and study the effect of feedback for the BC signal for example with respect to differential signaling in different axonal tips of a single BC.

A project that emerged from the work with both EM reconstructions of BCs and biophysical models is to model extracellular electrical stimulation of BCs as it is done by retinal implants (Zrenner 2002). The aim of this ongoing project is to set up biophysically realistic models as a test platform for new stimulation protocols for retinal implants. This allows rapid testing and optimization of stimuli with the aim of better differential stimulation of individual cell types or at least ON- vs. OFF-BCs. Another potential follow-up project to the studies in this thesis which follows this direction would be biophysical modeling of the different BC types to study if and how the functional type differences relate to morphological differences or if they are rather based on differences in ion channel types and density. Starting from the horizontal cell model developed as part of this thesis project, one could look further into HC functions by modeling how the surround of cone photoreceptors and BCs is influenced by horizontal cells.

One major advance for all connectivity studies as well as for the identification of functional sub circuits in the mouse retina would be a new, larger EM dataset with conventional staining. First, this would allow identifying synapses which results in a much clearer distinction between functional relevant contacts and random contacts

Synopsis

between cell volumes. The connectivity analysis in the OPL would already benefit a lot from this as it would potentially be possible to automatically classify single BC-cone contacts or better quantify connectivity at the HC bulbs. In the IPL, the advantage becomes even larger as the morphology around the synaptic contacts is much less distinct than at the cone or rod axon terminals. Second, a larger EM stack would allow for more completely reconstructed cells per cell type or, especially in the IPL, where cells of certain types could not be completely reconstructed in the e2006 dataset at all. This would dramatically increase statistic power for the analysis of larger cell types.

Another interesting direction for connectivity analyses which become tractable thanks to faster and cheaper recording and reconstruction techniques are comparative studies. EM stacks from different retinal locations could reveal differences in morphology and wiring across the retina and stacks from different mouse lines (e.g. disease model vs. wild-type) could further advance the understanding of anatomical changes following e.g. PR degeneration.

On the experimental side, it would be an interesting follow-up to uncover the true functional role of the newly identified connectivity patterns. Therefore, it is required to go beyond the anatomical level and record functional data for example using two-photon techniques. Potential projects emerging from study A could focus on uncovering the role of cone RBC connections or recordings from CBCX using a mouse line which expresses marker proteins in this cell type to uncover functional implications of its unusual OPL connectivity. Further insight into the role of HC bulb connectivity could be gained by functional recordings from HC dendrites using voltage or calcium sensors.

In sum, high complexity remains a major challenge both for the experimental and for the biophysical modeling approach. Biophysical modeling can support the development of comprehensive functional models of neural processing through generating hypothetical biologically plausible models of biological networks, which can then be tested specifically. While modeling allows reproducing biological functions at a detailed level, it comes with a large amount of parameters that have to be specified. With actual functional recordings available for model fitting, biophysical models can be further improved and fine-tuned. At the same time, biophysical models can support the interpretation of functional experimental data and thereby promote the understanding of neural processing.

References

- Alvarez, Veronica A., and Bernardo L. Sabatini. 2007. "Anatomical and Physiological Plasticity of Dendritic Spines." *Annual Review of Neuroscience* 30 (1): 79–97. doi:10.1146/annurev.neuro.30.051606.094222.
- Baden, Tom, Timm Schubert, Le Chang, Tao Wei, Mariana Zaichuk, Bernd Wissinger, and Thomas Euler. 2013. "A Tale of Two Retinal Domains: Near-Optimal Sampling of Achromatic Contrasts in Natural Scenes through Asymmetric Photoreceptor Distribution." *Neuron* 80 (5): 1206–1217. doi:10.1016/j.neuron.2013.09.030.
- Behrens, Christian, Timm Schubert, Silke Haverkamp, Thomas Euler, and Philipp Berens. 2016. "Connectivity map of bipolar cells and photoreceptors in the mouse retina." *eLife* 5:065722. doi:10.7554/eLife.20041.
- Berning, Manuel, Kevin M. Boergens, and Moritz Helmstaedter. 2015. "SegEM: Efficient Image Analysis for High-Resolution Connectomics." *Neuron* 87 (6): 1193–1206. doi:10.1016/j.neuron.2015.09.003.
- Bloomfield, Stewart A., and Ramon F. Dacheux. 2001. "Rod Vision: Pathways and Processing in the Mammalian Retina." *Progress in Retinal and Eye Research* 20 (3): 351–384. doi:10.1016/S1350-9462(00)00031-8.
- Breuninger, Tobias, Christian Puller, Silke Haverkamp, and Thomas Euler. 2011. "Chromatic bipolar cell pathways in the mouse retina." *The Journal of neuroscience : the official journal of the Society for Neuroscience* 31 (17): 6504–6517. doi:10.1523/JNEUROSCI.0616-11.2011.
- Briggman, Kevin L., and Winfried Denk. 2006. "Towards neural circuit reconstruction with volume electron microscopy techniques." *Current Opinion in Neurobiology* 16 (5): 562–570. doi:10.1016/j.conb.2006.08.010.
- Briggman, Kevin L., Moritz Helmstaedter, and Winfried Denk. 2011. "Wiring specificity in the direction-selectivity circuit of the retina." *Nature* 471 (7337): 183–190. doi:10.1038/nature09818.
- Denk, Winfried, Kevin L Briggman, and Moritz Helmstaedter. 2012. "Structural neurobiology: missing link to a mechanistic understanding of neural computation." *Nature Reviews Neuroscience* 13 (5): 351–8. doi:10.1038/nrn3169.
- Denk, Winfried, and Heinz Horstmann. 2004. "Serial block-face scanning electron microscopy to reconstruct three-dimensional tissue nanostructure." *PLoS Biology* 2 (11). doi:10.1371/journal.pbio.0020329.

References

- Drinnenberg, Antonia, Felix Franke, Rei K Morikawa, Josephine Jüttner, Daniel Hillier, Peter Hantz, Andreas Hierlemann, Rava Azeredo da Silveira, and Botond Roska. 2018. "How Diverse Retinal Functions Arise from Feedback at the First Visual Synapse." *Neuron* 99 (1): 117–134.e11. doi:10.1016/j.neuron.2018.06.001.
- Euler, Thomas, Silke Haverkamp, Timm Schubert, and Tom Baden. 2014. "Retinal bipolar cells: elementary building blocks of vision." *Nature Reviews Neuroscience* 15 (8): 507–519. doi:10.1038/nrn3783.
- Franke, Katrin, Philipp Berens, Timm Schubert, Matthias Bethge, Thomas Euler, and Tom Baden. 2017. "Inhibition decorrelates visual feature representations in the inner retina." *Nature* 542 (7642): 439–444. doi:10.1038/nature21394. arXiv: 15334406.
- Goldschmidt, Richard Benedikt. 1909. "Das Nervensystem von *Ascaris lumbricoides* und *megaloccephala*." *Zeitschrift für wissenschaftliche Zoologie* 92:306–358.
- Gollisch, Tim, and Markus Meister. 2010. "Eye smarter than scientists believed: neural computations in circuits of the retina." *Neuron* 65 (2): 150–64. doi:10.1016/j.neuron.2009.12.009.
- Greene, Matthew J., Jinseop S. Kim, and H. Sebastian Seung. 2016. "Analogous Convergence of Sustained and Transient Inputs in Parallel On and Off Pathways for Retinal Motion Computation." *Cell Reports* 14 (8): 1892–1900. doi:10.1016/j.celrep.2016.02.001.
- Gutmann, Michael U., and Jukka Corander. 2016. "Bayesian Optimization for Likelihood-Free Inference of Simulator-Based Statistical Models." *Journal of Machine Learning Research* 17 (125): 1–47. doi:arXiv:1501.03291v3. arXiv: 1501.03291.
- Hartveit, Espen. 1999. "Reciprocal Synaptic Interactions Between Rod Bipolar Cells and Amacrine Cells in the Rat Retina." *Journal of Neurophysiology* 81 (6): 2923–2936. doi:10.1152/jn.1999.81.6.2923.
- Haverkamp, Silke, Heinz Wässle, Jens Duebel, Thomas Kuner, George J Augustine, Guoping Feng, and Thomas Euler. 2005. "The primordial, blue-cone color system of the mouse retina." *The Journal of neuroscience : the official journal of the Society for Neuroscience* 25 (22): 5438–5445. doi:10.1523/JNEUROSCI.1117-05.2005.
- Hayworth, KJ, N Kasthuri, R Schalek, and JW Lichtman. 2006. "Automating the Collection of Ultrathin Serial Sections for Large Volume TEM Reconstructions." *Microscopy and Microanalysis* 12 (S02): 86–87. doi:10.1017/S1431927606066268.
- Hellmer, C. B., Y. Zhou, B. Fyk-Kolodziej, Z. Hu, and T. Ichinose. 2016. "Morphological and physiological analysis of type-5 and other bipolar cells in the Mouse Retina." *Neuroscience* 315:246–258. doi:10.1016/j.neuroscience.2015.12.016.
- Helmstaedter, Moritz, Kevin L Briggman, and Winfried Denk. 2011. "High-accuracy neurite reconstruction for high-throughput neuroanatomy." *Nature neuroscience* 14 (8): 1081–1088. doi:10.1038/nn.2868.

- Helmstaedter, Moritz, Kevin L Briggman, Srinivas C Turaga, Viren Jain, H Sebastian Seung, and Winfried Denk. 2013. "Connectomic reconstruction of the inner plexiform layer in the mouse retina." *Nature* 500 (7461): 168–74. doi:10.1038/nature12346.
- Hines, M L, and N T Carnevale. 1997. "The NEURON simulation environment." *Neural computation* 9 (6): 1179–209.
- Ivanova, Elena, and Frank Müller. 2006. "Retinal bipolar cell types differ in their inventory of ion channels." *Visual Neuroscience* 23 (2): 143–154. doi:10.1017/S0952523806232048.
- Jackman, Skyler L., Norbert Babai, James J. Chambers, Wallace B. Thoreson, and Richard H. Kramer. 2011. "A positive feedback synapse from retinal horizontal cells to cone photoreceptors." *PLoS Biology* 9 (5). doi:10.1371/journal.pbio.1001057.
- Jain, Viren, H Sebastian Seung, and Srinivas C Turaga. 2010. "Machines that learn to segment images: a crucial technology for connectomics." *Current Opinion in Neurobiology* 20 (5): 653–666. doi:10.1016/j.conb.2010.07.004.
- Jain, Viren, Srinivas C Turaga, K Briggman, Moritz N Helmstaedter, Winfried Denk, and H Sebastian Seung. 2011. "Learning to Agglomerate Superpixel Hierarchies." *Advances in Neural Information Processing Systems*: 648–656.
- Januszewski, Michał, Jörgen Kornfeld, Peter H. Li, Art Pope, Tim Blakely, Larry Lindsey, Jeremy Maitin-Shepard, Mike Tyka, Winfried Denk, and Viren Jain. 2018. "High-precision automated reconstruction of neurons with flood-filling networks." *Nature Methods* 15 (August): 1–6. doi:10.1038/s41592-018-0049-4.
- Kasthuri, Narayanan, Kenneth Jeffrey Hayworth, Daniel Raimund Berger, Richard Lee Schalek, José Angel Conchello, Seymour Knowles-Barley, Dongil Lee, et al. 2015. "Saturated Reconstruction of a Volume of Neocortex." *Cell* 162 (3): 648–661. doi:10.1016/j.cell.2015.06.054.
- Kim, Jinseop S, Matthew J Greene, Aleksandar Zlateski, Kisuk Lee, Mark Richardson, Srinivas C Turaga, Michael Purcaro, et al. 2014. "Space-time wiring specificity supports direction selectivity in the retina." *Nature* 509 (7500): 331–6. doi:10.1038/nature13240.
- Knott, G., H. Marchman, D. Wall, and B. Lich. 2008. "Serial Section Scanning Electron Microscopy of Adult Brain Tissue Using Focused Ion Beam Milling." *Journal of Neuroscience* 28 (12): 2959–2964. doi:10.1523/JNEUROSCI.3189-07.2008.
- Kornfeld, Jörgen, Sam E. Benezra, Rajeevan T. Narayanan, Fabian Svara, Robert Egger, Marcel Oberlaender, Winfried Denk, and Michael A. Long. 2017. "EM connectomics reveals axonal target variation in a sequence-generating network." *eLife* 6:1–20. doi:10.7554/eLife.24364.
- Kornfeld, Jörgen, and Winfried Denk. 2018. "Progress and remaining challenges in high-throughput volume electron microscopy." *Current Opinion in Neurobiology* 50:261–267. doi:10.1016/j.conb.2018.04.030.

References

- Lee, Seunghoon, Yi Zhang, Minggang Chen, and Z. Jimmy Zhou. 2016. "Segregated Glycine-Glutamate Co-transmission from vGluT3 Amacrine Cells to Contrast-Suppressed and Contrast-Enhanced Retinal Circuits." *Neuron* 90 (1): 27–34. doi:10.1016/j.neuron.2016.02.023.
- Lueckmann, Jan-Matthis, Pedro J. Goncalves, Giacomo Bassetto, Kaan Öcal, Marcel Nonnenmacher, and Jakob H. Macke. 2017. "Flexible statistical inference for mechanistic models of neural dynamics." *Advances in Neural Information Processing Systems* 30: 1289–1299. doi:Centrodedocumentación:INPA-Investigación. arXiv: 1711.01861.
- Masland, Richard H. 2012. "The neuronal organization of the retina." *Neuron* 76 (2): 266–80. doi:10.1016/j.neuron.2012.10.002.
- Mercer, Aaron J., and Wallace B. Thoreson. 2011. "The dynamic architecture of photoreceptor ribbon synapses: Cytoskeletal, extracellular matrix, and intramembrane proteins." *Visual Neuroscience* 28 (06): 453–471. doi:10.1017/S0952523811000356. arXiv: NIHMS150003.
- Morgan, Joshua L, and Jeff W Lichtman. 2013. "Why not connectomics?" *Nature Methods* 10 (6): 494–500. doi:10.1038/nmeth.2480.
- Münch, Thomas A., Rava Azeredo Da Silveira, Sandra Siegert, Tim James Viney, Gautam B. Awatramani, and Botond Roska. 2009. "Approach sensitivity in the retina processed by a multifunctional neural circuit." *Nature Neuroscience* 12 (10): 1308–1316. doi:10.1038/nn.2389.
- O'Brien, John. 2014. "The ever-changing electrical synapse." *Current Opinion in Neurobiology* 29:64–72. doi:10.1016/j.conb.2014.05.011. arXiv: NIHMS150003.
- Pang, J.-J., F. Gao, J. Lem, D. E. Bramblett, D. L. Paul, and S. M. Wu. 2010. "Direct rod input to cone BCs and direct cone input to rod BCs challenge the traditional view of mammalian BC circuitry." *Proceedings of the National Academy of Sciences* 107 (1): 395–400. doi:10.1073/pnas.0907178107.
- Rolnick, David, Yaron Meirovitch, Toufiq Parag, Hanspeter Pfister, Viren Jain, Jeff W. Lichtman, Edward S. Boyden, and Nir Shavit. 2017. "Morphological Error Detection in 3D Segmentations": 1–13. arXiv: 1705.10882.
- Shekhar, Karthik, Sylvain W. Lapan, Irene E. Whitney, Nicholas M. Tran, Evan Z. Macosko, Monika Kowalczyk, Xian Adiconis, et al. 2016. "Comprehensive Classification of Retinal Bipolar Neurons by Single-Cell Transcriptomics." *Cell* 166 (5): 1308–1323.e30. doi:10.1016/j.cell.2016.07.054.
- Smith, Robert G. 1992. "NeuronC: a computational language for investigating functional architecture of neural circuits." *Journal of neuroscience methods* 43 (2-3): 83–108. doi:10.1016/0165-0270(92)90019-A.
- Staffler, Benedikt, Manuel Berning, Kevin M. Boergens, Anjali Gour, Patrick van der Smagt, and Moritz Helmstaedter. 2017. "SynEM, automated synapse detection for connectomics." *eLife* 6:1–25. doi:10.7554/eLife.26414.

- Swanson, Larry W., and Jeff W. Lichtman. 2016. "From Cajal to Connectome and Beyond." *Annual Review of Neuroscience* 39 (1): 197–216. doi:10.1146/annurev-neuro-071714-033954. arXiv: arXiv:1011.1669v3.
- Thoreson, Wallace B., and Stuart C. Mangel. 2012. "Lateral interactions in the outer retina." *Progress in Retinal and Eye Research* 31 (5): 407–441. doi:10.1016/j.preteyeres.2012.04.003. arXiv: NIHMS150003.
- Tien, Nai Wen, Tahnbee Kim, and Daniel Kerschensteiner. 2016. "Target-Specific Glycinergic Transmission from VGlut3-Expressing Amacrine Cells Shapes Suppressible Contrast Responses in the Retina." *Cell Reports* 15 (7): 1369–1375. doi:10.1016/j.celrep.2016.04.025. arXiv: 15334406.
- Tikidji-Hamburyan, Alexandra, Katja Reinhard, Hartwig Seitter, A Hovhannisyann, C A Procyk, A E Allen, M Schenk, R J Lucas, and Thomas A. Münch. 2015. "Retinal output changes qualitatively with every change in ambient illuminance." *Nat Neurosci* 18 (1): 66–74. doi:10.1038/nn.3891.
- Tikidji-Hamburyan, Alexandra, Katja Reinhard, Riccardo Storchi, Johannes Dietter, Hartwig Seitter, Katherine E. Davis, Saad Idrees, et al. 2017. "Rods progressively escape saturation to drive visual responses in daylight conditions." *Nature Communications* 8 (1). doi:10.1038/s41467-017-01816-6.
- Tsukamoto, Y, K Morigiwa, M Ueda, and Peter Sterling. 2001. "Microcircuits for night vision in mouse retina." *The Journal of neuroscience : the official journal of the Society for Neuroscience* 21 (21): 8616–8623. doi:21/21/8616 [pii].
- Turaga, Srinivas C, Kevin L Briggman, Moritz Helmstaedter, Winfried Denk, and H Sebastian Seung. 2009. "Maximin affinity learning of image segmentation." *Advances in Neural Information Processing Systems* 22: 1865–1873. arXiv: 0911.5372.
- Turaga, Srinivas C, Joseph F Murray, Viren Jain, Fabian Roth, Moritz Helmstaedter, Kevin Briggman, Winfried Denk, and H Sebastian Seung. 2010. "Convolutional Networks Can Learn to Generate Affinity Graphs for Image Segmentation." *Neural Computation* 22 (2): 511–538. doi:10.1162/neco.2009.10-08-881.
- Turrigiano, Gina G. 2008. "The Self-Tuning Neuron: Synaptic Scaling of Excitatory Synapses." *Cell* 135 (3): 422–435. doi:10.1016/j.cell.2008.10.008. arXiv: arXiv:1011.1669v3.
- Vincent, L., and P. Soille. 1991. "Watersheds in digital spaces: an efficient algorithm based on immersion simulations." *IEEE Transactions on Pattern Analysis and Machine Intelligence* 13 (6): 583–598. doi:10.1109/34.87344.
- Vroman, Rozan, Lauw J. Klaassen, Marcus H.C. Howlett, Valentina Cenedese, Jan Klooster, Trijntje Sjoerdsma, and Maarten Kamermans. 2014. "Extracellular ATP Hydrolysis Inhibits Synaptic Transmission by Increasing pH Buffering in the Synaptic Cleft." *PLoS Biology* 12 (5). doi:10.1371/journal.pbio.1001864.

References

- Wässle, Heinz, Christian Puller, Frank Müller, and Silke Haverkamp. 2009. "Cone contacts, mosaics, and territories of bipolar cells in the mouse retina." *The Journal of neuroscience : the official journal of the Society for Neuroscience* 29 (1): 106–117. doi:10.1523/JNEUROSCI.4442-08.2009.
- Xu, C. Shan, Kenneth J. Hayworth, Zhiyuan Lu, Patricia Grob, Ahmed M. Hassan, José G. García-Cerdán, Krishna K. Niyogi, Eva Nogales, Richard J. Weinberg, and Harald F. Hess. 2017. "Enhanced FIB-SEM systems for large-volume 3D imaging." *eLife* 6:1–36. doi:10.7554/eLife.25916.
- Zlateski, Aleksandar, and H. Sebastian Seung. 2015. "Image Segmentation by Size-Dependent Single Linkage Clustering of a Watershed Basin Graph." arXiv: 1505.00249.
- Zrenner, Eberhart. 2002. "Will Retinal Implants Restore Vision?" *Science* 295 (5557): 1022–1025. doi:10.1126/science.1067996.

Statement of Contributions

Study A) Connectivity map of bipolar cells and photoreceptors in the mouse retina

Behrens C, Schubert T, Haverkamp S, Euler T, Berens P. Connectivity map of bipolar cells and photoreceptors in the mouse retina. *eLife* 2016;5:e20041.2016;5:e20041
<http://doi.org/10.7554/eLife.20041>

Christian Behrens and Timm Schubert are joint first authors of this study. The study was designed by Philipp Berens, Thomas Euler, Silke Haverkamp and Timm Schubert. **Christian Behrens** and Timm Schubert did the anatomical tracing and classified contact sites. **Christian Behrens** did the programming and analyzed the data with input from Philipp Berens, Thomas Euler and Timm Schubert. **Christian Behrens**, Philipp Berens, Thomas Euler and Timm Schubert interpreted the data. **Christian Behrens**, Philipp Berens, Thomas Euler and Timm Schubert drafted and revised the manuscript with contributions from Silke Haverkamp.

Study B) Local Signals in Horizontal Cell Dendrites

Chapot CA, Behrens C, Rogerson LE, Baden T, Pop S, Berens P, Euler T, Schubert T (2017). Local Signals in Horizontal Cell Dendrites. *Current Biology* 27(23):3603-3615.e5.
<https://doi.org/10.1016/j.cub.2017.10.050>

Camille A. Chapot, Timm Schubert and Thomas Euler designed the study. Camille A. Chapot and Sinziana Pop established the experimental approach. Camille A. Chapot performed experiments and pre-processing. Camille A. Chapot analyzed the data with input from Timm Schubert, Tom Baden, Luke E. Rogerson, Philipp Berens and Thomas Euler. **Christian Behrens** generated and analyzed the model with input from Timm Schubert, Philipp Berens and Thomas Euler. Camille A. Chapot, Timm Schubert, Thomas Euler and Luke E. Rogerson wrote the manuscript with input from Philipp Berens, **Christian Behrens** and Tom Baden.

Study C) Connectomics of synaptic microcircuits: lessons from the outer retina

Rogerson LE, Behrens C, Euler T, Berens P, Schubert T (2017). Connectomics of synaptic microcircuits: lessons from the outer retina. *Journal of Physiology* 292(16):5517-5524.
<http://doi.org/10.1113/JP273671>

This review was written for a special issue for the symposium “Phototransduction and synaptic transmission” which took place at the Phototransduction UK workshop,

Statement of Contributions

Sheffield, 31 August – 2 September 2016. **Christian Behrens** and Luke E. Rogerson are joint first authors of this review. The manuscript was drafted and revised by **Christian Behrens**, Luke E. Rogerson and Timm Schubert with input from Philipp Berens and Thomas Euler.

Study D) Horizontal cells use different synaptic sites for global and local signaling

Behrens C, Zhang Y, Yadav S, Haverkamp S, Korympidou MM, Schaedler A, Dedek K, Smith RG, Euler T, Berens P, Schubert T. Horizontal cells use different synaptic sites for global and local signaling. *Manuscript in prep.*

This study was designed by Philipp Berens, Thomas Euler and Timm Schubert. **Christian Behrens**, Timm Schubert and Yue Zhang did the anatomical tracing and identified contacts. **Christian Behrens** did the programming and **Christian Behrens** and Timm Schubert analyzed the data with input from Philipp Berens and Thomas Euler. Maria M. Korympidou, Anna Schaedler und Timm Schubert did immunolabeling for SNAP25. Karin Dedek and Shubhash C. Yadav did HC single cell injections and immunolabeling for glutamate receptor subunit GluR4 and GABA receptor subunit gamma 2. Silke Haverkamp and Stephan Irsen recorded the serial section EM. **Christian Behrens** built the biophysical model with input from Philipp Berens, Timm Schubert and Robert G Smith. **Christian Behrens** and Timm Schubert wrote the manuscript with input from Philipp Berens and Thomas Euler.

Manuscripts



Connectivity map of bipolar cells and photoreceptors in the mouse retina

Christian Behrens^{1,2,3,4†}, Timm Schubert^{1,2†}, Silke Haverkamp⁵, Thomas Euler^{1,2,3}, Philipp Berens^{1,2,3*}

¹Institute for Ophthalmic Research, University of Tübingen, Tübingen, Germany;

²Center for Integrative Neuroscience, University of Tübingen, Tübingen, Germany;

³Bernstein Center for Computational Neuroscience, University of Tübingen,

Tübingen, Germany; ⁴Graduate Training Center for Neuroscience, International Max Planck Research School, University of Tübingen, Tübingen, Germany; ⁵Institute of Cellular and Molecular Anatomy, Goethe-University Frankfurt, Frankfurt, Germany

Abstract In the mouse retina, three different types of photoreceptors provide input to 14 bipolar cell (BC) types. Classically, most BC types are thought to contact all cones within their dendritic field; ON-BCs would contact cones exclusively via so-called invaginating synapses, while OFF-BCs would form basal synapses. By mining publicly available electron microscopy data, we discovered interesting violations of these rules of outer retinal connectivity: ON-BC type X contacted only ~20% of the cones in its dendritic field and made mostly atypical non-invaginating contacts. Types 5T, 5O and 8 also contacted fewer cones than expected. In addition, we found that rod BCs received input from cones, providing anatomical evidence that rod and cone pathways are interconnected in both directions. This suggests that the organization of the outer plexiform layer is more complex than classically thought.

DOI: [10.7554/eLife.20041.001](https://doi.org/10.7554/eLife.20041.001)

*For correspondence: philipp.berens@uni-tuebingen.de

†These authors contributed equally to this work

Competing interests: The authors declare that no competing interests exist.

Funding: See page 18

Received: 25 July 2016

Accepted: 21 November 2016

Published: 25 November 2016

Reviewing editor: Fred Rieke, Howard Hughes Medical Institute, University of Washington, United States

© Copyright Behrens et al. This article is distributed under the terms of the [Creative Commons Attribution License](https://creativecommons.org/licenses/by/4.0/), which permits unrestricted use and redistribution provided that the original author and source are credited.

Introduction

Parallel visual processing already starts at the very first synapse of the visual system, where photoreceptors distribute the signal onto multiple types of bipolar cells. In the mouse retina, two types of cone photoreceptors differing in their spectral properties – short (S-) and medium wavelength-sensitive (M-) cones – and rod photoreceptors provide input to 14 types of bipolar cell (reviewed in Euler et al., 2014). The precise connectivity rules between photoreceptors and bipolar cell (BC) types determine which signals are available to downstream circuits. Therefore, the connectome of the outer retina is essential for a complete picture of visual processing in the retina.

For some mouse BC types, specific connectivity patterns have already been described: For example, based on electrical recordings and immunohistochemistry cone bipolar cell type 1 (CBC1) have been suggested to selectively contact M-cones, whereas CBC9 exclusively contacts S-cones (Haverkamp et al., 2005; Breuninger et al., 2011). The other BC types are thought to contact all M-cones within their dendritic field, but their connectivity to S-cones is unclear (Wässle et al., 2009). In addition, two fundamental cone-BC contact shapes have been described: invaginating contacts with the dendritic tips extending into the cone pedicle and flat (basal) contacts that touch the cone pedicle base, commonly associated with ON- and OFF-BCs, respectively (Dowling and Boycott, 1966; Kolb, 1970; Hopkins and Boycott, 1995).

Rod bipolar cells (RBCs) are thought to exclusively receive rod input and to feed this signal into the cone pathway via All amacrine cells (reviewed by Bloomfield and Dacheux, 2001). However, physiological data indicate that RBCs may receive cone photoreceptor input as well (Pang et al., 2010). Also, types CBC3A, CBC3B and CBC4 have been reported to receive direct rod input

(Mataruga et al., 2007; Haverkamp et al., 2008; Tsukamoto and Omi, 2014), suggesting that rod and cone pathways are much more interconnected than their names implicate.

Here, we analyzed an existing electron microscopy dataset (Helmstaedter et al., 2013) to quantify the connectivity between photoreceptors and bipolar cells in the mouse. We did not find evidence for additional M- or S-cone selective CBC types in addition to the reported CBC1 and 9. However, we found interesting violations of established rules of outer retinal connectivity: The newly discovered CBCX (Helmstaedter et al., 2013), likely an ON-CBC (Ichinose et al., 2014), had unexpectedly few and mostly atypical basal contacts to cones. CBC5T, CBC5O and CBC8 also contacted fewer cones than expected from their dendritic field. In addition, we provide anatomical evidence that rod and cone pathways are connected in both directions: Not only OFF-types CBC3A, CBC3B and CBC4 get direct input from rods but also RBCs from cones.

Results

Identification of S- and M-cones

We used the serial block-face electron microscopy (SBEM) dataset e2006 published by Helmstaedter et al. (2013) to analyze the connectivity between photoreceptors and bipolar cells in the outer plexiform layer (OPL) of the mouse retina (Figure 1A). To this end, we reconstructed the volume of all cone axon terminals (cone pedicles; $n = 163$) in the dataset as well as the dendritic trees of all BCs ($n = 451$; Figure 1B, see Materials and methods).

To identify S- and M-cones, we used the fact that type nine cone bipolar cells selectively target S-cones (Figure 1C,D) (Mariani, 1984; Kouyama and Marshak, 1992; Haverkamp et al., 2005; Breuninger et al., 2011). We found 48 contacts of CBC9s and cones, involving 43 cones (Figure 1—figure supplement 1A). We visually assessed all contacts and found that 29 of these were in the periphery of the cone pedicle, where no synapses are expected (Figure 1—figure supplement 1B) (Dowling and Boycott, 1966; Chun et al., 1996). This left 14 potential S-cones with invaginating contacts from at least one CBC9. It has been shown that S-cones are contacted by the dendrites of all neighboring CBC9s and that these contacts occur mostly at the tip of dendritic branches (Haverkamp et al., 2005). Out of the 14 candidate cones, eight cones had only one CBC9 contact. Some of these cones were contacted by a CBC9 dendritic branch that continued past the contact site. Other cones – although contact by one CBC9 – were not contacted by passing dendrites from other CBC9s. The other six cones had at least two invaginating contacts from CBC9s. These originated from two different CBC9s or – in case they originated only from a single CBC9 – at least one of them was formed by a dendritic branch ending at the cone (Figure 1E). We labeled the eight cones that featured only a single CBC9 contact as M-cones (Figure 1D and Figure 1—figure supplement 1C), and defined the remaining six candidate cones as S-cones (Figure 1D and Figure 1—figure supplement 1C and D, see Materials and methods). This corresponds to a fraction of 4.8% S-cones (6/124 cones within the dendritic field of at least one CBC9), matching the 3–5% reported in previous studies (Röhlich et al., 1994; Haverkamp et al., 2005).

An alternative scheme for identifying S-cones would have been to classify all cones with at least one invaginating contact from CBC9 as S-cones. This would have resulted in a total of 14 S-cones out of 124 cones (Figure 3—figure supplement 2A) or a fraction of 11.3%. Because this S-cone percentage is much larger than the 3–5% reported earlier (Haverkamp et al., 2005), we consider this scenario as very unlikely ($p=0.0037$, binomial test, null hypothesis: 5% S-cones, $n = 124$).

Classification of photoreceptor-BC contacts

We next developed an automatic method to distinguish contacts likely corresponding to synaptic connections from false contacts. As the tissue in the dataset was stained to enhance cell-surface contrast to enable automatic reconstruction, it is not possible to distinguish between synaptic contacts based on explicit ultrastructural synaptic markers, such as vesicles, synaptic ribbons or postsynaptic densities (see also discussion in Helmstaedter et al., 2013). In contrast to the synaptic contacts in the inner plexiform layer studied by Helmstaedter et al. (Helmstaedter et al., 2013), the highly stereotypical morphology of synapses at photoreceptor axon terminals allowed us to classify the contacts (Haverkamp et al., 2000): The ribbon synapses of the cones are placed exclusively in the presynaptic area at the bottom of the cone pedicles. Here, ON-cone

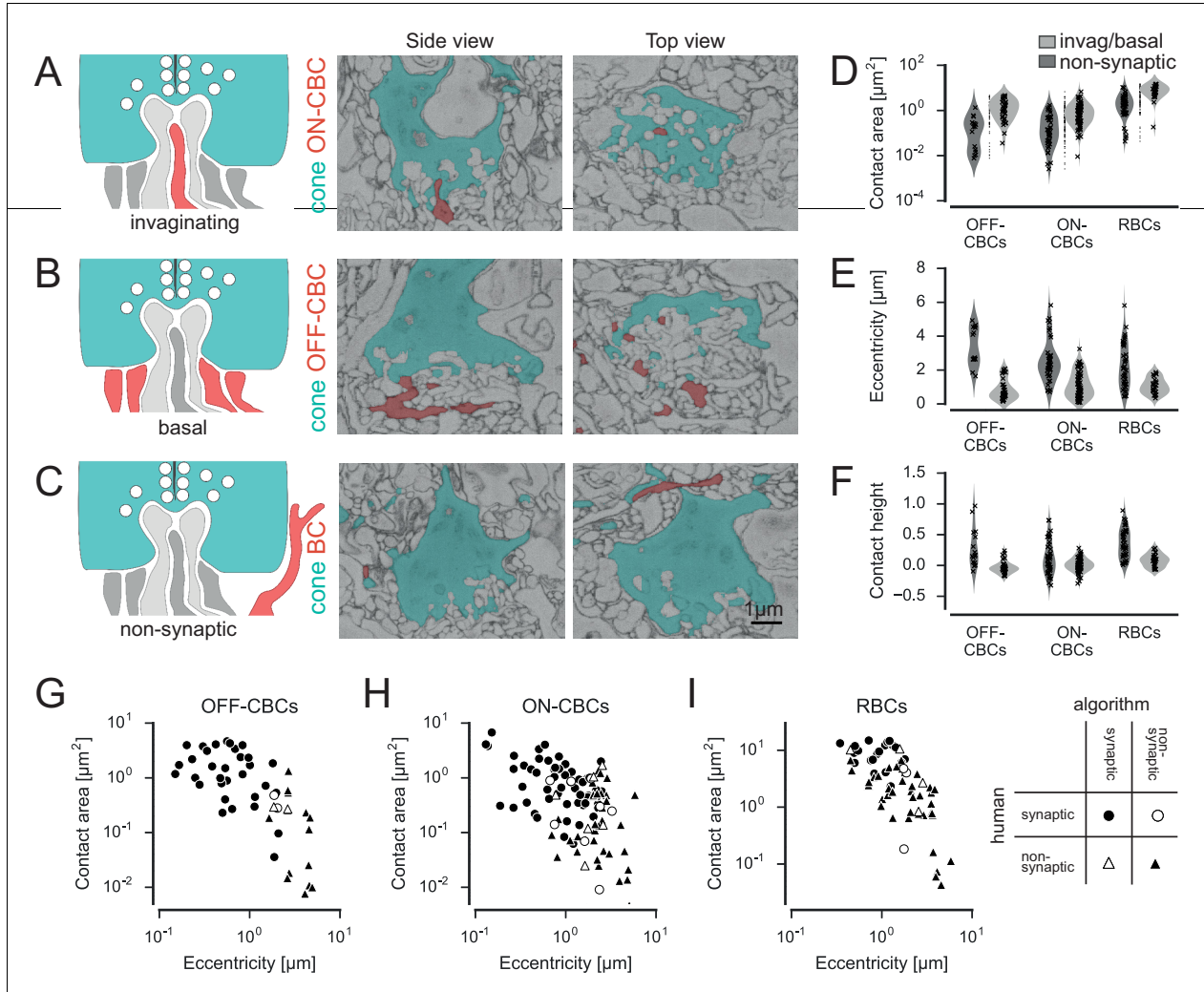


Figure 2. Classification of cone contacts. (A) Invaginating ON-CBC contact. Schematic drawing (left), EM side view (center) and top view (right). Red and dark grey, BC dendrites; light grey, horizontal cell dendrites; cyan, cone pedicles. (B) Basal/flat OFF-CBC contact as in A. (C) Peripheral (non-synaptic) BC contact as in A. (D–F) Contact area (D) eccentricity (E) contact height (F) of invaginating/basal and non-synaptic contacts for OFF-/ON-CBCs and rod bipolar cells (RBCs). (G–I) Contact area versus eccentricity for OFF-CBC (G), ON-CBC (H) and RBC (I) contacts indicating correctly and incorrectly classified contacts.

DOI: [10.7554/eLife.20041.004](https://doi.org/10.7554/eLife.20041.004)

The following figure supplements are available for figure 2:

Figure supplement 1. Illustration of parameters used for classifying contacts.

DOI: [10.7554/eLife.20041.005](https://doi.org/10.7554/eLife.20041.005)

Figure supplement 2. Examples for disagreements between human and algorithmic classification.

DOI: [10.7554/eLife.20041.006](https://doi.org/10.7554/eLife.20041.006)

bipolar cells (ON-CBCs) make invaginating contacts, where the dendritic tips reach a few hundred nanometers into the presynaptic area of cone pedicles (Dowling and Boycott, 1966). In contrast, OFF-cone BCs (OFF-CBCs) make basal contacts in the same area (Figure 2B). These ‘true’ contacts have to be distinguished from contacts in the periphery or at the (out)sides

of the cone pedicle as well as contacts between dendrites and cone telodendria, which can happen, for instance as dendrites pass by (**Figure 2C**).

In total, we found $n = 20,944$ contacts in $n = 2620$ pairs of cones and BCs. We trained a support vector machine (SVM) classifier to distinguish whether or not an individual BC obtains input from a cone (as opposed to classifying each individual contact site, see Materials and methods). To this end, we defined a set of seven features, including contact area, eccentricity and contact height, which allowed distinguishing between potential synaptic contacts and 'false' contacts (**Figure 2D–F**, **Figure 2—figure supplement 1**). For training of the classifier, we manually labeled a randomly selected set of contacts ($n = 50$ for OFF-CBCs, $n = 108$ for ON-CBCs and $n = 67$ for RBCs). Given the highly stereotypical anatomy of the photoreceptor-BC synapse, labeling performed by an experienced human observer is expected to be very accurate – we here consider therefore the human labels as 'ground-truth'. We trained separate classifiers for ON-CBCs, OFF-CBCs and RBCs and found that they could reliably distinguish between true and false contacts, with a success rate of ~90% (leave-one-out cross-validation accuracy, **Figure 2G–I**). Deviations between the labels of the automatic classifier and the human labels did not vary systematically with BC type (see Materials and methods). Such deviations typically occurred when human labels were assigned based on more global structural features of a contact; such more contextual features were not included in the features used for automatic classification (examples of misclassified contacts are shown in **Figure 2—figure supplement 2** and **Videos 1–3**).

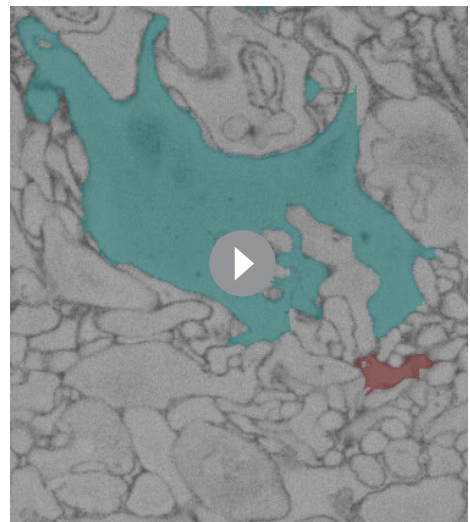
Contacts between cones and CBCs

We analyzed contacts between CBCs and S- and M-cones in the center of the EM stack where cones were covered by a complete set of all BC types. There was no difference in the number of CBCs contacted by S- and M-cones with 12.2 ± 1.5 CBCs ($n = 5$ cones, mean \pm SEM) for S-cones and 12.2 ± 0.4 CBCs ($n = 71$ cones) for M-cones, respectively. Similarly, the total number of contact points per cone was almost identical for S- and M-cones with an average of 108 ± 24 per S- and 105 ± 5 per M-cone.

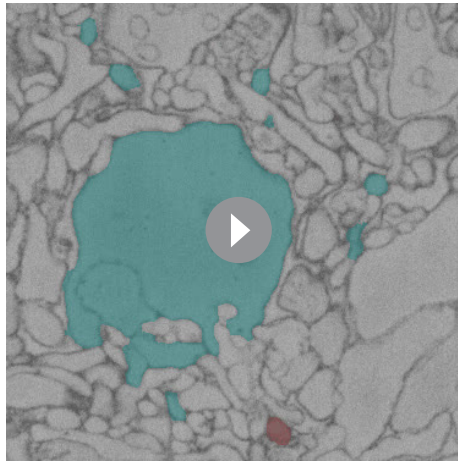
We first studied the convergent connectivity onto the different CBC types and studied how many cones provide input to a single BC of each type (**Figure 3A and B**). To this end, we classified type 5 CBCs, which had not been further subdivided by Helmstaedter et al. (**Helmstaedter et al., 2013**), into three types (**Figure 3—figure supplement 1**, see Materials and methods) in agreement with recent reports (**Greene et al., 2016**).

Most CBC types were contacted predominantly by M-cones, with an average of 2–6 cones contacting individual CBCs. One exception was the CBC9 that – by our definition of S-cones – received considerable S-cone input. We also detected a few contacts between CBC9s and M-cones; these are a consequence of our restrictive definition of S-cone and originate from those cones for which we found only single CBC9 contacts, such that they were classified as M-cone (see above, **Figure 1**; see also **Figure 3—figure supplement 2**).

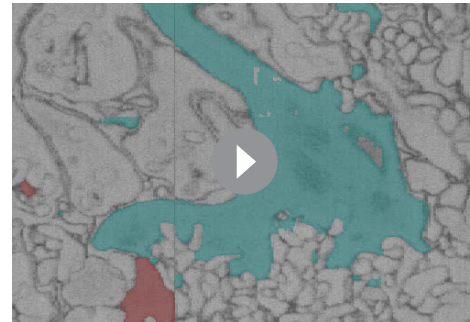
We next evaluated the divergent connectivity from S- and M-cones to CBCs and studied how many individual BCs of each type were contacted by a single cone (**Figure 3C**). We found that each M-cone contacted on average a little less than one CBC1, while S-cones contacted almost no CBC1, consistent with previous reports (**Breuninger et al., 2011**). Conversely, we found that M-cones almost never contacted CBC9s (see above), but S-cones contacted on average two. Both cone types contacted all other CBC types (**Figure 3D**), with each cone making contact with



Video 1. Animated 3D stack of an ON contact (human: contact, algorithm: no contact).
DOI: 10.7554/eLife.20041.007



Video 2. Animated 3D stack of an ON contact (human: no contact, algorithm: contact).
DOI: [10.7554/eLife.20041.008](https://doi.org/10.7554/eLife.20041.008)



Video 3. Animated 3D stack of a RBC contact (human: no contact, algorithm: contact).
DOI: [10.7554/eLife.20041.009](https://doi.org/10.7554/eLife.20041.009)

at least one CBC2, 3B, 4, 5I, 6 and 7. In contrast, some cones did not contact ON-CBC types 5T, 5O, X and 8, such that they were contacted by considerably less than one cone on average. In addition, we tested the hypothesis that CBCs other than type 1 and 9 unselectively contact all cones within their dendritic field (Wässle et al., 2009). To this end, we compared the number of contacted cones and the number of cones that are in reach of the BC dendrites (Figure 3E–G). OFF-CBCs (types 1–4) contacted on average 65–75% of the cones in their dendritic field, with very similar numbers across types (Figure 3G). In contrast, ON-CBCs showed greater diversity: The connectivity pattern of types 5I, 6 and 7 was similar to that observed in the OFF types (Figure 3G); these cells sampled from the majority of cones within their dendritic field (60–80%). CBC5T, 5O, X and 8, however, contacted less than half of the cones within their dendritic field (Figure 3G), with the lowest fraction contacted by CBCX (~20%). This result is not due to a systematic error in our contact classification: We manually checked volume-reconstructed dendritic trees of the respective types for completeness and frequently found dendrites passing underneath a cone with a distance of 1–3 μm without contacting it (Figure 3—figure supplement 3).

Finally, we studied the contact density along CBC dendrites (Figure 3H and I). To check for systematic variation independent of the absolute size of the CBC dendritic tree, we normalized the cone contact density for the dendritic field size of each CBC type (Figure 3I). Almost all CBC types received input at a very similar location relative to their soma, except for CBCX, which received the majority of inputs closer to the soma than all other types relative to its dendritic field size.

As a control, we also ran the connectivity analysis with the set of S-cones from our alternative, more liberal classification (Figure 3—figure supplement 2B,C). In this analysis, CBC9 was the only color specific BC type whereas all other BC types, including CBC1, contacted both S- and M-cones without preferences (Figure 3—figure supplement 2C). This contradicts the result of a previous analysis based on physiology, which implies that CBC1 does not receive S-cone input (Breuninger et al., 2011).

The CBCX has few and atypical cone contacts

CBCX had an atypical connectivity pattern compared to other CBC types, so we decided to study its connections in more detail. This BC type has only recently been identified by (Helmstaedter et al., 2013; Shekhar et al., 2016). It has a compact dendritic tree but a relatively wide axonal terminal system that stratifies narrowly at approximately the same depth as CBC5O and 5I do. Interestingly, CBCX seems to sample the cone input very sparsely, with input from only two cones on average, and contacting only about 20% of the cones available in its dendritic field (Figure 3C,D and G). In fact, dendrites of CBCX oftentimes passed underneath cones or even stopped shortly before cone pedicles without making contacts at all (Figure 4A and B). It is unlikely that this resulted from

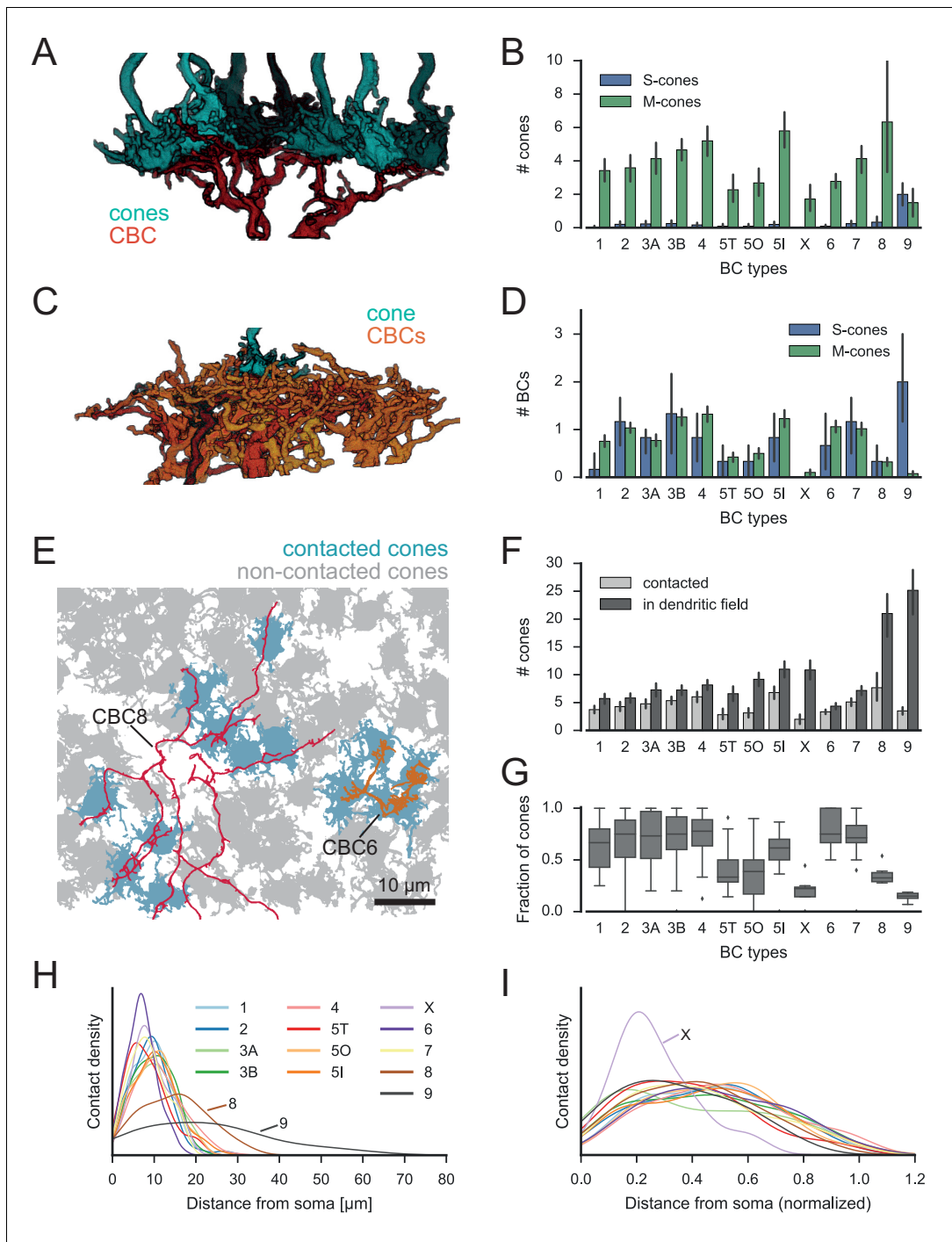


Figure 3. Quantification of cone-to-CBC contacts. (A) Volume-reconstructed single BC dendrite (red) contacting numerous cone pedicles (cyan). (B) Number of S- and M-cones contacted by different CBC types. (C) Volume-reconstructed single cone (cyan) contacted by multiple BCs (orange/red). (D) Number of CBCs per type contacted by individual S- and M-cones. (E) Example cone array with CBC6 and CBC8 contacting cones. Grey, non-contacted cones; blue, contacted cones. (F) Number of contacted cones and cones within dendritic field for different CBC types. (G) Fraction of
Figure 3 continued on next page

Figure 3 continued

contacted cones/cones within the dendritic field. (H) Kernel density estimate of the distribution of contacted cones as function of distance from BC somata. (I) Same as H. but distance normalized by dendritic field size. Bars in B,D,F indicate 95% CI.

DOI: [10.7554/eLife.20041.010](https://doi.org/10.7554/eLife.20041.010)

The following figure supplements are available for figure 3:

Figure supplement 1. Classification of type 5 BCs.

DOI: [10.7554/eLife.20041.011](https://doi.org/10.7554/eLife.20041.011)

Figure supplement 2. Connectivity analysis for alternative s-cone classification.

DOI: [10.7554/eLife.20041.012](https://doi.org/10.7554/eLife.20041.012)

Figure supplement 3. Example of a passing dendrite without contacts.

DOI: [10.7554/eLife.20041.013](https://doi.org/10.7554/eLife.20041.013)

incomplete skeletons for these BCs, as all skeletons were independently verified for this study and corrected where necessary (see Materials and methods).

We re-examined all detected contacts between CBCXs and cones and found that very few of those were ‘classical’ invaginating ON-CBC contacts (3 out of 19 contacts, $n = 7$ cells, **Figure 4B–D**). The vast majority were ‘tip’ contacts (16 out of 19 contacts, $n = 7$ cells), which were similar to basal contacts made by OFF-CBC dendrites (**Figure 4B–D**). The available data was not conclusive with regards to the question whether these tip contacts of CBCX are smaller than those of OFF-CBCs (median area: $0.05 \mu\text{m}^2$ for $n = 22$ CBCX contacts; $0.10 \mu\text{m}^2$ for $n = 23$ OFF-CBC contacts, but $p=0.17$, Wilcoxon ranksum test).

In contrast to the CBCX, the other ON-CBC types made mostly invaginating contacts (71 out of 81 contacts, $n = 12$ cells, two cells per BC type, **Figure 4D**), indicating a significant effect of cell type on contact type (GLM with Poisson output distribution, $n = 38$, interaction: $p=3.6 \times 10^{-7}$, see Materials and methods). We checked if CBCX receive rod input instead but did not observe any rod contacts (see below). Thus, the CBCX appears to be an ON-CBC with both very sparse and atypical cone contacts similar to those made by OFF-CBCs. Still, based on the axonal stratification depth (**Helmstaedter et al., 2013**) and recent electrophysiological and functional recordings (**Ichinose et al., 2014; Franke et al., 2016**) this BC type is most likely an ON-CBC, supported by its mGluR6 expression (**Shekhar et al., 2016**).

RBCs make contacts with cones

We next analyzed the connectivity between photoreceptors and rod bipolar cells (RBCs) to test the hypothesis that RBCs may contact cones directly (**Pang et al., 2010**). Three cells labeled as RBC in Helmstaedter et al. (**Helmstaedter et al., 2013**) were excluded from this analysis, as they did not contact any rods (**Figure 5—figure supplement 1**). We also found some rods not contacted by any RBC, which is likely due to incomplete tracing of the fine dendritic tips of some RBCs.

In fact, RBCs did not only contact rod spherules but also cone pedicles (**Figure 5A,B**). These contacts were typical ON-CBC contacts with invaginating dendritic tips into the cone pedicles (**Figure 5B**). To quantify the cone-to-RBC connectivity in more detail, we counted the number of cones contacted by an individual RBC. While the vast majority (75%) contacted at least one cone, only 25% of all RBCs ($n = 141$) did not contact any (**Figure 5C**). However, we did not find a preference of RBCs to connect S- or M-cones (**Figure 5D**). Conversely, 45% of cones contacted a single RBC, ~35% spread their signal to two to four RBCs, and only 20% of the cones did not make any contact with an RBC (**Figure 5E**). Our finding provides an anatomical basis to the physiologically postulated direct cone input into a subset of RBCs (**Pang et al., 2010**). Next, we evaluated whether RBCs contacting only rods or both cone(s) and rods represent two types of RBC, as hypothesized by **Pang et al. (2010)**. However, the two groups of RBCs did not differ regarding the stratification depth of their axonal arbor (**Figure 5—figure supplement 2A**), number of rod contacts (**Figure 5—figure supplement 2B**) or potential connectivity to All amacrine cells (**Figure 5—figure supplement 2C**), and did not form independent mosaics (**Figure 5—figure supplement 2D**). In addition, the dendritic field size (116 vs $131 \mu\text{m}^2$, $p=0.1$, $n = 139$ RBCs) and the number of dendritic tips (46 vs. 45.5 , $p=0.8$, $n = 12$ manually counted RBCs) did not differ significantly between the two groups. Therefore, the available anatomical data argue against two types of RBC.

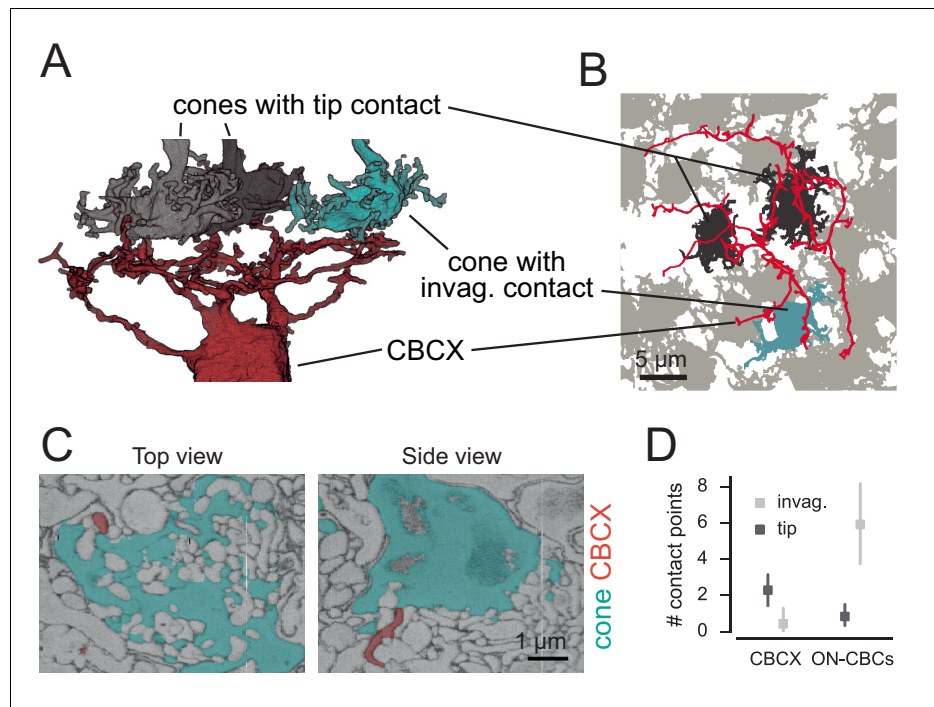


Figure 4. CBCX makes few and atypical cone contacts. (A) Volume-reconstructed CBCX dendritic arbor (red) contacting few cone pedicles (cyan, invaginating contact; grey, tip contact). (B) Same exemplary cone array as in A with CBCX dendritic arbor contacting cones. Light grey, non-contacted cones; cyan, invaginating contacts; dark grey, tip contacts. (C) EM image showing tip contact between CBCX (red) and cone pedicles (cyan), top view (left) and side view (right). (D) Invaginating and tip contacts in CBCXs and other ON-CBCs. Bars in D indicate 95% CI. DOI: [10.7554/eLife.20041.014](https://doi.org/10.7554/eLife.20041.014)

Quantification of rod to OFF-CBC contacts

Analogous to the analysis above, we skeletonized and volume rendered a complete set of over 2000 neighboring rod spherules (about 50% of the EM field, *Figure 6A*, *Figure 6—figure supplement 1*) and identified rod-to-bipolar cell connections. In addition to the well-described invaginating rod-to-RBC connections (*Figure 6B*), we also found basal contacts between OFF-CBCs and rods close to the invaginating RBC dendrites (*Figure 6C*), as described earlier (*Hack et al., 1999; Mataruga et al., 2007; Haverkamp et al., 2008; Tsukamoto and Omi, 2014*). We did not find any contacts between ON-CBCs and rods (in agreement with *Tsukamoto and Omi, 2014*; but see *Tsukamoto et al., 2007*).

A single RBC contacted about 35 rods (*Figure 6D*), which is slightly more than what was recently reported (~25 rods, *Tsukamoto and Omi, 2013*). A single rod contacted one or two RBCs, but very rarely no RBC or more than two (*Figure 6E*). In all cases with two invaginating dendrites, the dendrites belonged to two different RBCs ($n = 30$ rods). The rods without RBC contacts were mainly located at the border of the reconstructed volume, where we could not recover all RBCs. The number of rods contacting OFF-CBCs was much lower: Whereas CBC1 and CBC2 did not receive considerable rod input, CBC3A, CBC3B and CBC4 were contacted by 5–10 rods, with CBC3B receiving the strongest rod input (*Figure 6D*).

Discussion

We analyzed an existing electron microscopy dataset (*Helmstaedter et al., 2013*) to quantify the connectivity between photoreceptors and bipolar cells. We found interesting violations of

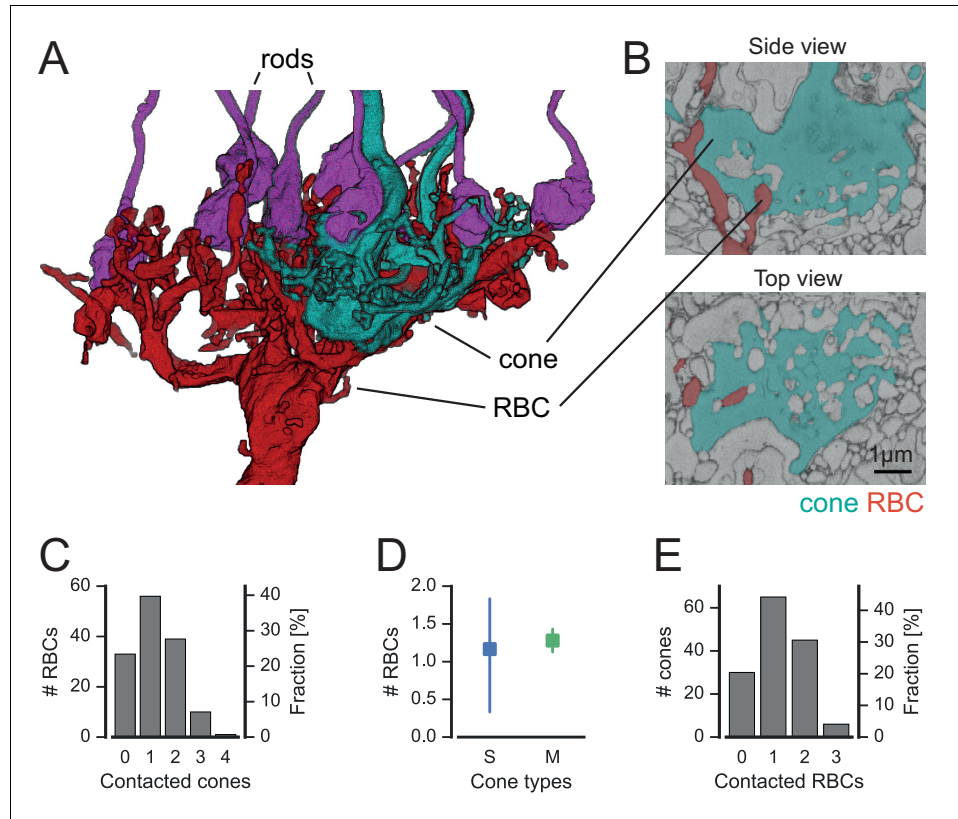


Figure 5. Cones contact rod bipolar cells. (A) Volume-reconstructed RBC (red) contacting both rods (magenta) and cone pedicles (cyan). (B) EM images showing invaginating contact between cone (cyan) and RBC (red), side view (top) and top view (bottom). (C) Number of RBCs contacted by cones. (D). Number of RBCs contacted by S- and M cones. (E) Number of cones contacted by RBCs. Bars in D. indicate 95% CI.
DOI: [10.7554/eLife.20041.015](https://doi.org/10.7554/eLife.20041.015)

The following figure supplements are available for figure 5:

Figure supplement 1. Excluded RBCs.

DOI: [10.7554/eLife.20041.016](https://doi.org/10.7554/eLife.20041.016)

Figure supplement 2. No evidence for two RBC subtypes.

DOI: [10.7554/eLife.20041.017](https://doi.org/10.7554/eLife.20041.017)

established principles of outer retinal connectivity: The newly discovered CBCX (*Helmstaedter et al., 2013*), likely an ON-CBC (*Ichinose et al., 2014; Franke et al., 2016*), had unexpectedly few and mostly atypical basal contacts to cones. While CBC types 5T, 5O and 8 also contacted fewer cones than expected from their dendritic field, they exhibited ‘standard’ invaginating synapses. In addition, we provide anatomical evidence that rod and cone pathways are interconnected, showing frequent cone-RBC contacts. The emerging picture of BC types with their input profiles are summarized in *Figure 7*.

Does a ‘contact’ represent a synaptic connection?

Since the dataset we used was not labeled for synaptic structures, we used automatic classifiers based on structural criteria to identify putative synaptic contacts between BCs and photoreceptors. Due to the highly stereotypical anatomy of the photoreceptor-BC synapse, these criteria allow unambiguous identification of synaptic sites for trained humans (see also *Results*). For example, we used the proximity of the closest contact to the center of the cone pedicle region as a feature, where

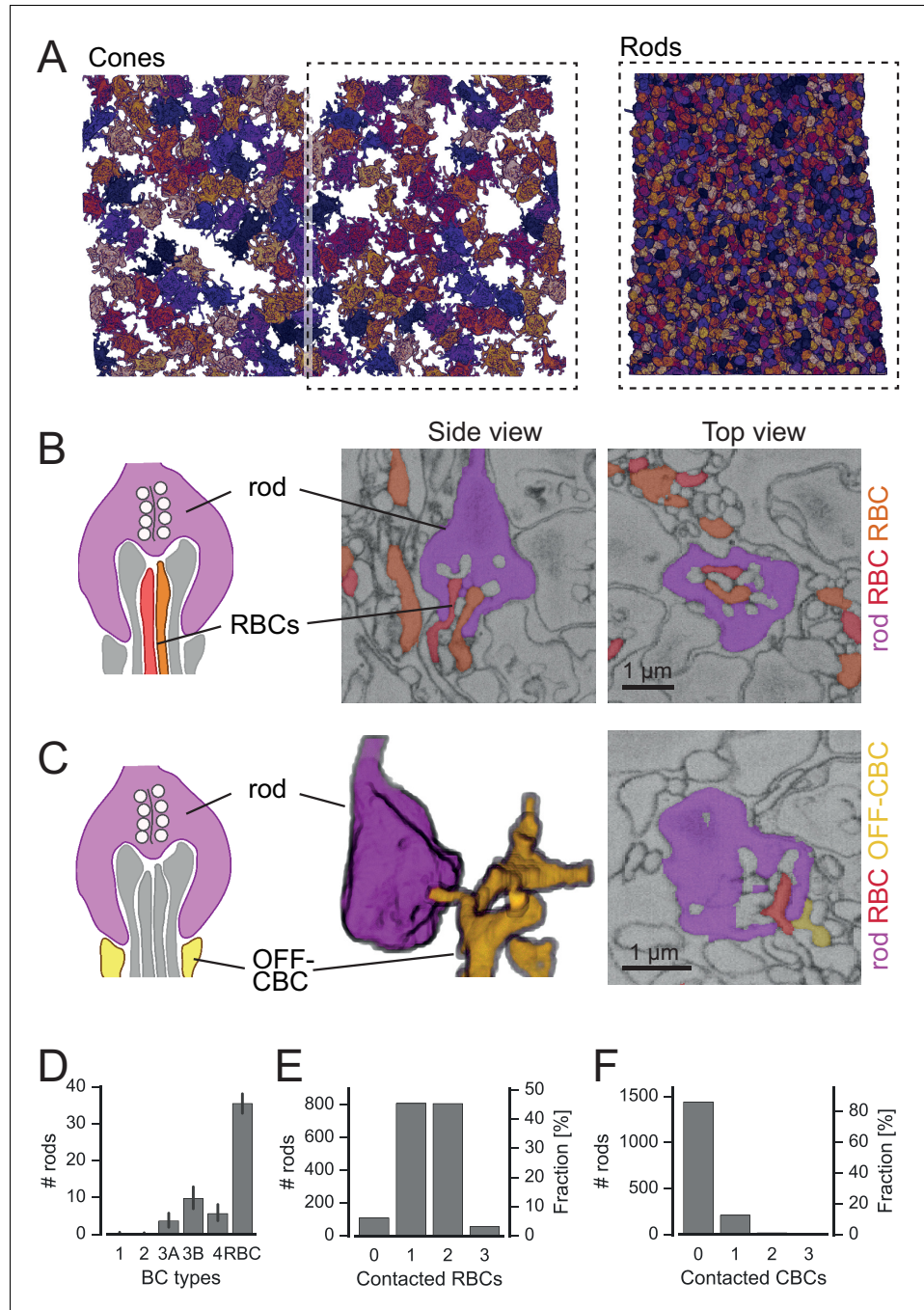


Figure 6. Rods contact RBCs and OFF-CBCs. (A) Volume-reconstructed, neighboring rod spherules (right) in one half of the field of the reconstructed cone pedicles (left). (B) Rod spherule (magenta) with invaginating dendrites of two RBCs (orange, red). Schematic drawing (left), EM images side view (middle) and top view (right). (C) Rod spherule (magenta) with basal contacts by OFF-CBCs (yellow). Schematic (left), volume-reconstructed vertical view (middle), EM image with top view (right). The latter also shows an invaginating RBC dendrite (red). (D–F). Number of rods (and fraction) contacted by RBCs (D,E), and OFF-CBC types (D, F). Bars in D. indicate 95% CI.

Figure 6 continued on next page

Figure 6 continued

DOI: [10.7554/eLife.20041.018](https://doi.org/10.7554/eLife.20041.018)

The following figure supplement is available for figure 6:

Figure supplement 1. Classification of rod contact classification.

DOI: [10.7554/eLife.20041.019](https://doi.org/10.7554/eLife.20041.019)

presynaptic ribbons have been reported at the ultrastructural level (Dowling and Boycott, 1966; Chun et al., 1996).

The overall accuracy of the classifiers evaluated with human annotated labels was high (~90%). Nevertheless, it is possible that a few contacts were misclassified. Manual quality control, however, revealed no systematic errors. Therefore it is unlikely that classification errors affected our main conclusions. Mismatches between human and classifier labels usually occurred when the human used the global context for the assessment of a contact, knowledge that is not easily transferred into an algorithm (Figure 2—figure supplement 2). Still, human error cannot be ruled out: For instance, contact points labeled by humans as non-synaptic may feature a gap junction and are therefore functional rather than random. For reference, all data including software for classifying and examining BC-cone contacts is available online.

Is there an effect of retinal location?

Unfortunately, the retinal location of the EM stack used here is unknown (Helmstaedter et al., 2013); it may originate from the ventral retina, where M-cones co-express S-opsin (Röhlich et al., 1994; Baden et al., 2013). However, as ‘true’ S-cones were shown to be evenly distributed across the retina (Haverkamp et al., 2005), CBC9 connectivity can be used for identification of S-cones independent of location. Nevertheless, it cannot be excluded that opsin co-expression in M-cones in the ventral retina may influence the connectivity patterns between the M-cones and the remaining bipolar cell types.

Sparse contacts between some ON CBC types and cones

We found that ON-CBCs 5T, 5O, X and 8 contact fewer cones than expected from the size of their dendritic field. We observed that many of their dendrites passed by the cone pedicles with a distance of 1–3 μm or even ended under a cone pedicle without contacting it (Figure 3—figure

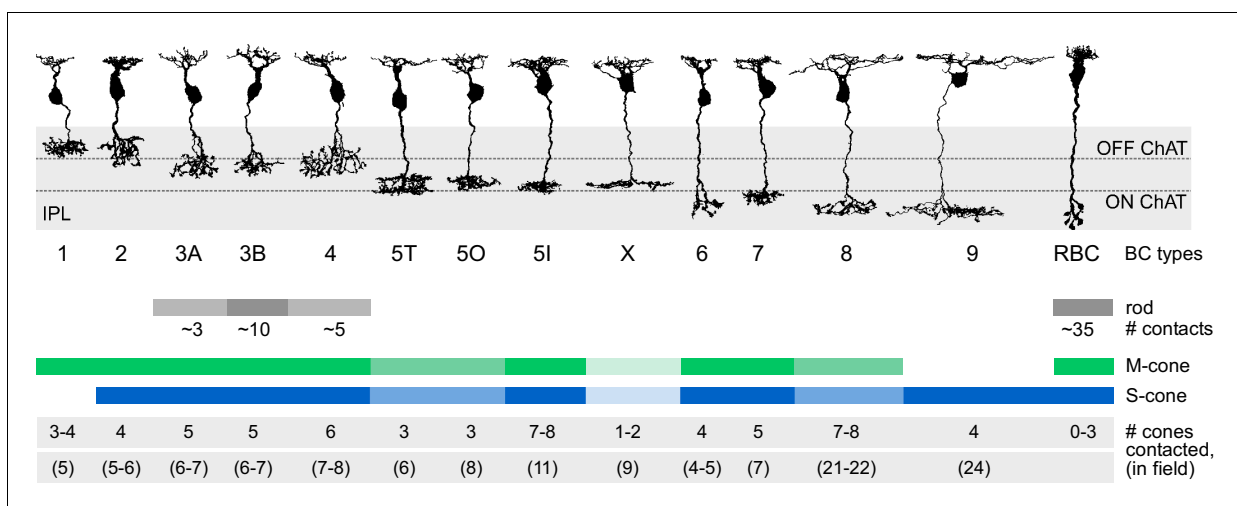


Figure 7. Connectivity between cone and rod photoreceptors and bipolar cells in the mouse retina. Representative examples of bipolar cell types in the mouse retina are shown. The number of cones in the dendritic field number and contacted photoreceptors are given for each type.

DOI: [10.7554/eLife.20041.020](https://doi.org/10.7554/eLife.20041.020)

supplement 1). This is in agreement with a recent study reporting that CBC8 does not contact all cones within its dendritic field (Dunn and Wong, 2012), but in contrast to earlier studies that concluded that different diffuse BC types receive input from all cones within their dendritic field (Boycott and Wässle, 1991; Wässle et al., 2009). However, a crucial difference with the earlier studies and our study is spatial resolution: Conventional light microscopy can resolve depth with a resolution of several hundreds of nanometers, whereas the EM dataset we used has a resolution of 25 nm, allowing us to more accurately assess whether pre- and postsynaptic structures are in contact with each other.

Could diffusion-based synaptic signaling play a role in ON-CBCs with sparse contacts? 'Diffusion-based' synaptic contacts have been proposed for OFF-CBCs (DeVries et al., 2006) and between cones (Szmajda and DeVries, 2011). However, although diffusion-based transmission may be present in the outer retina, there is no evidence so far that cone signals reach bipolar cells that neither make invaginating or basal contacts (i.e. with dendrites just passing by a cone pedicle).

CBCX makes atypical contacts with cones

As shown above, the CBCX makes the fewest contacts with cones of all ON CBCs. On average, they contacted only about two cones, representing only 20% of the cones within the area of their dendrites. This finding is in agreement with a recent single-cell RNA-seq study, which found that CBCXs feature lower expression levels for metabotropic glutamate receptor mGluR6 (*grm6*) – the hallmark of ON-BCs – compared to other ON-CBC types (Shekhar et al., 2016). The mouse CBCX is reminiscent of the giant CBC in macaque retina (Joo et al., 2011, Tsukamoto and Omi, 2016) with respect to several features: Also the latter has a very large and sparsely branched dendritic tree and a relatively large axonal arbor that stratifies in the middle of the IPL and contacts only about 50% of the cones in its dendritic field.

In contrast to all other ON-CBCs, we found that the vast majority of CBCX contacts were not invaginating but rather resembled basal OFF-CBC contacts. It is unclear if these tip contacts are indeed functional synaptic sites. This is not the first finding to challenge the traditional view that ON-CBCs form only invaginating and OFF-CBCs only basal synaptic contacts. In the primate fovea, diffuse ON-CBCs (DBs) form basal contacts with foveal cones since almost all invaginating sites are taken by midget bipolar cell dendrites (Calkins et al., 1996). This spatial limitation is less evident in mid-peripheral primate retina. At 3–4 mm eccentricity, diffuse ON-CBCs receive 10% (DB5) to 40% (DB4 and DB6) of their cone input through basal synapses (Hopkins and Boycott, 1996).

Interestingly, CBCX contacts in the IPL also appear to be distinct from those of other BC types: First, the majority of cells contacted by CBCX in the IPL are amacrine cells rather than ganglion cells (Helmstaedter et al., 2013). Second, they form sparse contacts relative to their axon terminal size with comparatively few cells. Thus, the CBCX seems to be an exception, an unusual BC type in many respects in addition to its sparse and atypical connectivity properties in the OPL, reminiscent of a recently described dendrite-less interneuron type that expresses BC-specific genes (Shekhar et al., 2016) and was named GluM1 (glutamatergic monopolar interneuron) (Della Santina et al., 2016). It is conceivable that – similar to the GluM1 – the CBCX is evolutionary on its way to retracting its dendrites. Alternatively, CBCX develops a tad later than other CBC types and most potential synaptic sites at cone ribbons are already occupied, such that the CBCX can only form few connections – reminiscent of the situation in primate (see above).

May RBCs form an additional photopic ON channel?

We found that cones connect to 75% of RBCs; in many cases, one cone contacted multiple RBCs. In turn, 35% of RBCs received converging input from several cones. This massive cone input via invaginating synapses to RBCs suggests a prominent use of the primary rod pathway (Bloomfield and Dacheux, 2001) during photopic conditions. Consistent with our findings, RBCs can be activated under photopic light conditions (Franke et al., 2016). However, since rods recover at high light levels (Blakemore and Rushton, 1965), the functional significance of cone input to RBC remains unclear. In principle, it is possible that the observed cone-RBC synapses are developmental 'left-overs' without physiological relevance, but as the cone-RBC contacts look like standard cone-CBC invaginating synapses, we think that it is more likely that they contribute to RBC activation under

photopic conditions, especially in mid-range light intensities where cones are active but rods not yet recovering (Tikidji-Hamburyan *et al.*, 2015).

If this was the case, cone activation of RBCs could indirectly inhibit OFF-CBCs via All amacrine cells. This suggests that RBCs may contribute to crossover inhibition (Molnar and Werblin, 2007). On the other hand, it is unclear whether gap junctions between Alls and ON-CBCs are in an open or closed state under light-adapted conditions (Bloomfield *et al.*, 1997; Kuo *et al.*, 2016). With open gap junctions, activating RBCs may boost the signal in ON-CBC axon terminals and therefore enhance contrast (in complement with the OFF-CBC inhibition).

Based on the physiological finding that only a subset of RBCs receive input from cones, Pang *et al.* (2010) suggested that there may be two distinct RBC types, with the rod-only one having axon terminals ending closer to the ganglion cell layer. Our data do not provide evidence for two RBC types based on the connectivity in the outer retina. This agrees well with recent findings from single-cell RNA-seq experiments, where all RBCs fell into a single genetic cluster with little heterogeneity (Shekhar *et al.*, 2016).

OFF CBC types contact different numbers of rods

We quantified the number of rods contacting the five OFF-CBC types. Whereas CBC1 and 2 received almost no rod input, we observed flat/basal contacts between rods and types CBC3A, 3B and 4, providing a quantitative confirmation of this finding (Mataruga *et al.*, 2007; Haverkamp *et al.*, 2008; Tsukamoto and Omi, 2014). CBC3A and 4 received input from ~5 rods in addition to the ~5 cones contacted by them. CBC3B sampled from the same number of cones but was contacted by about twice as many rods. Since these basal contacts between rods and OFF CBCs have been shown to express AMPA receptors (Hack *et al.*, 1999), rods likely provide considerable input to OFF-CBCs, possibly representing a distinct scotopic OFF channel complementing the scotopic ON channel via RBCs. Interestingly, the morphologically similar CBC3A and 3B may obtain their (functional) differences not only from the expression of different ionotropic glutamate receptors (Puller *et al.*, 2013) but also from their connectivity with rods.

Conclusion

Here, we performed a systematic quantitative analysis of the photoreceptor-to-bipolar cell synapse. We showed that there are exceptions to several established principles of outer retinal connectivity. In particular, we found several ON-BC types that contacted only a relatively small fraction of the cones in their dendritic field. We also find that rod and cone pathways already interact strongly in the outer plexiform layer. Whether these are general features of mammalian retinas or evolutionary specializations unique to the mouse remains to be seen.

Materials and methods

Dataset and preprocessing

We used the SBEM dataset e2006 published by (Helmstaedter *et al.*, 2013) for our analysis (<http://www.neuro.mpg.de/connectomics>). The dataset has a voxel resolution of $16.5 \times 16.5 \times 25$ nm with dimensions $114 \mu\text{m} \times 80 \mu\text{m} \times 132 \mu\text{m}$. We performed volume segmentation of the outer plexiform layer (OPL) using the algorithms of (Helmstaedter *et al.*, 2013). The preprocessing of the data consisted of three steps: (i) Segmentation of the image stack, (ii) merging of the segmented regions and (iii) collection of regions into cell volumes based on traced skeletons.

We modified the segmentation algorithm to prevent merging of two segments if the total volume was above a threshold ($>50,000$ voxels), as sometimes the volumes of two cone pedicles could not be separated with the original algorithm. Although this modification resulted in overall smaller segments, these were collected and correctly assigned to cells based on the skeletons in the last step of the preprocessing.

We identified 163 cone pedicles and created skeletons spanning their volume using the software KNOSSOS ((Helmstaedter *et al.*, 2012), www.knossostool.org). We typically traced the center of the cone pedicle coarsely and added the individual telodendria for detailed reconstruction. In addition, we traced 2177 rod spherules covering half of the dataset (Figure 6). For our analysis, we used all photoreceptors for which at least 50% of the volume had been reconstructed (resulting in 147

cones and 1799 rods). We used the BC skeletons published by *Helmstaedter et al. (2013)*, with the following exceptions: We completed the dendritic trees of three XBCs (CBCXs), which were incompletely traced in the original dataset. In addition, we discarded three BCs originally classified as RBCs because they were lacking rod contacts as well as the large axonal boutons typical for RBCs (Supp. **Figure 6A–C**), and one BC classified as a CBC9 because its dendritic field was mostly outside of the data stack (Supp. **Figure 6D**).

Next, we used the algorithm by (*Helmstaedter et al., 2013*) to detect and calculate the position and area of 20,944 contact points between cone pedicles and BC dendrites and 7993 contact points between rod spherules and BC dendrites. To simplify the later visual inspection of contacts, we used the reconstructed cell volumes to generate colored overlays for the raw data to highlight the different cells in KNOSSOS.

Identification of S-cones

We detected 169 contacts in 51 pairs of CBC9s and cones. Upon manual inspection, we found a total of 32 invaginating (potentially synaptic) contacts between 6 CBC9s and 14 cone pedicles.

Based on immunocytochemistry, it has been shown that S-cones are contacted by all CBC9 within reach and that CBC9 contacts to S-cones are mostly at the tips of the dendrites (*Haverkamp et al., 2005*). For all 14 contacted cones, we analyzed the number of invaginating CBC9 contacts, the number of contacting CBC9s, the fraction of CBC9 with dendrites close to the cone that make contact and whether the dendrites end at the cone or continue beyond it (**Figure 1E**). Based on these criteria, we classified 6 out of these 14 cones as S-cones (see also **Figure 1—figure supplement 1**). In addition to our main analysis, we present an alternative analysis that considers the case if all 14 cones were counted as S-cones (**Figure 3—figure supplement 2**).

CBC5 classification

CBC5s were classified initially based on their connectivity to ganglion cells and amacrine cells into types 5A and 5R, where 5R was a group containing multiple types (*Helmstaedter et al., 2013*). In addition, some CBC5s could not be classified due to a lack of axonal overlap with the reconstructed ganglion cells of the types used for classification. Considering the separate coverage factors for dendritic and axonal overlap of all CBC5s together (OPL: 3.14, IPL: 2.89), dividing them into three subtypes is conceivable considering the numbers for other CBC types (**Table 1**). This has already been suggested by (*Greene et al., 2016*), who divide CBC5s into three subtypes based on axonal density profiles (using a different EM dataset that includes only the inner retina).

We followed the classification approach suggested by Greene et al. (*Greene et al., 2016*): First, we calculated the densities of both ON- and OFF-starburst amacrine cells (SACs) dendrites along the optical axis. We fitted the peak of these profiles with a surface using bivariate B-splines of third order. Next, we corrected the density profiles of CBC5 axonal trees by mapping the SAC surfaces to parallel planes. We then applied principal component analysis (**Figure 3—figure supplement 1A**) to obtain a first clustering into three groups by fitting a Gaussian mixture model (GMM) (*Bishop, 2006*) with three components onto the first three principal components of the axon density profiles. The resulting density profiles of the three clusters matches those found by (*Greene et al., 2016*) (**Figure 3—figure supplement 1B**). As we noted a few violations of the postulated tiling of the retina by each type (*Seung and Sümbül, 2014*), we implemented a heuristic to shift cells to a different cluster or swap pairs of cells optimizing a cost function including both overlap in IPL and OPL as well as the GMM clustering (**Figure 3—figure supplement 1**):

$$\mathcal{L} = \lambda_1 \sum_i \sqrt{(x_i - \mu_{c_i})^T \Sigma_{c_i} (x_i - \mu_{c_i})} + \lambda_2 \frac{\sum_{i,j} \delta_{c_i,c_j} O_{ij,OPL}}{\sum_i A_{i,OPL}} + \lambda_2 \frac{\sum_{i,j} \delta_{c_i,c_j} O_{ij,IPL}}{\sum_i A_{i,IPL}}$$

with x_i the parameter vector of cell i , c_i the mixture component cell i is assigned to, μ_c the mean of the mixture component c , Σ_c the covariance matrix of the mixture component c , δ_{ij} the Kronecker delta, $A_{i,OPL/IPL}$ the area of the dendritic field/axonal tree of cell i and $O_{ij,OPL/IPL}$ the overlap of cell i and j in the OPL/IPL. The overlap of two cells is calculated as the intersection of the convex hull of the dendritic fields/axonal trees. Likely, our CBCX corresponds to CBC5D from (*Shekhar et al., 2016*) and CBC5T to CBC5C. Possibly, CBC5I corresponds to CBC5A and CBC5O to CBC5B (see discussion in *Greene et al., 2016*; *Shekhar et al., 2016*).

Table 1. OPL hull area: Average area of convex hull of dendritic field in OPL per cell type [μm^2], mean \pm SEM; OPL cov.: coverage factor derived from convex hulls by computing the sum of convex hull areas divided by area of the union of convex hulls; OPL cov. cones: coverage factor computed from cones by computing the sum of the number of cones in the dendritic field of each cell divided by the number of cones in the joint dendritic field; Wässle: coverage values from [Wässle et al. \(2009\)](#) computed by the same method as OPL cov. cones; IPL hull area: Average area of convex hull of the axonal field in IPL per cell type [μm^2], mean \pm SD; IPL cov.: analogous to OPL cov.

Type	N	OPL hull area [μm^2]	OPL cov.	OPL cov. cones	Wässle	IPL hull area	IPL cov.
CBC1	26	175 \pm 16	1.17	1.48	1.48	376 \pm 16	1.52
CBC2	34	204 \pm 19	1.18	1.55	1.5	353 \pm 23	1.52
CBC3A	22	273 \pm 28	1.17	1.37	1.25	308 \pm 28	1.21
CBC3B	32	292 \pm 19	1.41	1.90	1.55	224 \pm 9	1.24
CBC4	30	302 \pm 20	1.32	1.86	1.6	274 \pm 23	1.33
CBC5T	22	256 \pm 30	1.13	1.30	-	402 \pm 25	1.28
CBC5O	22	380 \pm 41	1.35	1.60	-	359 \pm 23	1.17
CBC5I	25	459 \pm 30	1.55	1.95	-	276 \pm 14	1.22
CBCX	7	433 \pm 34	1.02	1.12	-	899 \pm 126	1.12
CBC6	45	125 \pm 11	1.14	1.58	-	165 \pm 11	1.17
CBC7	29	254 \pm 18	1.22	1.65	1.3	274 \pm 11	1.16
CBC8	6	1249 \pm 144	1.14	1.21	-	699 \pm 55	1.02
CBC9	6	2223 \pm 227	1.84	1.45	-	1605 \pm 335	1.43
RBC	141	128 \pm 3	2.17	4.37	-	65 \pm 3	1.40

DOI: 10.7554/eLife.20041.021

Automatic contact classification

To distinguish potential synaptic contacts between photoreceptors and BCs from accidental contacts, we developed an automatic classification procedure exploiting the stereotypical anatomy of cone-BC synapses (triads, [Dowling and Boycott, 1966](#)). First, we grouped all contacts for a specific cone-BC pair, in the following referred to as a contact-set. We obtained a training data set by randomly selecting 10 contact-sets per CBC type and 50 RBC-cone contact-sets. We excluded CBCX from the training data because of their atypical contacts. To increase classifier performance we added 17 additional RBC-cone contact-sets manually classified as invaginating contacts as well as all 48 CBC9-cone contact-sets classified for the S-cone identification. For those contact-sets, we visually inspected each individual contact point in the raw data combined with volume segmentation overlay using KNOSSOS. Then we classified it either as a central basal contact (potentially synaptic) or peripheral contact (e.g. at the side of a cone or contact with telodendria, likely non-synaptic) for OFF-CBCs or as invaginating contact vs. peripheral contact for ON-CBCs and RBCs. Next, we extracted a set of seven parameters for each contact (see [Figure 2—figure supplement 1](#)):

- **Contact area:** The total contact area aggregated over all contact points between a BC and a cone
- **Eccentricity:** The distance between the cone center and the closest contact point in the plane perpendicular to the optical axis
- **Contact height:** The distance of the contact point with minimal eccentricity from the bottom of the cone pedicle (measured along the optical axis, normalized by the height of the cone pedicle).
- **Distance to branch point:** Minimal distance between a contact point and the closest branch point, measured along the dendrite
- **Distance to tip:** Minimal distance between a contact point and the closest dendritic tip. A large distance occurs for example for a contact between a passing dendrite and a cone.
- **Smallest angle** between the dendrite and the optical axis at a contact point
- **Number of contact points** between cone and BC

Table 2. Cross validation results of BC-to-cone contact classification.

	False positive	False negative	Total score
OFF-CBCs	12.5%	5.9%	0.92
ON-CBCs	14.0%	12.3%	0.87
RBCs	9.3%	12.5%	0.90

DOI: [10.7554/eLife.20041.022](https://doi.org/10.7554/eLife.20041.022)

Based on those parameters we trained a support vector machine classifier with radial basis functions (C-SVM) for each OFF-CBC, ON-CBC and RBC cone contact using the Python package *scikit-learn*. Optimal parameters were determined using leave-one-out cross validation (see **Table 2** for scores and error rates). Typically, 0–2 errors for 10 labeled training samples occurred per BC type (three in one case, CBC3A; 7/48 for CBC9).

Analysis of rod contacts

As the reconstructed rod spherules cover only half of the EM dataset, we restricted the analysis to bipolar cells with their soma position inside this area. To automatically classify the contacts to rods, we followed a similar scheme as for the cones. Again, we grouped the contacts for each pair of BC and rod spherule. As training data, we selected all putative contact sites with CBC1s ($n = 5$) and CBC2s ($n = 32$), 20 random contacts to CBC types 3A, 3B and four as well as 100 random contacts to RBCs. Again, we classified these contacts by visual inspection in KNOSSOS using the raw data with a colored segmentation overlay. In addition, we manually inspected all 132 contact points between rod spherules and ON-CBCs, but could not identify a single potential synaptic contact. We trained SVM classifiers for contacts between rods and RBCs/OFF-CBCs using the same parameters as for the contacts to cones. As synaptic contacts between OFF-CBCs and rod spherules are basal contacts situated close to the invaginating RBC contacts, we added the minimum distance to the next (synaptic) RBC contact as an additional classification parameter for OFF-CBCs. As a consequence, we restricted the analysis of OFF-CBC-to-rod contacts to those rods where RBC contacts could be identified ($n = 1685$). See **Table 3** for scores and error rates from the leave-one-out cross-validation.

Statistics

Error bars in all plots are 95% confidence intervals (CI) calculated as percentiles of the bootstrap distribution obtained via case resampling. In **Figure 4D**, we used a generalized linear mixed model with Poisson output distribution and fixed effects contact type and cell type and random effect cell identity (R package *lme4*). The model yielded a significant intercept ($z = 8.72$, $p < 0.0001$), a significant main effect of cell type ($z = 4.11$, $p = 4 \times 10^{-4}$), a significant main effect of contact type ($z = 2.66$, $p = 0.008$) and a significant interaction cell \times contact type ($z = -5.09$, $p < 3.6 \times 10^{-7}$).

Data and code availability

Jupyter notebooks and data for reproducing our analysis and main figures are available online at https://github.com/berenslab/pr_bc_connectivity.

Table 3. Cross validation results of BC-to-rod contact classification.

	False positive	False negative	Total score
OFF-CBCs	18.3%	22.5%	0.8
RBCs	14.3%	2.6%	0.95

DOI: [10.7554/eLife.20041.023](https://doi.org/10.7554/eLife.20041.023)

Acknowledgements

We thank *Helmstaedter et al. (2013)* for making their data available. This work was funded by the DFG (EXC 307 and BE 5601/1–1) and the BMBF through the BCCN Tübingen (FKZ 01GQ1002) and the Bernstein Award to PB (FKZ 01GQ1601).

Additional information

Funding

Funder	Grant reference number	Author
Deutsche Forschungsgemeinschaft	EXC 307	Thomas Euler
Bundesministerium für Bildung und Forschung	FKZ 01GQ1601	Philipp Berens
Deutsche Forschungsgemeinschaft	BE 5601/1-1	Philipp Berens
Bundesministerium für Bildung und Forschung	FKZ 01GQ1002	Thomas Euler

The funders had no role in study design, data collection and interpretation, or the decision to submit the work for publication.

Author contributions

CB, Anatomical tracing, Analysis and interpretation of data, Drafting or revising the article; TS, Anatomical tracing, Conception and design, Analysis and interpretation of data, Drafting or revising the article; SH, TE, Conception and design, Drafting or revising the article; PB, Conception and design, Analysis and interpretation of data, Drafting or revising the article

Author ORCIDs

Thomas Euler, <http://orcid.org/0000-0002-4567-6966>

Philipp Berens, <http://orcid.org/0000-0002-0199-4727>

References

- Baden T, Schubert T, Chang L, Wei T, Zaichuk M, Wissinger B, Euler T. 2013. A tale of two retinal domains: near-optimal sampling of achromatic contrasts in natural scenes through asymmetric photoreceptor distribution. *Neuron* **80**:1206–1217. doi: [10.1016/j.neuron.2013.09.030](https://doi.org/10.1016/j.neuron.2013.09.030), PMID: [24314730](https://pubmed.ncbi.nlm.nih.gov/24314730/)
- Bishop CM. 2006. *Pattern Recognition and Machine Learning*. New York: Springer
- Blakemore CB, Rushton WA. 1965. Dark adaptation and increment threshold in a rod monochromat. *The Journal of Physiology* **181**:612–628. doi: [10.1113/jphysiol.1965.sp007786](https://doi.org/10.1113/jphysiol.1965.sp007786), PMID: [5880380](https://pubmed.ncbi.nlm.nih.gov/5880380/)
- Bloomfield SA, Dacheux RF. 2001. Rod vision: pathways and processing in the mammalian retina. *Progress in Retinal and Eye Research* **20**:351–384. doi: [10.1016/S1350-9462\(00\)00031-8](https://doi.org/10.1016/S1350-9462(00)00031-8), PMID: [11286897](https://pubmed.ncbi.nlm.nih.gov/11286897/)
- Bloomfield SA, Xin D, Osborne T. 1997. Light-induced modulation of coupling between aii amacrine cells in the rabbit retina. *Visual Neuroscience* **14**:565–576. doi: [10.1017/S0952523800012220](https://doi.org/10.1017/S0952523800012220), PMID: [9194323](https://pubmed.ncbi.nlm.nih.gov/9194323/)
- Boycott BB, Wässle H. 1991. Morphological classification of bipolar cells of the primate retina. *European Journal of Neuroscience* **3**:1069–1088. doi: [10.1111/j.1460-9568.1991.tb00043.x](https://doi.org/10.1111/j.1460-9568.1991.tb00043.x), PMID: [12106238](https://pubmed.ncbi.nlm.nih.gov/12106238/)
- Breuninger T, Puller C, Haverkamp S, Euler T. 2011. Chromatic bipolar cell pathways in the mouse retina. *Journal of Neuroscience* **31**:6504–6517. doi: [10.1523/JNEUROSCI.0616-11.2011](https://doi.org/10.1523/JNEUROSCI.0616-11.2011), PMID: [21525291](https://pubmed.ncbi.nlm.nih.gov/21525291/)
- Calkins DJ, Tsukamoto Y, Sterling P. 1996. Foveal cones form basal as well as invaginating junctions with diffuse on bipolar cells. *Vision Research* **36**:3373–3381. doi: [10.1016/0042-6989\(95\)00333-9](https://doi.org/10.1016/0042-6989(95)00333-9), PMID: [8977004](https://pubmed.ncbi.nlm.nih.gov/8977004/)
- Chun MH, Grünert U, Martin PR, Wässle H. 1996. The synaptic complex of cones in the fovea and in the periphery of the macaque monkey retina. *Vision Research* **36**:3383–3395. doi: [10.1016/0042-6989\(95\)00334-7](https://doi.org/10.1016/0042-6989(95)00334-7), PMID: [8977005](https://pubmed.ncbi.nlm.nih.gov/8977005/)
- Della Santina L, Kuo SP, Yoshimatsu T, Okawa H, Suzuki SC, Hoon M, Tsuboyama K, Rieke F, Wong RO. 2016. Glutamatergic monopolar interneurons provide a novel pathway of excitation in the mouse retina. *Current Biology* **26**:2070–2077. doi: [10.1016/j.cub.2016.06.016](https://doi.org/10.1016/j.cub.2016.06.016), PMID: [27426514](https://pubmed.ncbi.nlm.nih.gov/27426514/)
- DeVries SH, Li W, Saszik S. 2006. Parallel processing in two transmitter microenvironments at the cone photoreceptor synapse. *Neuron* **50**:735–748. doi: [10.1016/j.neuron.2006.04.034](https://doi.org/10.1016/j.neuron.2006.04.034), PMID: [16731512](https://pubmed.ncbi.nlm.nih.gov/16731512/)
- Dowling JE, Boycott BB. 1966. Organization of the Primate Retina: Electron Microscopy. *Proceedings of the Royal Society B: Biological Sciences* **166**:80–111. doi: [10.1098/rspb.1966.0086](https://doi.org/10.1098/rspb.1966.0086)

- Dunn FA, Wong RO. 2012. Diverse strategies engaged in establishing stereotypic wiring patterns among neurons sharing a common input at the visual system's first synapse. *Journal of Neuroscience* **32**:10306–10317. doi: [10.1523/JNEUROSCI.1581-12.2012](https://doi.org/10.1523/JNEUROSCI.1581-12.2012), PMID: [22836264](https://pubmed.ncbi.nlm.nih.gov/22836264/)
- Euler T, Haverkamp S, Schubert T, Baden T. 2014. Retinal bipolar cells: elementary building blocks of vision. *Nature Reviews Neuroscience* **15**:507–519. doi: [10.1038/nrn3783](https://doi.org/10.1038/nrn3783), PMID: [25158357](https://pubmed.ncbi.nlm.nih.gov/25158357/)
- Franke K, Berens P, Schubert T, Bethge M, Euler T, Baden T. 2016. Balanced excitation and inhibition decorrelates visual feature representation in the mammalian inner retina. *bioRxiv*. doi: [10.1101/040642](https://doi.org/10.1101/040642).
- Greene MJ, Kim JS, Seung HS, EyeWriters. 2016. Analogous convergence of sustained and transient inputs in parallel on and off pathways for retinal motion computation. *Cell Reports* **14**:1892–1900. doi: [10.1016/j.celrep.2016.02.001](https://doi.org/10.1016/j.celrep.2016.02.001), PMID: [26904938](https://pubmed.ncbi.nlm.nih.gov/26904938/)
- Hack I, Peichl L, Brandstätter JH. 1999. An alternative pathway for rod signals in the rodent retina: rod photoreceptors, cone bipolar cells, and the localization of glutamate receptors. *PNAS* **96**:14130–14135. doi: [10.1073/pnas.96.24.14130](https://doi.org/10.1073/pnas.96.24.14130), PMID: [10570210](https://pubmed.ncbi.nlm.nih.gov/10570210/)
- Haverkamp S, Grünert U, Wässle H. 2000. The cone pedicle, a complex synapse in the retina. *Neuron* **27**:85–95. doi: [10.1016/S0896-6273\(00\)00011-8](https://doi.org/10.1016/S0896-6273(00)00011-8), PMID: [10939333](https://pubmed.ncbi.nlm.nih.gov/10939333/)
- Haverkamp S, Specht D, Majumdar S, Zaidi NF, Brandstätter JH, Wasco W, Wässle H, Tom Dieck S. 2008. Type 4 OFF cone bipolar cells of the mouse retina express calnenilin and contact cones as well as rods. *The Journal of Comparative Neurology* **507**:1087–1101. doi: [10.1002/cne.21612](https://doi.org/10.1002/cne.21612), PMID: [18095322](https://pubmed.ncbi.nlm.nih.gov/18095322/)
- Haverkamp S, Wässle H, Duebel J, Kuner T, Augustine GJ, Feng G, Euler T. 2005. The primordial, blue-cone color system of the mouse retina. *Journal of Neuroscience* **25**:5438–5445. doi: [10.1523/JNEUROSCI.1117-05.2005](https://doi.org/10.1523/JNEUROSCI.1117-05.2005), PMID: [15930394](https://pubmed.ncbi.nlm.nih.gov/15930394/)
- Helmstaedter M, Briggman KL, Denk W. 2012. High-accuracy neurite reconstruction for high-throughput neuroanatomy. *Nature Neuroscience* **14**:1081–1088. doi: [10.1038/nn.2868](https://doi.org/10.1038/nn.2868)
- Helmstaedter M, Briggman KL, Turaga SC, Jain V, Seung HS, Denk W. 2013. Connectomic reconstruction of the inner plexiform layer in the mouse retina. *Nature* **500**:168–174. doi: [10.1038/nature12346](https://doi.org/10.1038/nature12346), PMID: [23925239](https://pubmed.ncbi.nlm.nih.gov/23925239/)
- Hopkins JM, Boycott BB. 1995. Synapses between cones and diffuse bipolar cells of a primate retina. *Journal of Neurocytology* **24**:680–694. doi: [10.1007/BF01179818](https://doi.org/10.1007/BF01179818), PMID: [7500123](https://pubmed.ncbi.nlm.nih.gov/7500123/)
- Hopkins JM, Boycott BB. 1996. The cone synapses of DB1 diffuse, DB6 diffuse and invaginating midget, bipolar cells of a primate retina. *Journal of Neurocytology* **25**:381–390. PMID: [8866239](https://pubmed.ncbi.nlm.nih.gov/8866239/)
- Ichinose T, Fyk-Kolodziej B, Cohn J. 2014. Roles of ON cone bipolar cell subtypes in temporal coding in the mouse retina. *Journal of Neuroscience* **34**:8761–8771. doi: [10.1523/JNEUROSCI.3965-13.2014](https://doi.org/10.1523/JNEUROSCI.3965-13.2014), PMID: [24966376](https://pubmed.ncbi.nlm.nih.gov/24966376/)
- Joo HR, Peterson BB, Haun TJ, Dacey DM. 2011. Characterization of a novel large-field cone bipolar cell type in the primate retina: evidence for selective cone connections. *Visual Neuroscience* **28**:29–37. doi: [10.1017/S0952523810000374](https://doi.org/10.1017/S0952523810000374), PMID: [21156090](https://pubmed.ncbi.nlm.nih.gov/21156090/)
- Kolb H. 1970. Organization of the outer plexiform layer of the primate retina: electron microscopy of Golgi-impregnated cells. *Philosophical Transactions of the Royal Society B: Biological Sciences* **258**:261–283. doi: [10.1098/rstb.1970.0036](https://doi.org/10.1098/rstb.1970.0036), PMID: [22408829](https://pubmed.ncbi.nlm.nih.gov/22408829/)
- Kouyama N, Marshak DW. 1992. Bipolar cells specific for blue cones in the macaque retina. *Journal of Neuroscience* **12**:1233–1252. PMID: [1556594](https://pubmed.ncbi.nlm.nih.gov/1556594/)
- Kuo SP, Schwartz GW, Rieke F. 2016. Nonlinear spatiotemporal integration by electrical and chemical synapses in the retina. *Neuron* **90**:320–332. doi: [10.1016/j.neuron.2016.03.012](https://doi.org/10.1016/j.neuron.2016.03.012), PMID: [27068789](https://pubmed.ncbi.nlm.nih.gov/27068789/)
- Mariani AP. 1984. Bipolar cells in monkey retina selective for the cones likely to be blue-sensitive. *Nature* **308**:184–186. doi: [10.1038/308184a0](https://doi.org/10.1038/308184a0), PMID: [6199677](https://pubmed.ncbi.nlm.nih.gov/6199677/)
- Mataruga A, Kremmer E, Müller F. 2007. Type 3a and type 3b OFF cone bipolar cells provide for the alternative rod pathway in the mouse retina. *The Journal of Comparative Neurology* **502**:1123–1137. doi: [10.1002/cne.21367](https://doi.org/10.1002/cne.21367), PMID: [17447251](https://pubmed.ncbi.nlm.nih.gov/17447251/)
- Molnar A, Werblin F. 2007. Inhibitory feedback shapes bipolar cell responses in the rabbit retina. *Journal of Neurophysiology* **98**:3423–3435. doi: [10.1152/jn.00838.2007](https://doi.org/10.1152/jn.00838.2007), PMID: [17928553](https://pubmed.ncbi.nlm.nih.gov/17928553/)
- Pang JJ, Gao F, Lem J, Bramblett DE, Paul DL, Wu SM. 2010. Direct rod input to cone BCs and direct cone input to rod BCs challenge the traditional view of mammalian BC circuitry. *PNAS* **107**:395–400. doi: [10.1073/pnas.0907178107](https://doi.org/10.1073/pnas.0907178107), PMID: [20018684](https://pubmed.ncbi.nlm.nih.gov/20018684/)
- Puller C, Ivanova E, Euler T, Haverkamp S, Schubert T. 2013. OFF bipolar cells express distinct types of dendritic glutamate receptors in the mouse retina. *Neuroscience* **243**:136–148. doi: [10.1016/j.neuroscience.2013.03.054](https://doi.org/10.1016/j.neuroscience.2013.03.054), PMID: [23567811](https://pubmed.ncbi.nlm.nih.gov/23567811/)
- Röhlich P, van Veen T, Szél A. 1994. Two different visual pigments in one retinal cone cell. *Neuron* **13**:1159–1166. doi: [10.1016/0896-6273\(94\)90053-1](https://doi.org/10.1016/0896-6273(94)90053-1), PMID: [7946352](https://pubmed.ncbi.nlm.nih.gov/7946352/)
- Seung HS, Sümbül U. 2014. Neuronal cell types and connectivity: lessons from the retina. *Neuron* **83**:1262–1272. doi: [10.1016/j.neuron.2014.08.054](https://doi.org/10.1016/j.neuron.2014.08.054), PMID: [25233310](https://pubmed.ncbi.nlm.nih.gov/25233310/)
- Shekhar K, Lapan SW, Whitney IE, Tran NM, Macosko EZ, Kowalczyk M, Adiconis X, Levin JZ, Nemesh J, Goldman M, McCarroll SA, Cepko CL, Regev A, Sanes JR. 2016. Comprehensive classification of retinal bipolar neurons by single-cell transcriptomics. *Cell* **166**:1308–1323.e30. doi: [10.1016/j.cell.2016.07.054](https://doi.org/10.1016/j.cell.2016.07.054), PMID: [27565351](https://pubmed.ncbi.nlm.nih.gov/27565351/)
- Szmajda BA, Devries SH. 2011. Glutamate spillover between mammalian cone photoreceptors. *Journal of Neuroscience* **31**:13431–13441. doi: [10.1523/JNEUROSCI.2105-11.2011](https://doi.org/10.1523/JNEUROSCI.2105-11.2011), PMID: [21940436](https://pubmed.ncbi.nlm.nih.gov/21940436/)

- Tikidji-Hamburyan A**, Reinhard K, Seitter H, Hovhannisyan A, Procyk CA, Allen AE, Schenk M, Lucas RJ, Münch TA. 2015. Retinal output changes qualitatively with every change in ambient illuminance. *Nature Neuroscience* **18**:66–74. doi: [10.1038/nn.3891](https://doi.org/10.1038/nn.3891), PMID: [25485757](https://pubmed.ncbi.nlm.nih.gov/25485757/)
- Tsukamoto Y**, Morigiwa K, Ishii M, Takao M, Iwatsuki K, Nakanishi S, Fukuda Y. 2007. A novel connection between rods and on cone bipolar cells revealed by ectopic metabotropic glutamate receptor 7 (mGluR7) in mGluR6-deficient mouse retinas. *Journal of Neuroscience* **27**:6261–6267. doi: [10.1523/JNEUROSCI.5646-06.2007](https://doi.org/10.1523/JNEUROSCI.5646-06.2007), PMID: [17553999](https://pubmed.ncbi.nlm.nih.gov/17553999/)
- Tsukamoto Y**, Omi N. 2013. Functional allocation of synaptic contacts in microcircuits from rods via rod bipolar to All amacrine cells in the mouse retina. *Journal of Comparative Neurology* **521**:3541–3555. doi: [10.1002/cne.23370](https://doi.org/10.1002/cne.23370), PMID: [23749582](https://pubmed.ncbi.nlm.nih.gov/23749582/)
- Tsukamoto Y**, Omi N. 2014. Some OFF bipolar cell types make contact with both rods and cones in macaque and mouse retinas. *Frontiers in Neuroanatomy* **8**:105. doi: [10.3389/fnana.2014.00105](https://doi.org/10.3389/fnana.2014.00105), PMID: [25309346](https://pubmed.ncbi.nlm.nih.gov/25309346/)
- Tsukamoto Y**, Omi N. 2016. ON bipolar cells in macaque retina: type-specific synaptic connectivity with special reference to OFF counterparts. *Frontiers in Neuroanatomy* **10**:104. doi: [10.3389/fnana.2016.00104](https://doi.org/10.3389/fnana.2016.00104), PMID: [27833534](https://pubmed.ncbi.nlm.nih.gov/27833534/)
- Wässle H**, Puller C, Müller F, Haverkamp S. 2009. Cone contacts, mosaics, and territories of bipolar cells in the mouse retina. *Journal of Neuroscience* **29**:106–117. doi: [10.1523/JNEUROSCI.4442-08.2009](https://doi.org/10.1523/JNEUROSCI.4442-08.2009), PMID: [19129389](https://pubmed.ncbi.nlm.nih.gov/19129389/)



Figures and figure supplements

Connectivity map of bipolar cells and photoreceptors in the mouse retina

Christian Behrens *et al*

Figure 1. Identification of S- and M-cones. (A) Scheme showing vertical section through the mouse retina. (B) Volume-reconstructed cones and all CBC4 cells. (C) Cone pedicles (grey) with CBC9s. BC soma localization is indicated by colored dots. Dashed outlines indicate incomplete cones. (D) Same as in C, but with putative S-cones (blue) and M-cones (green) highlighted. Unidentified cones are shown in grey. Insets indicate the location of the examples shown below of cone pedicles contacted by CBC9 dendrites. (E) Contact parameters used for S-cone identification. ONL, outer nuclear layer; OPL, outer plexiform layer; INL, inner nuclear layer; IPL, inner plexiform layer; GCL, ganglion cell layer.
DOI: [10.7554/eLife.20041.002](https://doi.org/10.7554/eLife.20041.002)

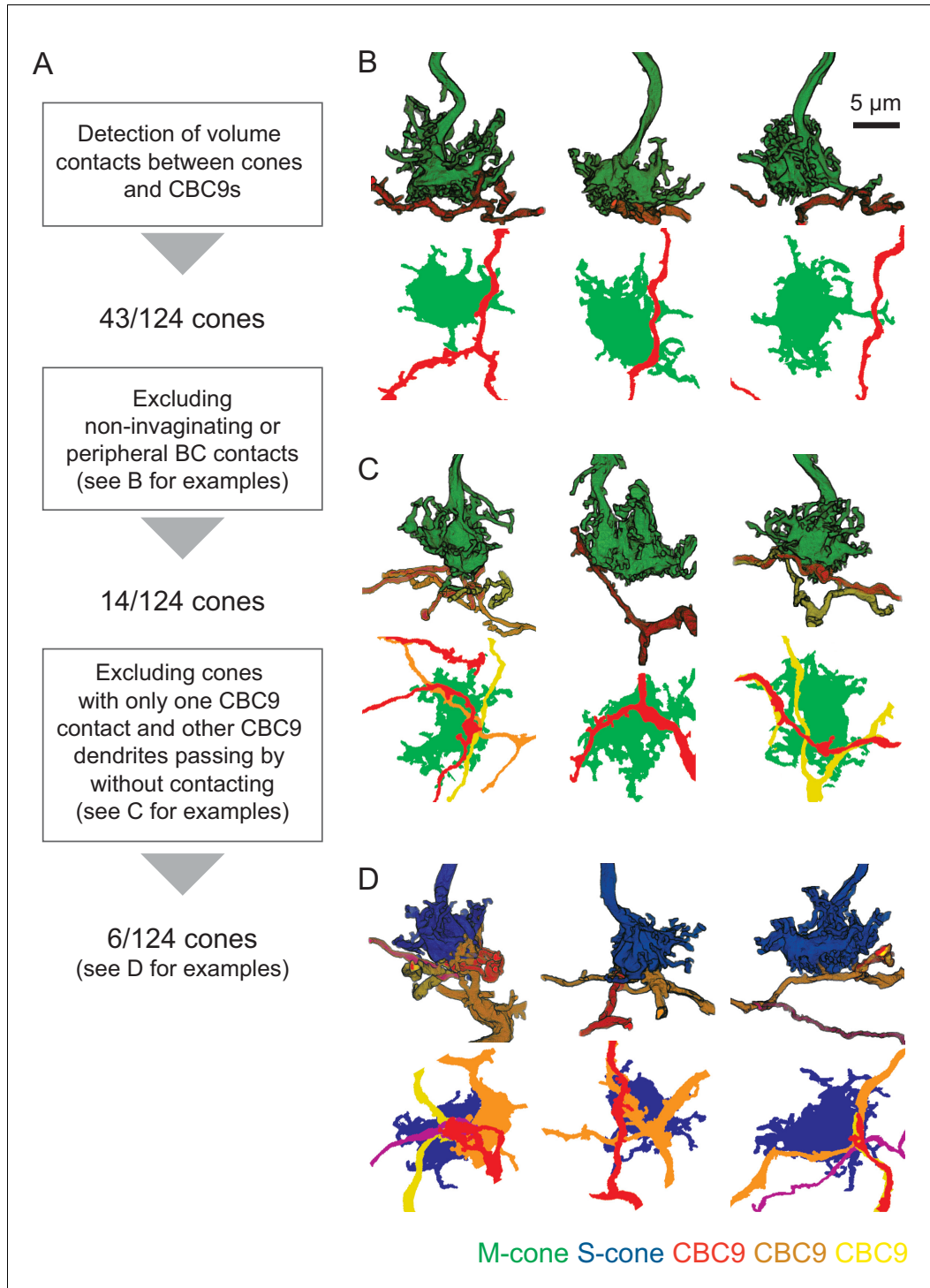


Figure 1—figure supplement 1. Details on the identification of S-cones. (A) Diagram showing workflow for identification of S- and M-cones using connectivity with CBC9 cells. (B–D) Side view and horizontal projection of representative examples of cone pedicles (green, M-cone; blue, S-cone) with CBC9 dendrites (red, yellow, orange) in side and horizontal views. (B) Side view of representative examples of cone pedicles (green, M-cone; blue, S-cone) with CBC9 dendrites (red, yellow, orange) in side and horizontal views. (C) Side view of representative examples of cone pedicles (green, M-cone; blue, S-cone) with CBC9 dendrites (red, yellow, orange) in side and horizontal views. (D) Side view of representative examples of cone pedicles (green, M-cone; blue, S-cone) with CBC9 dendrites (red, yellow, orange) in side and horizontal views. Figure 1—figure supplement 1 continued on next page

Figure 1—figure supplement 1 continued

CBC9 dendrites (yellow, orange, red) with non-invaginating but peripheral contacts (B), with only one CBC9 contact and other CBC9 dendrites passing by (C) and 'true' S-cones (D).

DOI: [10.7554/eLife.20041.003](https://doi.org/10.7554/eLife.20041.003)

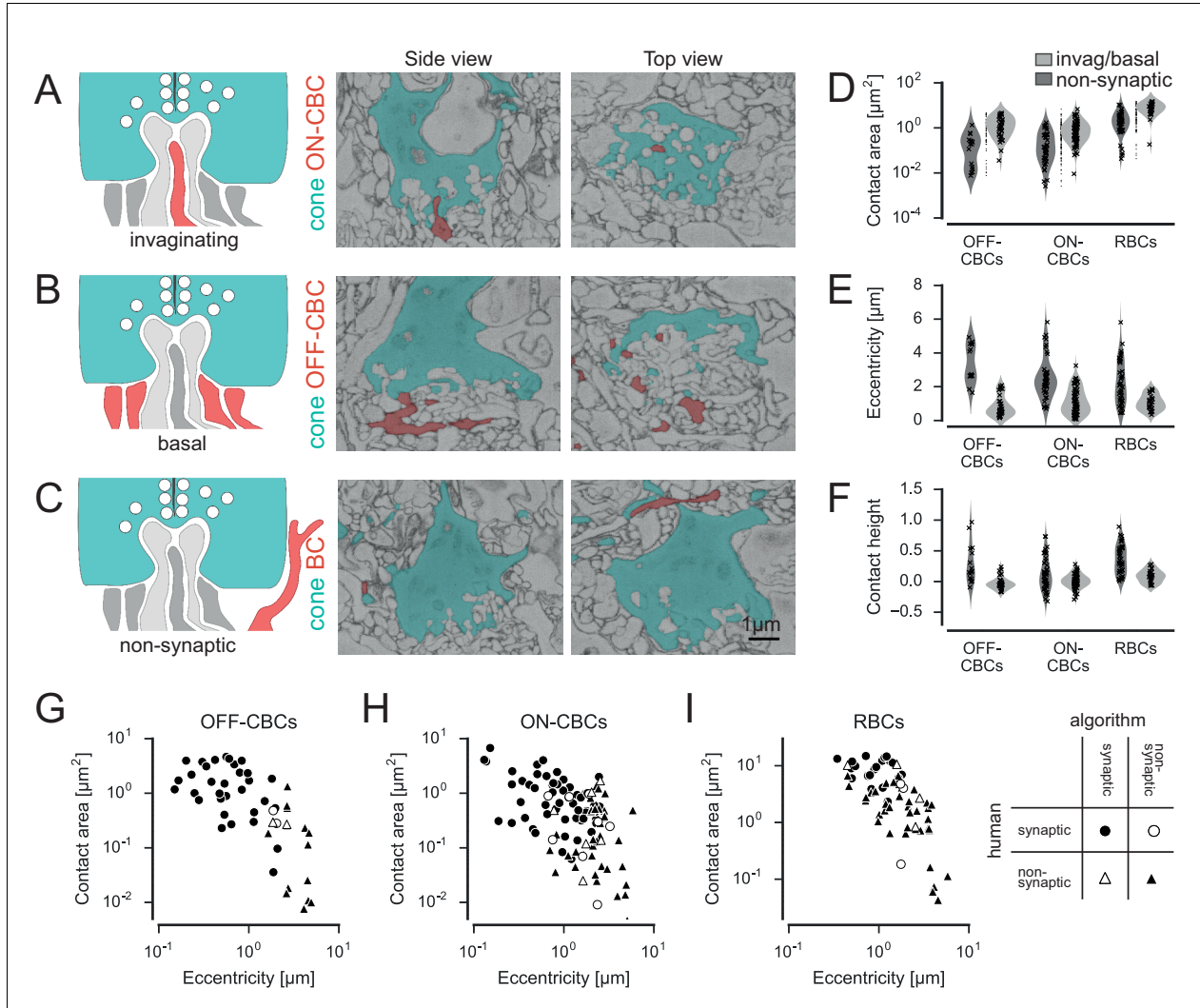


Figure 2. Classification of cone contacts. (A) Invaginating ON-CBC contact. Schematic drawing (left), EM side view (center) and top view (right). Red and dark grey, BC dendrites; light grey, horizontal cell dendrites; cyan, cone pedicles. (B) Basal/flat OFF-CBC contact as in A. (C) Peripheral (non-synaptic) BC contact as in A. (D–F) Contact area (D) eccentricity (E) contact height (F) of invaginating/basal and non-synaptic contacts for OFF-/ON-CBCs and rod bipolar cells (RBCs). (G–I) Contact area versus eccentricity for OFF-CBC (G), ON-CBC (H) and RBC (I) contacts indicating correctly and incorrectly classified contacts.

DOI: 10.7554/eLife.20041.004

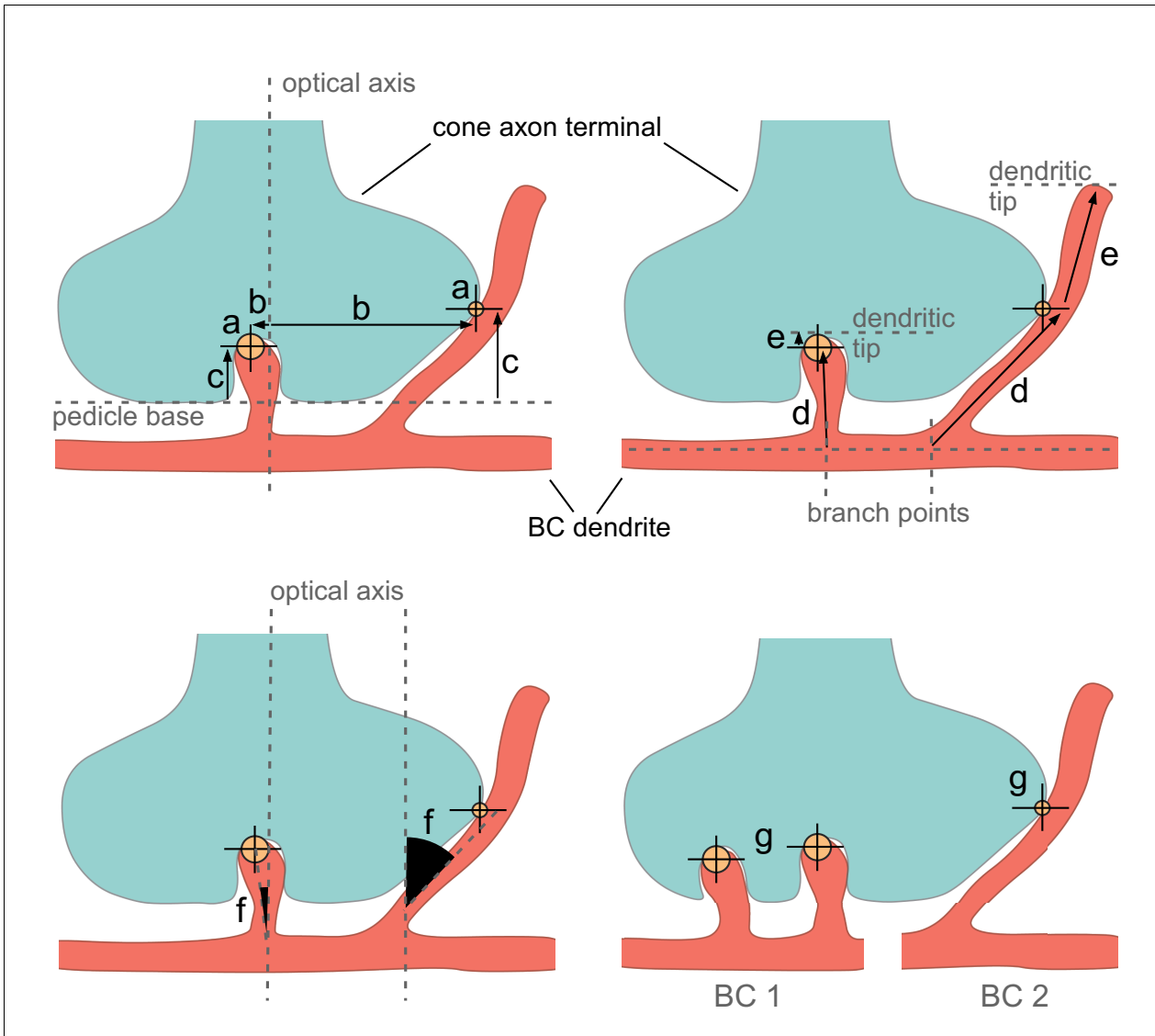


Figure 2—figure supplement 1. Illustration of parameters used for classifying contacts. Cone pedicle schemes showing the parameter used for automated contact classification: Contact area (a), eccentricity (b), contact height (c), distances to branch point (d) and dendritic tip (e), smallest angle between contacting dendrite and optical axis (f) and number of contact points between cone pedicle and BC (g). Example invaginating and peripheral contacts between cone (cyan) and BC dendrite(s) (red) are shown as large and small yellow circles, respectively. The optical axis is defined as a perpendicular through the center of the cone pedicle. BC, bipolar cell.

DOI: 10.7554/eLife.20041.005

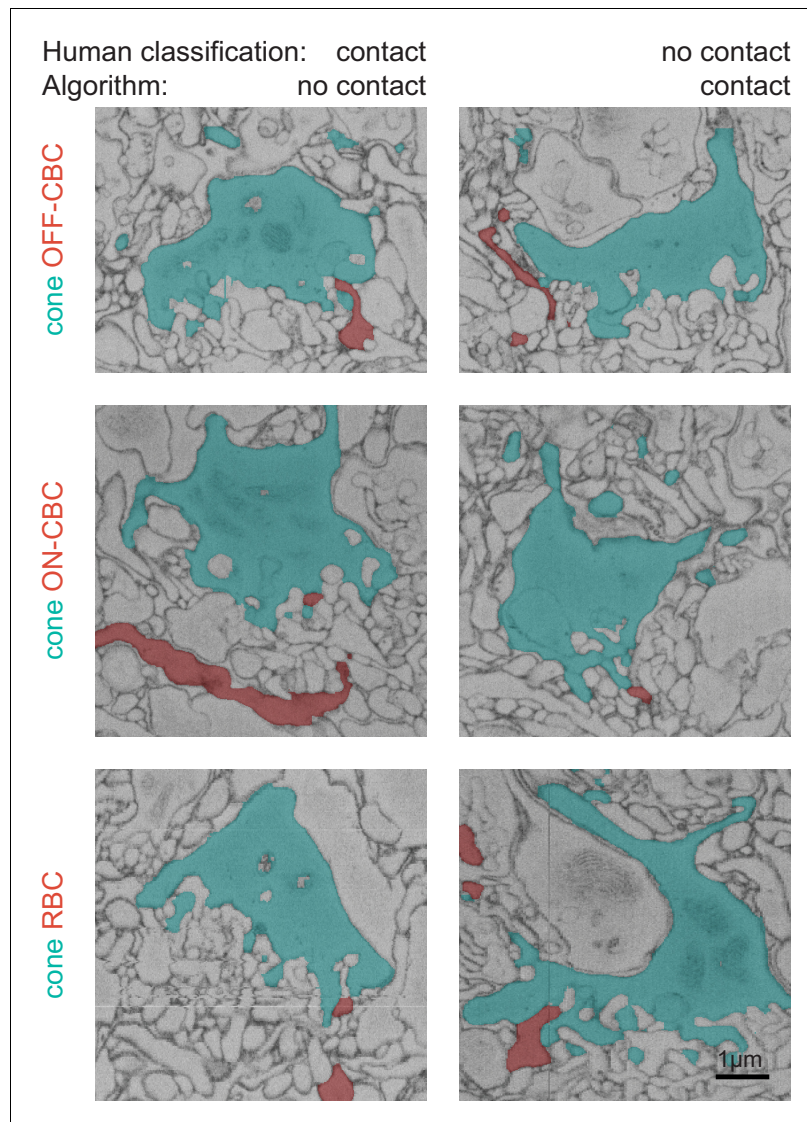


Figure 2—figure supplement 2. Examples for disagreements between human and algorithmic classification. EM slices (side view) showing examples of contacts where the automated contact classification did not match the human label. See also animated versions ([Video 1](#) and [2](#)).

DOI: [10.7554/eLife.20041.006](https://doi.org/10.7554/eLife.20041.006)

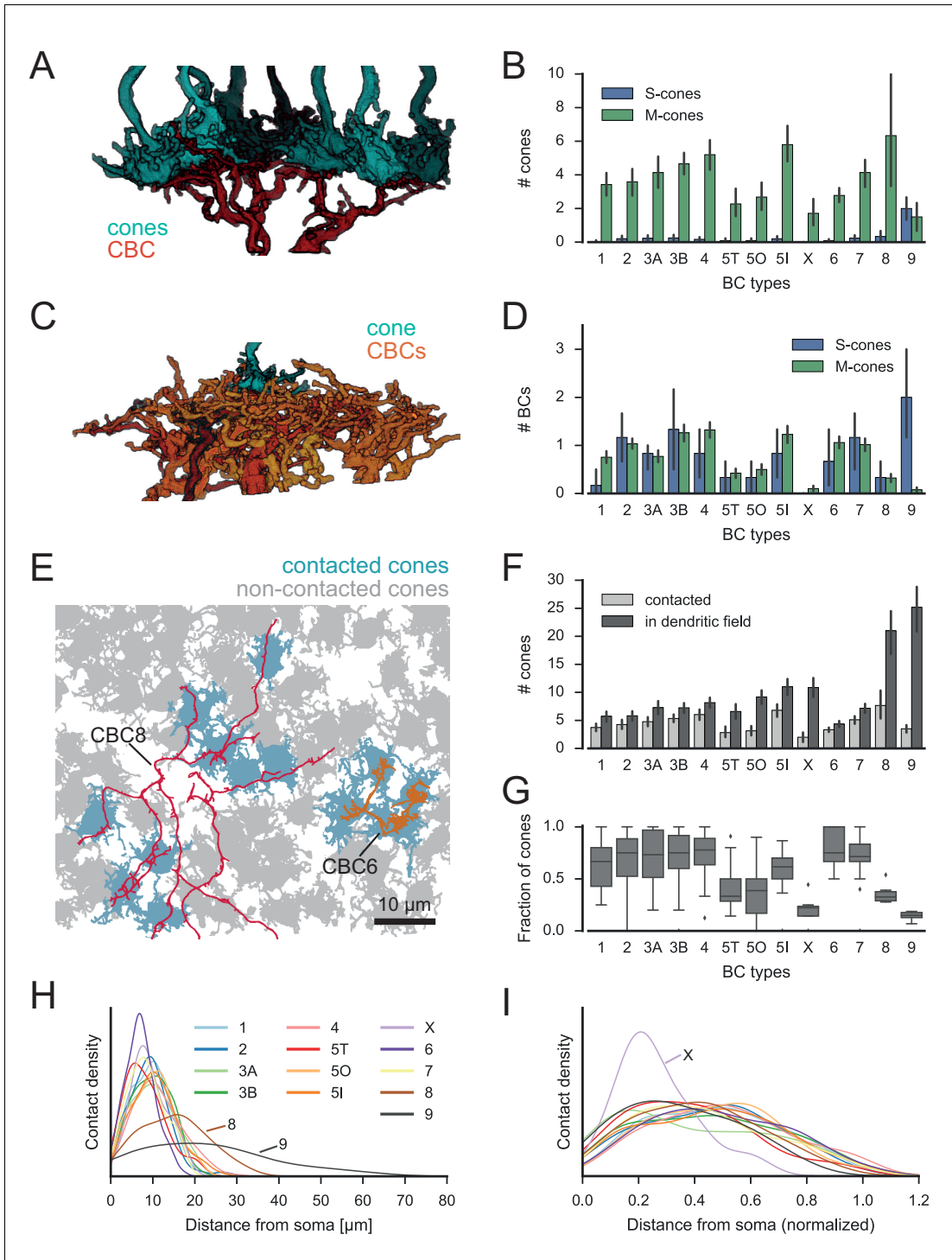


Figure 3. Quantification of cone-to-CBC contacts. (A) Volume-reconstructed single BC dendrite (red) contacting numerous cone pedicles (cyan). (B) Number of S- and M-cones contacted by different CBC types. (C) Volume-reconstructed single cone (cyan) contacted by multiple BCs (orange/red). (D) Figure 3 continued on next page

Figure 3 continued

Number of CBCs per type contacted by individual S- and M-cones. (E) Example cone array with CBC6 and CBC8 contacting cones. Grey, non-contacted cones; blue, contacted cones. (F) Number of contacted cones and cones within dendritic field for different CBC types. (G) Fraction of contacted cones/cones within the dendritic field. (H) Kernel density estimate of the distribution of contacted cones as function of distance from BC somata. (I) Same as H. but distance normalized by dendritic field size. Bars in B,D,F indicate 95% CI.

DOI: [10.7554/eLife.20041.010](https://doi.org/10.7554/eLife.20041.010)

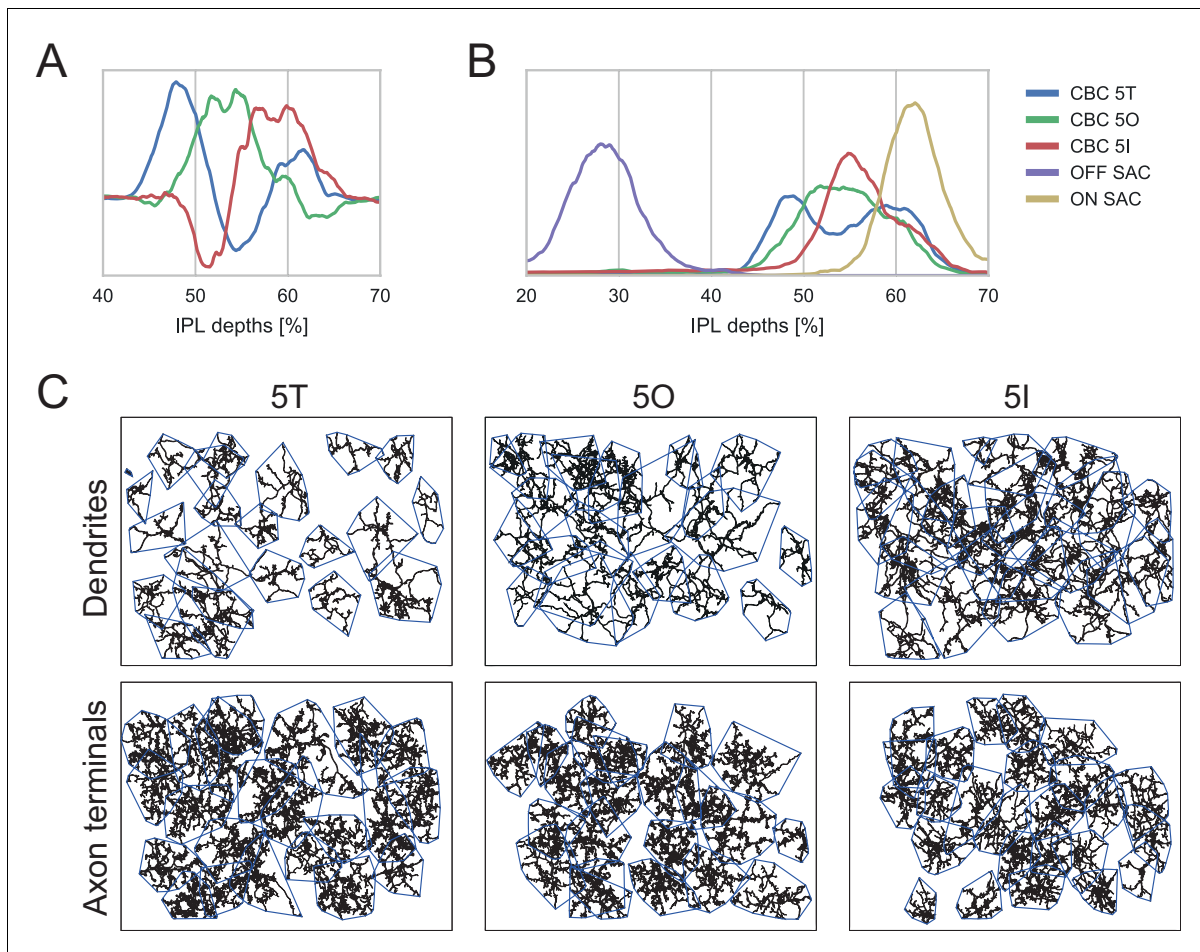


Figure 3—figure supplement 1. Classification of type 5 BCs. (A) First three PCA components for CBC5 density profiles in the IPL. (B) Stratification depth of CBC5T, 5O and 5I axon terminals in relation to the OFF- and ON-CHAT bands. (C) Dendritic (top) and axonal (bottom) mosaics for CBC5T, 5O and 5I cells.

DOI: [10.7554/eLife.20041.011](https://doi.org/10.7554/eLife.20041.011)

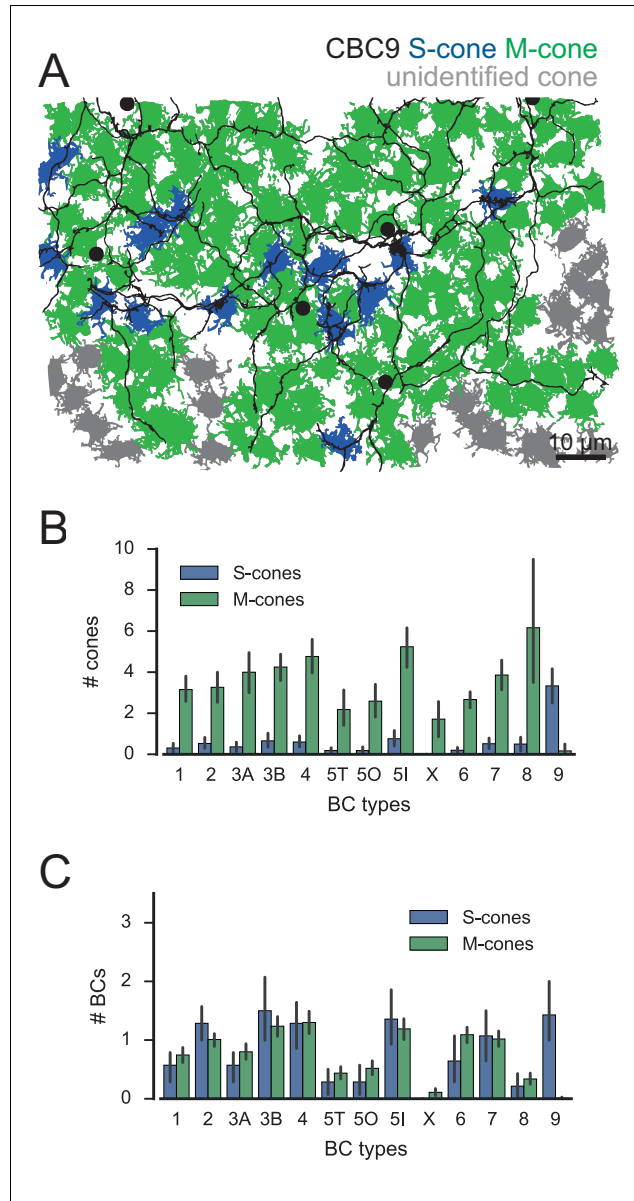


Figure 3—figure supplement 2. Connectivity analysis for alternative s-cone classification. (A) Cone pedicle array with CBC9s highlighted showing alternative S-cone classification. CBC9 somata are indicated by black dots, S-cones in blue, M-cones in green and unidentified cones in grey. (B) Number of S- and M-cones contacted by different BC types. (C) Number of BC types contacted by individual S- and M-cones. DOI: [10.7554/eLife.20041.012](https://doi.org/10.7554/eLife.20041.012)

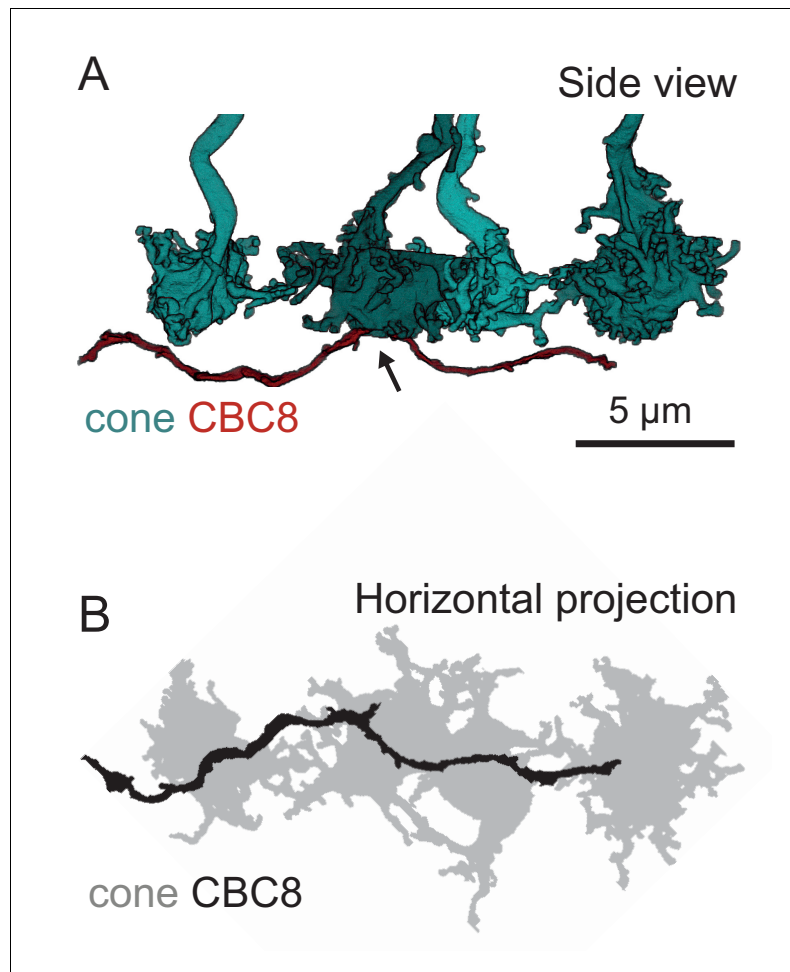


Figure 3—figure supplement 3. Example of a passing dendrite without contacts. (A) Side view of four volume-reconstructed cone pedicle (cyan) and CBC8 dendrite (red). (B) Horizontal projection of the neurite structures shown in (A). Arrow indicates the only invaginating ON-CBC contact along the dendrite.
DOI: [10.7554/eLife.20041.013](https://doi.org/10.7554/eLife.20041.013)

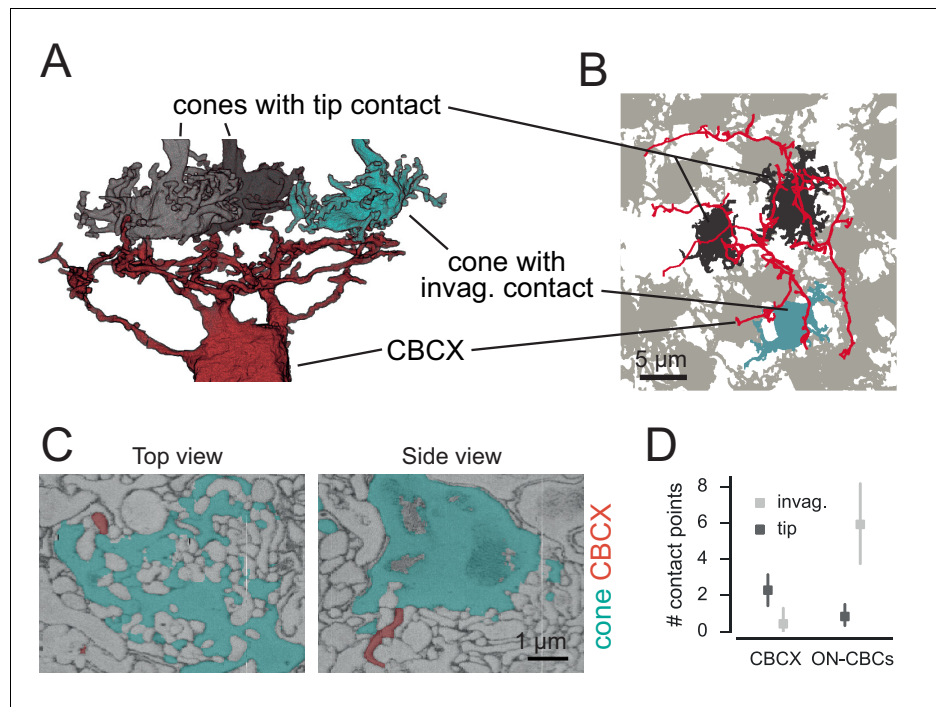


Figure 4. CBCX makes few and atypical cone contacts. (A) Volume-reconstructed CBCX dendritic arbor (red) contacting few cone pedicles (cyan, invaginating contact; grey, tip contact). (B) Same exemplary cone array as in A. with CBCX dendritic arbor contacting cones. Light grey, non-contacted cones; cyan, invaginating contacts; dark grey, tip contacts. (C) EM image showing tip contact between CBCX (red) and cone pedicles (cyan), top view (left) and side view (right). (D) Invaginating and tip contacts in CBCXs and other ON-CBCs. Bars in D. indicate 95% CI. DOI: [10.7554/eLife.20041.014](https://doi.org/10.7554/eLife.20041.014)

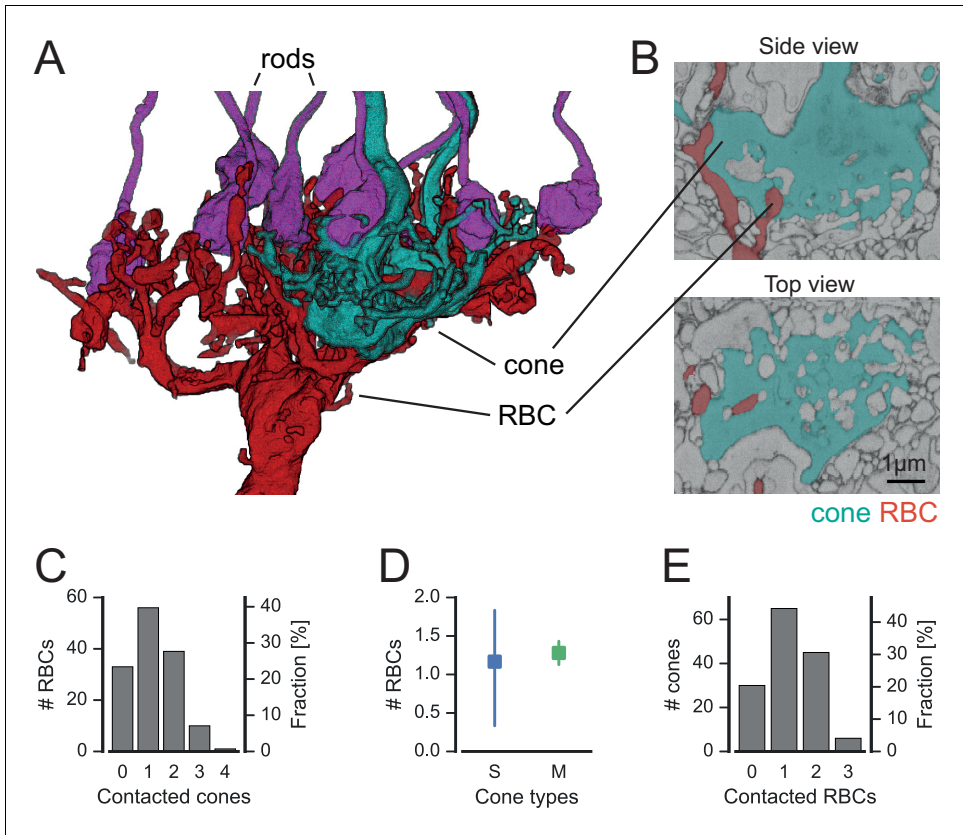


Figure 5. Cones contact rod bipolar cells. (A) Volume-reconstructed RBC (red) contacting both rods (magenta) and cone pedicles (cyan). (B) EM images showing invaginating contact between cone (cyan) and RBC (red), side view (top) and top view (bottom). (C) Number of RBCs contacted by cones. (D). Number of RBCs contacted by S- and M cones. (E) Number of cones contacted by RBCs. Bars in D. indicate 95% CI.

DOI: [10.7554/eLife.20041.015](https://doi.org/10.7554/eLife.20041.015)

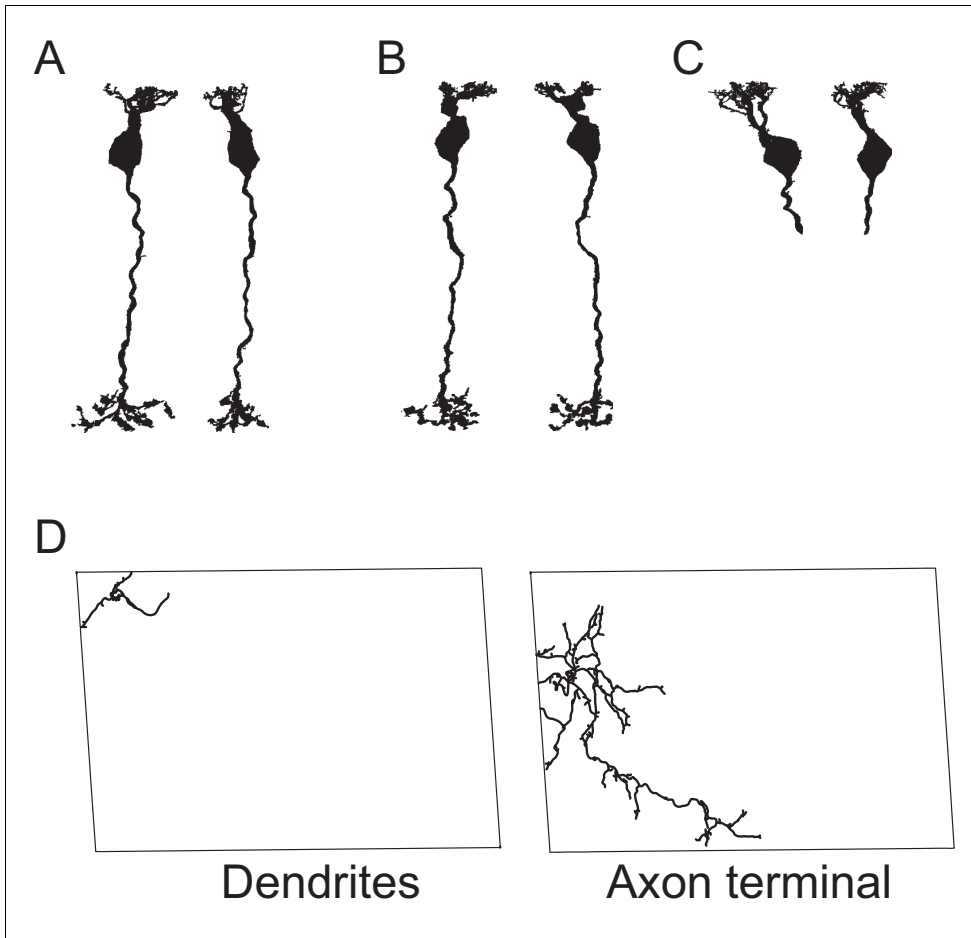


Figure 5—figure supplement 1. Excluded RBCs. (A–C) Three BCs classified as RBCs by *Helmstaedter et al. (2013)* but not contacting rods in the present study, these cells were therefore excluded from the analysis (for each cell two projections from different angles are shown). (D) BC classified as CBC9 but excluded from this study due to lack of complete dendritic tree.

DOI: [10.7554/eLife.20041.016](https://doi.org/10.7554/eLife.20041.016)

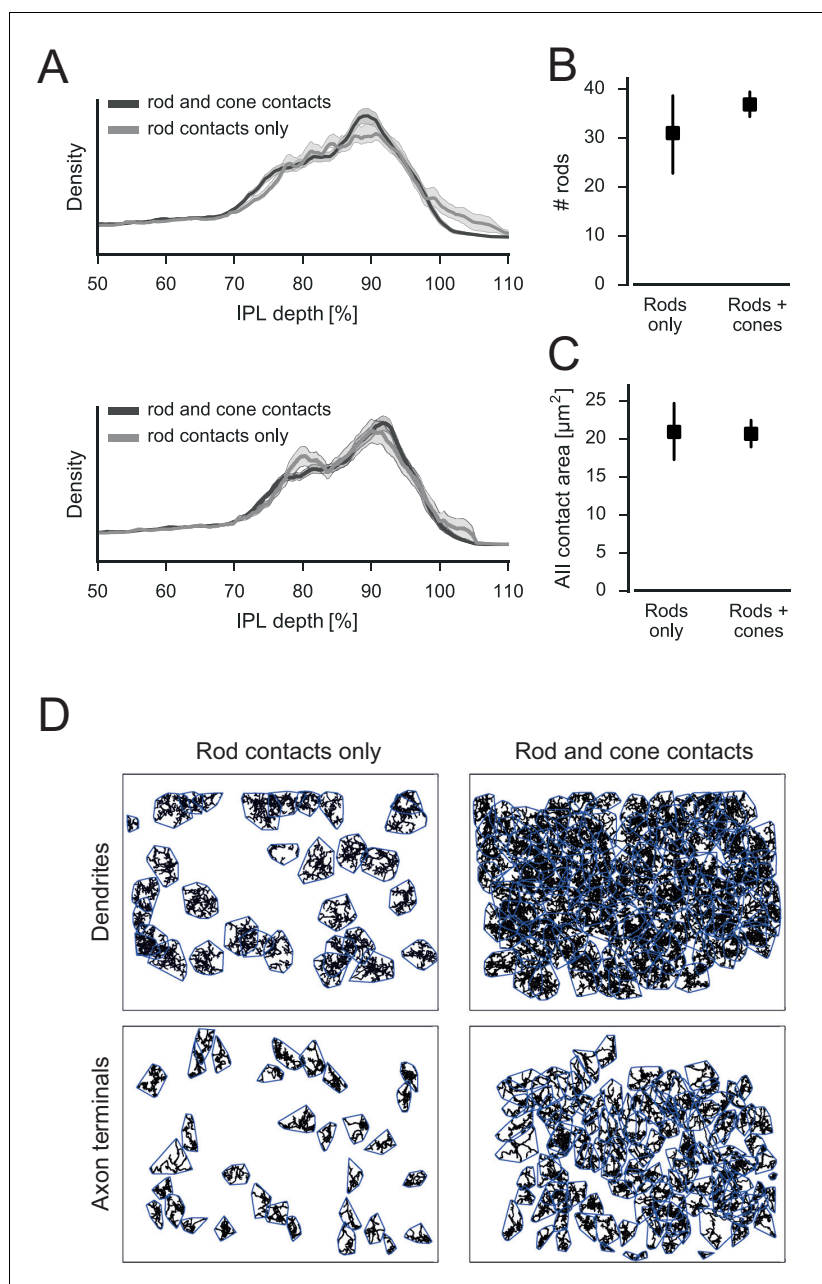


Figure 5—figure supplement 2. No evidence for two RBC subtypes. (A) Relative density of RBC spherules in the IPL using both dendritic ON and OFF starburst amacrine cell (SAC) bands (top) and only the dendritic ON SAC band (bottom) for depth correction (shading: SEM). (B) Number of rods contacted by RBCs contacting only rods or both rods and cones (95% confidence interval, CI). (C) Contact area with Alls for RBCs contacting only rods or both rods and cones (95% CI). (D) Dendritic (top) and axonal (bottom) mosaics for RBCs contacting rods or both rods and cones.

DOI: [10.7554/eLife.20041.017](https://doi.org/10.7554/eLife.20041.017)

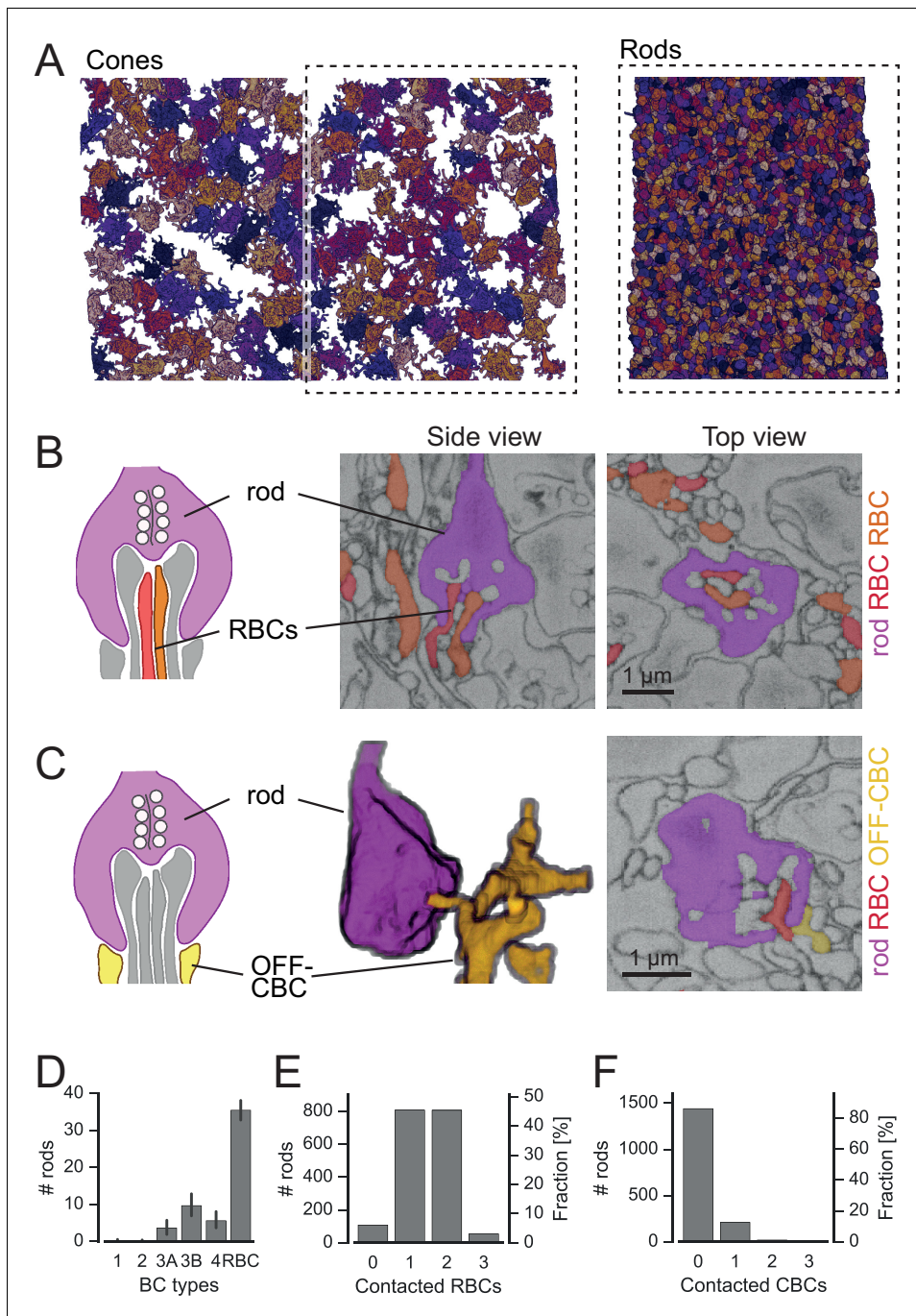


Figure 6. Rods contact RBCs and OFF-CBCs. (A) Volume-reconstructed, neighboring rod spherules (right) in one half of the field of the reconstructed cone pedicles (left). (B) Rod spherule (magenta) with invaginating dendrites of two RBCs (orange, red). Schematic drawing (left), EM images side view (middle) and top view (right). (C) Rod spherule (magenta) with basal contacts by OFF-CBCs (yellow). Schematic (left), volume-reconstructed vertical view (middle), EM image with top view (right). The latter also shows an invaginating RBC dendrite (red). (D–F). Number of rods (and fraction) contacted by RBCs (D,E), and OFF-CBC types (D, F). Bars in D, indicate 95% CI.

Figure 6 continued on next page

Figure 6 continued

DOI: [10.7554/eLife.20041.018](https://doi.org/10.7554/eLife.20041.018)

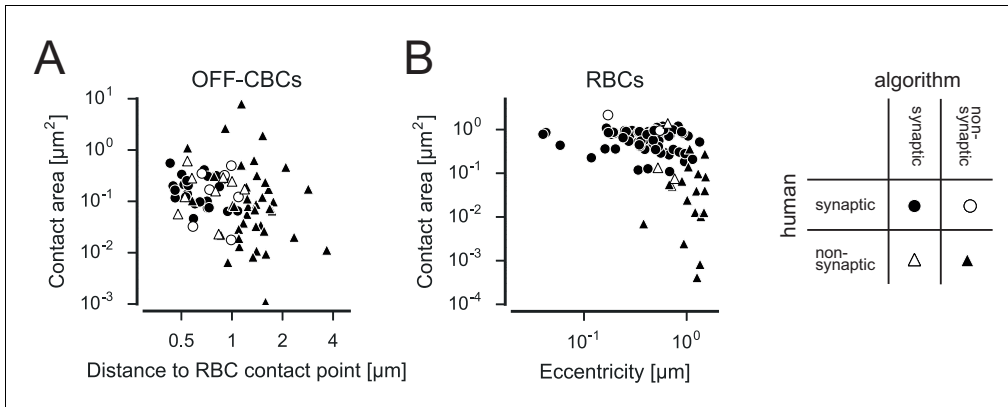


Figure 6—figure supplement 1. Classification of rod contact classification. Contact area versus distance to RBC contact point for OFF-CBC-rod contacts (A) and contact area versus eccentricity for RBCs (B) contacts indicating correctly and incorrectly classified contacts.
 DOI: [10.7554/eLife.20041.019](https://doi.org/10.7554/eLife.20041.019)

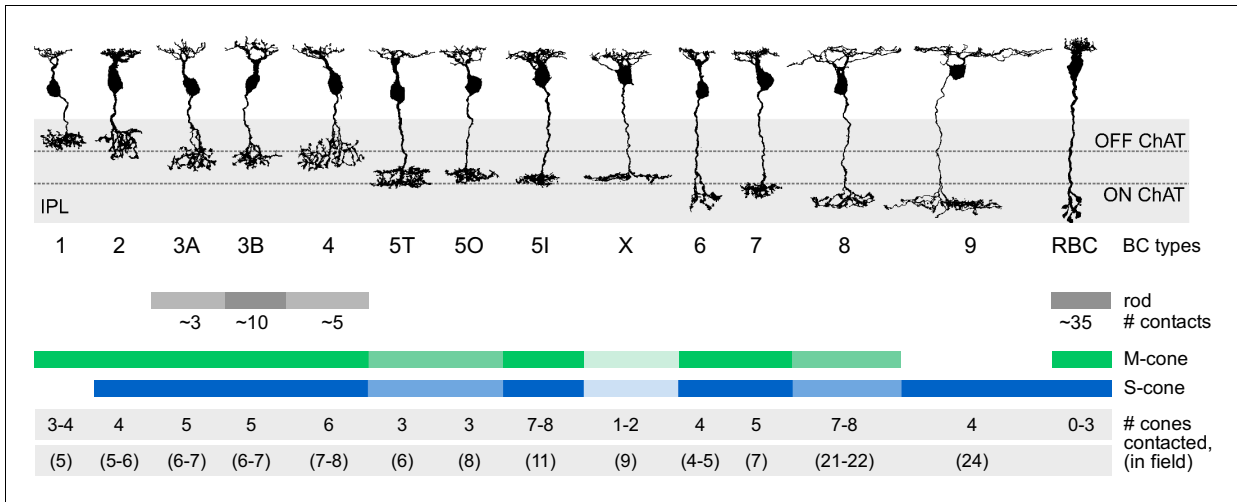


Figure 7. Connectivity between cone and rod photoreceptors and bipolar cells in the mouse retina. Representative examples of bipolar cell types in the mouse retina are shown. The number of cones in the dendritic field number and contacted photoreceptors are given for each type.
 DOI: [10.7554/eLife.20041.020](https://doi.org/10.7554/eLife.20041.020)

Current Biology

Local Signals in Mouse Horizontal Cell Dendrites

Highlights

- Light-evoked Ca²⁺ signals in horizontal cell dendrites reflect opsin gradient
- Chromatic preferences in neighboring dendritic tips vary markedly
- Mouse horizontal cells process cone photoreceptor input locally
- Local horizontal cell feedback shapes the temporal properties of cone output

Authors

Camille A. Chapot, Christian Behrens, Luke E. Rogerson, ..., Philipp Berens, Thomas Euler, Timm Schubert

Correspondence

thomas.euler@cin.uni-tuebingen.de (T.E.),
timm.schubert@cin.uni-tuebingen.de (T.S.)

In Brief

Chapot et al. show that local light responses in mouse horizontal cell dendrites inherit properties, including chromatic preference, from the presynaptic cone photoreceptor, suggesting that their dendrites can provide private feedback to cones, for instance, to shape the temporal filtering properties of the cone synapse.



Chapot et al., 2017, Current Biology 27, 3603–3615
December 4, 2017 © 2017 Elsevier Ltd.
<https://doi.org/10.1016/j.cub.2017.10.050>

CellPress

Local Signals in Mouse Horizontal Cell Dendrites

Camille A. Chapot,^{1,2,3} Christian Behrens,^{1,2,3,4} Luke E. Rogerson,^{1,2,3,4} Tom Baden,^{1,5} Sinziana Pop,^{1,2,3} Philipp Berens,^{1,2,4} Thomas Euler,^{1,2,4,*} and Timm Schubert^{1,2,6,*}

¹Institute for Ophthalmic Research, University of Tübingen, 72076 Tübingen, Germany

²Center for Integrative Neuroscience, University of Tübingen, 72076 Tübingen, Germany

³Graduate Training Centre of Neuroscience, University of Tübingen, 72076 Tübingen, Germany

⁴Bernstein Center for Computational Neuroscience, University of Tübingen, 72076 Tübingen, Germany

⁵School of Life Sciences, University of Sussex, Brighton BN1 9RH, UK

⁶Lead Contact

*Correspondence: thomas.euler@cin.uni-tuebingen.de (T.E.), timmschubert@cin.uni-tuebingen.de (T.S.)

<https://doi.org/10.1016/j.cub.2017.10.050>

SUMMARY

The mouse retina contains a single type of horizontal cell, a GABAergic interneuron that samples from all cone photoreceptors within reach and modulates their glutamatergic output via parallel feedback mechanisms. Because horizontal cells form an electrically coupled network, they have been implicated in global signal processing, such as large-scale contrast enhancement. Recently, it has been proposed that horizontal cells can also act locally at the level of individual cone photoreceptors. To test this possibility physiologically, we used two-photon microscopy to record light stimulus-evoked Ca^{2+} signals in cone axon terminals and horizontal cell dendrites as well as glutamate release in the outer plexiform layer. By selectively stimulating the two mouse cone opsins with green and UV light, we assessed whether signals from individual cones remain isolated within horizontal cell dendritic tips or whether they spread across the dendritic arbor. Consistent with the mouse's opsin expression gradient, we found that the Ca^{2+} signals recorded from dendrites of dorsal horizontal cells were dominated by M-opsin and those of ventral horizontal cells by S-opsin activation. The signals measured in neighboring horizontal cell dendritic tips varied markedly in their chromatic preference, arguing against global processing. Rather, our experimental data and results from biophysically realistic modeling support the idea that horizontal cells can process cone input locally, extending the classical view of horizontal cell function. Pharmacologically removing horizontal cells from the circuitry reduced the sensitivity of the cone signal to low frequencies, suggesting that local horizontal cell feedback shapes the temporal properties of cone output.

INTRODUCTION

Most neurons in the brain have elaborate dendritic arbors capable of more than simply integrating synaptic input. Studies

of neurons from different brain regions, such as cerebellar Purkinje cells [1], cortical pyramidal cells [2], hippocampal neurons [3], and retinal amacrine cells [4, 5], have demonstrated that dendrites can be functionally highly compartmentalized. Often, multiple dendritic units can both process synaptic input and generate synaptic output independently and at a local scale (reviewed in [6]). The cellular mechanisms supporting dendritic processing include anatomical specializations, differential distribution of active channels, and the local restriction of intracellular signaling (reviewed in [6]). Moreover, computational work suggests that dendrites can even switch between local and global signal processing [7]. Such functional compartmentalization of dendritic arbors greatly increases the computational power of single neurons and, therefore, that of the brain.

In the retina, dendritic processing has been mainly studied in ganglion cells [8, 9] and amacrine cells [4], where dendritic subunits vary dramatically in size and function. For example, starburst amacrine cell dendritic arbors are divided in sections that individually compute direction of visual motion [10, 11], while individual dendritic varicosities of A17 amacrine cells provide local reciprocal feedback to individual rod bipolar cell terminals under low-light conditions [4]. However, the outer retina also contains a candidate for dendritic processing, the horizontal cell (HC). This is a GABAergic interneuron that provides reciprocal feedback to photoreceptors and shapes their transmitter release [12–14]. The dendrites of HCs contact cone photoreceptors (cones), whereas their axon terminal system contacts rod photoreceptors (rods) [15].

Traditionally, HCs have been implicated in global processing, such as contrast enhancement and the generation of antagonistic center-surround receptive fields (reviewed in [16]). This is consistent with the fact that HCs form a gap junction-coupled network [17], which allows averaging signals across many cones. However, recent studies suggest that HCs support also a local mode of operation and that HC feedback can act at the level of a single synaptic contact between an HC dendritic tip and a cone ([14, 18]; for discussion see [19]) (Figures 1A and 1B).

Here, we test this idea by recording light stimulus-evoked signals at the HC-cone synapse in a slice preparation of the mouse retina using two-photon Ca^{2+} [20, 21] and glutamate imaging [22]. We exploited the particular retinal distribution of mouse cone types to discriminate between global and local processing: Mice express two types of cone opsins, a short (S, UV) and a medium (M, green) wavelength-sensitive opsin. So-called true S-cones [23] exclusively express S-opsin and are homogeneously



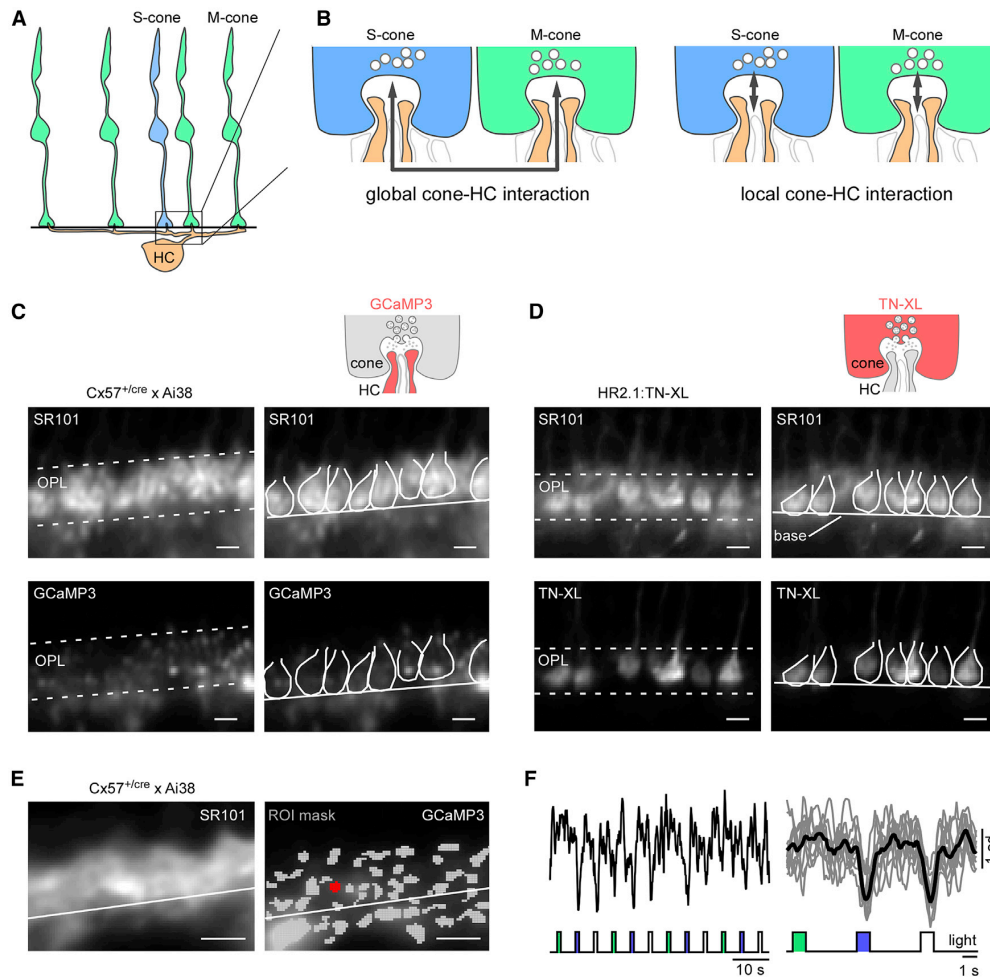


Figure 1. Identification of Cone Axon Terminals and HC Processes in Mouse Retinal Slices

(A) Schematic representation of the connectivity between S- (blue) or M-cones (green) and a horizontal cell (HC, orange). The box corresponds to the enlarged schemata shown in (B). The black line indicates the cone axon terminal base.
 (B) Neighboring S- and M-cones with postsynaptic HC dendrites. Bipolar cell dendrites are shown in white. The arrows indicate the hypothesized spread of signals in HC dendrites. Left: global (lateral) signal spread along HC dendrites. Right: local signal processing in HC dendritic tips.
 (C and D) Bath application of sulforhodamine 101 (SR101) (top images in C and D) to identify cone axon terminals in retinal slices of the *Cx57^{+/cre} × Ai38* (C) and *HR2.1:TN-XL* (D) mouse lines. Outlines of cone axon terminals were manually drawn for illustration purposes; solid lines indicate cone axon terminal base, and dotted lines indicate outer plexiform layer (OPL) borders. Upper right diagram depicts imaged synaptic compartment and the biosensor used (red).
 (E) Left: SR101 fluorescence with line marking the cone axon terminal base (analogous to A, C, and D). Right: GCaMP3-labeled HC processes are superimposed by regions of interest (ROIs; gray, exemplary ROI marked red) automatically determined (STAR Methods).
 (F) Ca^{2+} responses to green, UV, and white (GUW) 1 s light flashes of exemplary ROI (in E). The continuous Ca^{2+} trace (left) and average of $n = 10$ trials for each stimulus condition (right) are shown (Ca^{2+} signals de-trended by high-pass filtering at ~ 0.1 Hz and z-normalized; STAR Methods). Scale bars, 5 μm . See also Figure S1.

distributed across the retina, while M-cones co-express both opsins at a ratio that changes from M- to S-opsin dominant along the dorsoventral axis [24]. Thus, recording at different retinal locations with different-wavelength stimuli makes it possible to test if signals of neighboring cones mix in the postsynaptic HC dendritic process. We found that cone signals indeed remain local in the contacting HC dendritic tips, suggesting that HCs support a local mode of operation.

RESULTS

Identification of Cone Axon Terminals and HC Processes in the Mouse Retinal Slice

We recorded Ca^{2+} signals in retinal slices prepared from transgenic mice (*Cx57^{+/cre} × Ai38*; see the STAR Methods). HC processes could be identified in retinal slices by their GCaMP3 expression (Figure 1C). To identify cone axon terminals, we

bath-applied SR101 [25], which is taken up from the extracellular solution by the terminals of synaptically very active cells, such as photoreceptors, during vesicle endocytosis [26]. We confirmed that the (larger) SR101-labeled structures in the outer plexiform layer (OPL) were cone axon terminals with slices prepared from HR2.1:TN-XL mice [21], in which exclusively cones expressed TN-XL (Figure 1D).

Light-Evoked Ca^{2+} Signals in HC Processes

To record light-evoked Ca^{2+} signals in HC dendritic segments, we imaged fields in the OPL while presenting green, UV, or white light flashes (GUW protocol, STAR Methods) (Figures 1E and 1F). The resulting GCaMP3 fluorescence image series was averaged to anatomically defined regions of interest (ROIs) (STAR Methods). We only considered ROIs that responded to white flashes and fulfilled two strict quality criteria, a quality index (Q_i) and a consistency index (C_i) (Figure S1; STAR Methods), yielding 423 ROIs (4.3% from a total of 9,912 ROIs) with reliable light-evoked Ca^{2+} signals for further analysis (Figures S1B–S1D).

Because the structural layout of the cone synapse is highly stereotypical [27], we assumed that ROIs located close to the cone axon terminal base are likely to be HC dendritic tips, since this is where they make invaginating contacts with the cones (reviewed in [19]). ROIs well above the cone base are expected to belong mostly to HC axon terminal tips (contacting rods), whereas ROIs below the cone base should be located on HC primary dendrites [27]. To get an estimate of each ROI's identity, we manually determined the base of the cone terminals as a landmark (solid lines in Figures 1A and 1C–1E) in each imaged field based on SR101 labeling. We used the sharp transition between the brightly stained cone axon terminals and the dimmer SR101 labeling below, which likely represented HC dendrites [26]. We estimated the distance (d_{base}) to the cone axon terminal base for each ROI. Responsive ROIs were most frequent just above the cone axon terminal base (61.5% ROIs within $0 < d_{\text{base}} < 5 \mu\text{m}$), within the OPL band occupied by cone terminals. Here, ROIs had the highest Q_i values (Figure S1E) and the largest light-evoked Ca^{2+} signals (Figure S1F), suggesting that we could indeed measure responses from HC dendritic processes in or very close to the cone synapse.

Mechanisms Underlying Light-Evoked Ca^{2+} Responses in HCs

To confirm that the Ca^{2+} responses were mediated by glutamate release from photoreceptors, we puff-applied the AMPA/KA-type glutamate receptor antagonist 6,7-dinitroquinoline-2,3-dione (NBQX; 200 μM) while presenting white flashes (Figures 2A and 2B). NBQX significantly decreased the Ca^{2+} baseline level (F_0) in HC processes, and it virtually abolished light-evoked Ca^{2+} signals, as indicated by a significant reduction in response amplitude (ΔF) and area under the curve (F_{Area}) (Figures 2C–2E; for statistics, see Table 1).

Earlier experiments on isolated mouse HCs had shown that intracellular Ca^{2+} is modulated by influx through Ca^{2+} -permeable AMPA/KA receptors, L-type voltage-gated Ca^{2+} channels (VGCCs), and by release from internal Ca^{2+} stores [28]. To test how these pathways contributed to the Ca^{2+} signals in HC dendrites, we puff-applied a mixture of AMPA (50 μM) and KA (25 μM) before and in the presence of blockers (Figure S2). The

response amplitudes to AMPA/KA puffs alone decreased during the experiment (Figures S2A and S2C), possibly caused by downregulation of VGCCs and/or Ca^{2+} stores due to the strong pharmacological stimulus. We estimated this run-down from two consecutive puffs by calculating the ratio of the response amplitudes ($\Delta F_2/\Delta F_1$). When applying the L-type VGCC blocker verapamil (100 μM) 5 min before the second AMPA/KA puff, $\Delta F_2/\Delta F_1$ was significantly reduced compared to control (Figures S2A, S2B, and S2E; for statistics, see Table 1), confirming that VGCCs contributed to the signals.

In separate experiments, we tested if intracellular Ca^{2+} stores could be involved in amplifying Ca^{2+} signals in HC processes. We bath-applied the sarco-endoplasmic reticulum Ca^{2+} ATPase (SERCA) inhibitor thapsigargin (5 μM), which blocks Ca^{2+} store refill and leads to the depletion of Ca^{2+} stores [28], 20 min before the second AMPA/KA puff. Thapsigargin decreased $\Delta F_2/\Delta F_1$ significantly (Figures S2C, S2D, and S2F; Table 1), suggesting that release from stores contributes to Ca^{2+} signals in HC dendrites.

In summary, the observed light-evoked Ca^{2+} signals in HC processes result from a combination of Ca^{2+} sources, in agreement with earlier findings [13, 28–31]. Moreover, they are modulated by GABA auto-reception (see Figure S3 and Table S1).

Light-Evoked Ca^{2+} Signals in HCs Reflect the Dorsal-Ventral Opsin Expression Gradient

Next, we recorded HC light-evoked Ca^{2+} responses at different locations along the dorsoventral axis of the retina, using the mouse opsin expression gradient as a tool to specifically activate different combinations of S- and M-cones. While the mouse retina contains only ~5% true S-cones [23], ontogenetic M-cones in the ventral retina co-express large amounts of S-opsin and, thus, are functional S-cones [24, 32]. Therefore, if the spectral preference of the HC Ca^{2+} signals reflects this gradient, this indicates that cones (and not rods) dominantly drive these signals and that we are recording from HC dendrites.

We determined the spectral contrast (SC; STAR Methods) of each ROI as a function of its location along the dorsoventral axis (Figure 3). Consistent with the reported opsin gradient [32], we found that dorsal HC responses were dominated by M- and ventral HC responses by S-opsin activation (Figures 3A and 3B). ROIs located close to the cone axon terminal base ($-4 \leq d_{\text{base}} \leq 4 \mu\text{m}$) had significantly higher absolute SC values ($|\text{SC}_{-4\dots+4}| = 0.717 \pm 0.022$; mean \pm SEM; $n = 342$) than ROIs below ($d_{\text{base}} < -4 \mu\text{m}$, $|\text{SC}_{< -4}| = 0.417 \pm 0.045$; $n = 28$; $p = 1.611 \cdot 10^{-5}$, Wilcoxon rank-sum test) (Figure 3C). This suggests that the HC distal tips reflect the contacted cone's chromatic preference and, thus, local signals. More proximal dendrites, on the other hand, average across cones, and, thus, they show spatial integration, in agreement with the funnel shape of the d_{base} versus SC plot (Figures 3A and 3B). In the transitional zone between dorsal and ventral retina halves, both a UV- and a green-dominated ROI population co-exist (Figure 3D). Opsin immunostaining of slices from this zone confirmed that the distribution of UV and green ROIs reflects cone opsin expression (Figure 3E). ROIs in the nasal part of the slice were UV sensitive, and those in the temporal part were green sensitive, consistent with the transitional zone running at a shallow angle relative to the naso-temporal axis (Figure 3E, right scheme) [32]. Together,

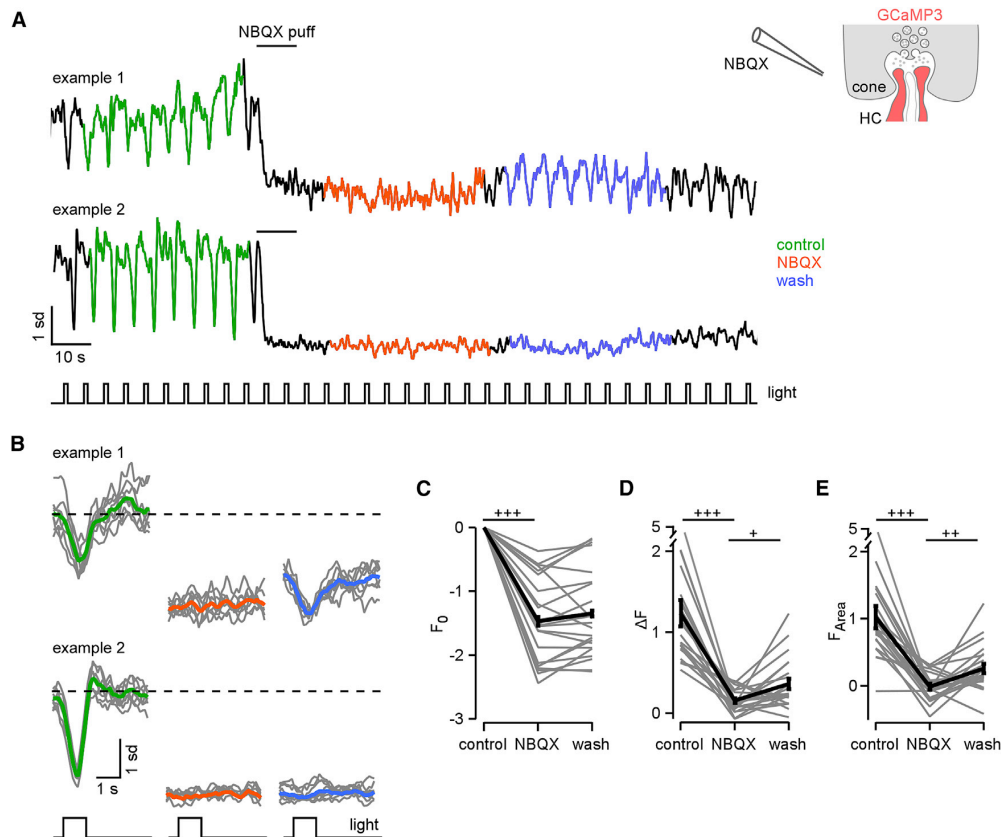


Figure 2. Light-Evoked Ca^{2+} Responses in HC Processes Are Mediated by the Activation of AMPA/Kainate-type Glutamate Receptors

(A) Exemplary Ca^{2+} responses of HC processes to white flashes before (control), after a NBQX puff, and during wash-out.

(B) Averaged responses for control (green), NBQX (orange), and wash-out (blue) (trials in gray) for the traces shown in (A).

(C–E) Quantification of NBQX effects on response baseline (F_0 , C), amplitude (ΔF , D), and area under the curve (F_{Area} , E) (average of $n = 23$ ROIs from 4 slices, 2 animals). Error bars indicate SEM; $+p \leq 0.025$, $++p \leq 0.005$, and $+++p \leq 0.0005$, Bonferroni-corrected significance threshold).

See also [Figures S2](#) and [S3](#) and [Table S1](#).

our data indicate that the activity recorded in ROIs close to the cone axon terminal base is mostly cone driven and likely reflects activity in HC dendritic tips.

Local Light-Evoked Ca^{2+} Signals in HC Dendritic Tips

Next, we assessed if signals from individual cones remain isolated within HC distal dendrites or if they spread across the cells' dendritic arbors (or the electrically coupled HC network) ([Figure 1B](#)). We looked for recording fields where neighboring ROIs had different SC preferences (i.e., contained ROIs with $SC > 0$ and ROIs with $SC < 0$). Indeed, this was the case for 15 of a total of 125 recording fields in both dorsal (5 fields; [Figure 3F](#)) and ventral retina (10 fields; [Figure 3G](#)).

To quantify this finding, we focused on purely UV and green ROIs ($|SC| > 0.3$; 7 fields, 22 ROIs), and we analyzed the distribution of the lateral distance between each UV ROI and its neighbors ([Figure 3H](#)). We found that UV ROIs clustered in close proximity ($< 10 \mu\text{m}$) of each UV ROI, suggesting that they are driven by the same cone, while the majority of green ROIs

clustered at larger distances ($> 10 \mu\text{m}$). The distribution of green ROIs appeared to be periodic with the average distance approximating that between cone axon terminals ($\sim 8 \mu\text{m}$, cf. [Figures 1C](#) and [1D](#)), indicating that these (green) ROIs were likely driven by other cones.

HC Dendritic Processes Inherit Properties of the Presynaptic Cone

If HC dendritic tips reflect the local cone output, the measured signals are expected to share properties with the cone signals (see also [Figure S4](#)). To test this, we presented a colored noise stimulus (see the [STAR Methods](#)), and we measured correlations between neighboring cone axon terminals and between neighboring HC dendritic tips in the dorsal retina ([Figure 4](#)). If HCs integrated signals globally, e.g., by averaging across an HC's dendritic arbor or by electrical HC coupling, we would expect a higher correlation between HC dendritic tips for the two stimulus classes, due to the lateral signal spread, than for cone axon terminals. The cone recordings were performed in HR2.1:TN-XL

Table 1. Pharmacology for AMPA/KA-type Glutamate Receptors, Voltage-Gated Ca²⁺ Channels, and Ca²⁺ Release from Stores

Pharmacology for AMPA/KA-type Glutamate Receptors				
	Number of Mice/ Slices/ROIs	Control	NBQX	Wash
F_0 (SD)	2/4/23	0	-1.470 ± 0.069 ($p = 2.384 \cdot 10^{-7}$)	-1.348 ± 0.046 ($p = 0.033$)
ΔF (SD)		1.235 ± 0.163	0.156 ± 0.029 ($p = 2.384 \cdot 10^{-7}$)	0.362 ± 0.064 ($p = 0.007$)
F_{Area} (a.u.)		1.024 ± 0.167	-0.012 ± 0.044 ($p = 4.768 \cdot 10^{-7}$)	0.257 ± 0.071 ($p = 0.003$)
Pharmacology for Voltage-Gated Ca ²⁺ Channels and Ca ²⁺ Release from Stores				
	Number of Mice/ Slices/ROIs	AMPA/KA Puff 1 ΔF_1 [SD]	AMPA/KA Puff 2 ΔF_2 [SD] (ΔF_2 versus ΔF_1)	$\Delta F_2/\Delta F_1$ Median [MAD] (versus Control)
Control (5')	2/2/23	3.106 ± 0.286	1.648 ± 0.198 ($p = 1.025 \cdot 10^{-5}$)	0.439 ± 0.137
Verapamil (5')	2/3/18	2.011 ± 0.177	0.426 ± 0.130 ($p = 7.629 \cdot 10^{-5}$)	0.127 ± 145 ($p = 9.088 \cdot 10^{-5}$)
Control (20')	2/3/28	2.842 ± 0.209	2.293 ± 0.167 ($p = 0.014$)	0.855 ± 0.284
Thapsigargin (20')	2/4/14	2.297 ± 0.387	0.814 ± 0.256 ($p = 3.662 \cdot 10^{-4}$)	0.499 ± 0.140 ($p = 9.163 \cdot 10^{-4}$)

NBQX, AMPA/KA-type glutamate receptor antagonist; Ca²⁺ baseline (F_0), amplitude (ΔF), and area under the curve (F_{Area}) of light-evoked Ca²⁺ responses; verapamil, L-type VGCC blocker; thapsigargin, inhibitor of sarco-endoplasmic reticulum Ca²⁺-ATPases; amplitude puff 1 (ΔF_1), amplitude puff 2 (ΔF_2), ratio puff 2/puff 1 ($\Delta F_2/\Delta F_1$); MAD, median absolute deviation; SD, standard deviation. Wilcoxon signed-rank test and Wilcoxon rank-sum test ($\Delta F_2/\Delta F_1$).

mice [21] in which cones expressed the Ca²⁺ biosensor TN-XL (cf. Figure 1D).

We calculated the linear correlation coefficient (ρ) between Ca²⁺ traces from cone ROIs (Figures 4A–4C) in the same recording field, in response to colored noise and to the GUV stimulus. Because the noise is a weaker stimulus compared to the GUV flashes, the correlation between cone terminal responses significantly decreased for the noise (Table S2), both when only considering negative transients (Figure 4G) and when comparing whole traces (Figure 4H). We repeated this experiment on HCs in Cx57^{+/cre} × Ai38 mice (Figures 4D–4F), and, indeed, like for the cones, the correlation between HC responses decreased for colored noise compared to GUV stimulation (Table S2), for negative transients (Figure 4G) and whole traces (Figure 4H).

A direct comparison between the two sets of experiments is complicated by several factors that influence the estimation of response correlation, including different scan rates for GUV versus noise stimuli, different biosensors in cones versus HCs, and different ROI sizes. Nevertheless, our finding that noise stimulation results in a similar (relative) decrease in correlation for both the pre- (cone) and the postsynaptic (HC) signal (see Δ median in Table S2) argues in favor of relatively independent signals and possibly local processing in HC distal dendrites. This is further supported by the finding that nearby HC dendrites possibly receiving input from the same cone show a higher degree of correlation (correlation between negative events versus distance for noise: Spearman $R = -0.271$, $p = 2.28 \cdot 10^{-20}$, Spearman rank correlation test; $n = 1,125$; Figure S5).

We also used the Ca²⁺ responses to the noise stimulus to estimate the temporal receptive field (time kernels, STAR Methods; [33]). In cone axon terminals (Figure 4I) and HC dendritic tips (Figure 4J), the time kernels computed using negative Ca²⁺ transients (cf. Figures 4C and 4F) displayed robust positive deflections. Grouping cone ROIs by their spectral preference (derived from their time kernels; STAR Methods) into green, UV, and mixed revealed a fraction of ~4% UV ROIs (Figure 4I), closely matching the fraction of S-cones in the dorsal mouse retina [23]. The averaged time kernels of the different groups

looked similar for cones and HCs (Figures 4I and 4J); cone kernels appeared to be slightly faster, likely due to differences in biosensor properties (TN-XL: $\tau_{decay} = 0.2$ s, K_D *in vitro* = 2.2 μ M, from [34]; GCaMP3: $\tau_{decay} = 0.23$ s, K_D *in vitro* = 0.66 μ M, from [20, 35]). HC kernels were noisier than those of cones. This may be related to differences in ROI area (cones: 9.6 ± 0.2 μ m², $n = 457$ ROIs; HCs: 1.9 ± 0.1 μ m², $n = 344$ ROIs) and, thus, different spatial averaging. The fact that we observed UV-selective kernels in HC dendritic tips just as in cones adds further evidence to the notion that HC dendritic tips show highly local Ca²⁺ signals (cf. Figure 3).

HC Morphology Supports Electrical Isolation of Distal HC Dendrites

To test if the HC morphology supports electrically isolating at its dendritic tips, we built a simple, biophysically realistic model of a dendritic branch, including synapses with cones based on a volume reconstruction from electron microscopy (EM) data (Figure 5; see the STAR Methods for details). First, we stimulated a single HC dendritic tip by injecting a current at the position of its synaptic cone contact such that the tip depolarized to -25 mV. We measured the resulting voltage and Ca²⁺ levels in all other cone-contacting tips, and we found the membrane voltage dropping rapidly with distance from the stimulated tip (Figure 5B). Only in directly neighboring tips (≤ 15 μ m distance), the depolarization was sufficient to activate VGCCs; however, even then the resulting Ca²⁺ increase was two orders of magnitude smaller compared to the stimulated tip (Figure 5C). We also traced the voltage change from a stimulated tip to the soma (Figures 5D and 5E), showing that the tips were well isolated from the rest of the HC's dendritic arbor. Finally, we tested if our model could reproduce the light-evoked Ca²⁺ signals: We connected a representative mixture of S- and M-cones to the HC, and we presented full-field light flashes (Figure 5F). The simulated voltage responses resembled the Ca²⁺ signals we observed in distal HC dendrites in terms of time course and spectral preference diversity (e.g., Figure 3F). Therefore, these modeling data are in line with our experimental data, indicating that the HC

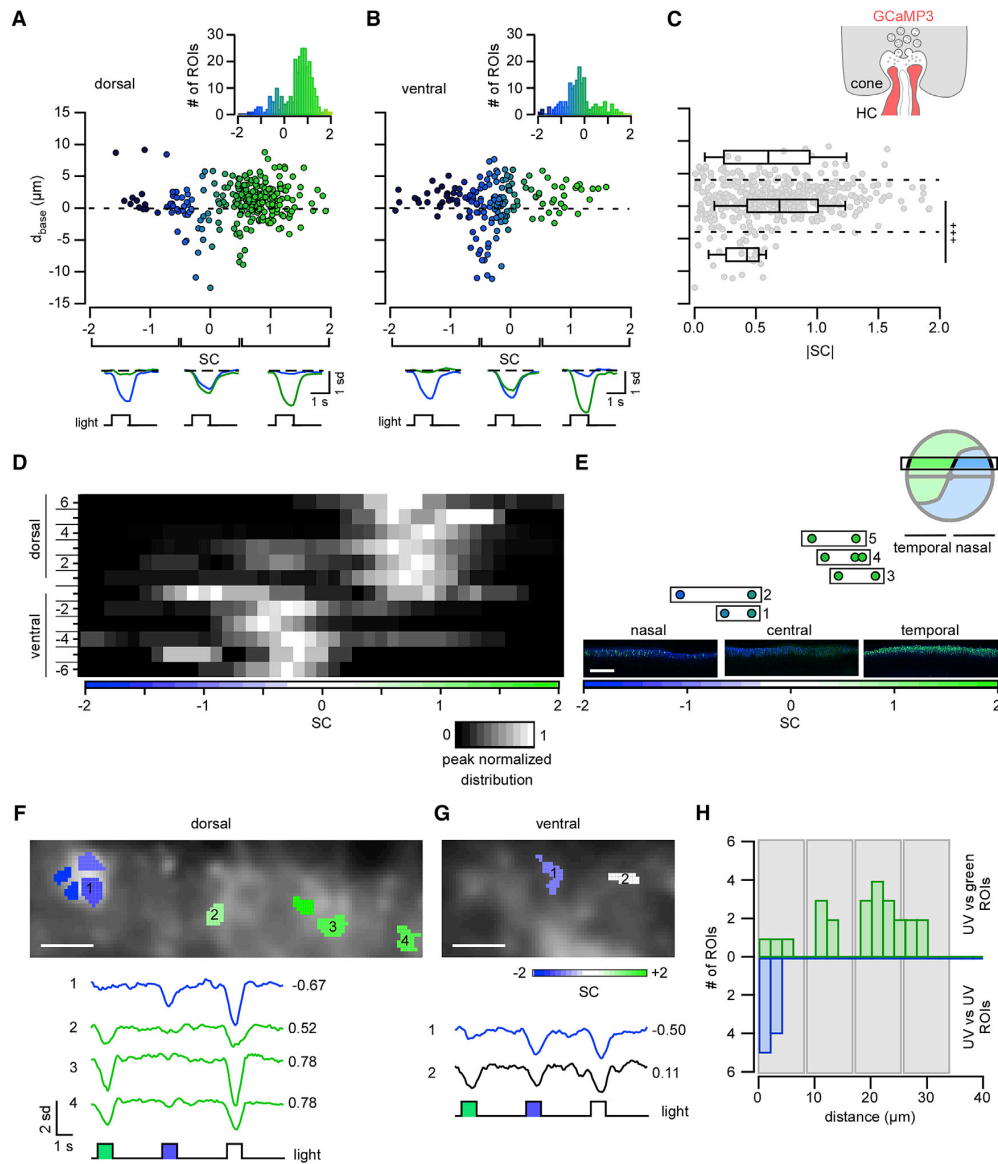


Figure 3. Light-Evoked Ca^{2+} Signals in HC Dendrites Reflect the Dorsoventral Cone Opsin Expression Gradient and Local Cone Input
 (A and B) Plots showing distance between ROI and cone axon terminal base (d_{base}) as a function of spectral contrast (SC; STAR Methods) for dorsal ($n = 262$ ROIs) (A) and ventral retina ($n = 161$) (B). Insets: histograms of SC distributions are shown. Below: averaged Ca^{2+} signals in response to green and UV flashes for different SC intervals are shown (averages of $n = 10$ trials).
 (C) ROI distance to cone axon terminal base (d_{base}) as a function of $|\text{SC}|$ (ROIs from dorsal and ventral retina). ROIs were separated into three groups (dashed lines) depending on d_{base} : above ($d_{\text{base}} > 4 \mu\text{m}$), below ($d_{\text{base}} < -4 \mu\text{m}$), and near the cone axon terminal base ($-4 \leq d_{\text{base}} \leq 4 \mu\text{m}$).
 (D) SC distribution sorted by retinal slice position (dorsal to ventral; distributions peak normalized for each slice position).
 (E) SC of ROIs from 5 locations on the same slice (boxes 1–5) along the naso-temporal axis (position +3, see D) and corresponding S- (blue) and M-opsin (green) immunolabeling in the temporal, central, and nasal regions.
 (F and G) Examples of recording fields containing ROIs with different SC for dorsal (F) and ventral (G) retina; respective Ca^{2+} signals below (averages of $n = 10$ trials). Colors reflect SC preference of each ROI (color bar in G).
 (H) Spatial distribution of UV- (bottom) and green- (top) preferring ROIs relative to each UV ROI (at $0 \mu\text{m}$) (for ROIs with $|\text{SC}| > 0.3$; $n = 22$ ROIs from 7 fields, 4 dorsal and 3 ventral retinas). Gray boxes illustrate expected location of neighboring cone axon terminals ($+++p \leq 0.0005$, Bonferroni-corrected significance threshold). Scale bars, $200 \mu\text{m}$ (E) and $5 \mu\text{m}$ (F and G).

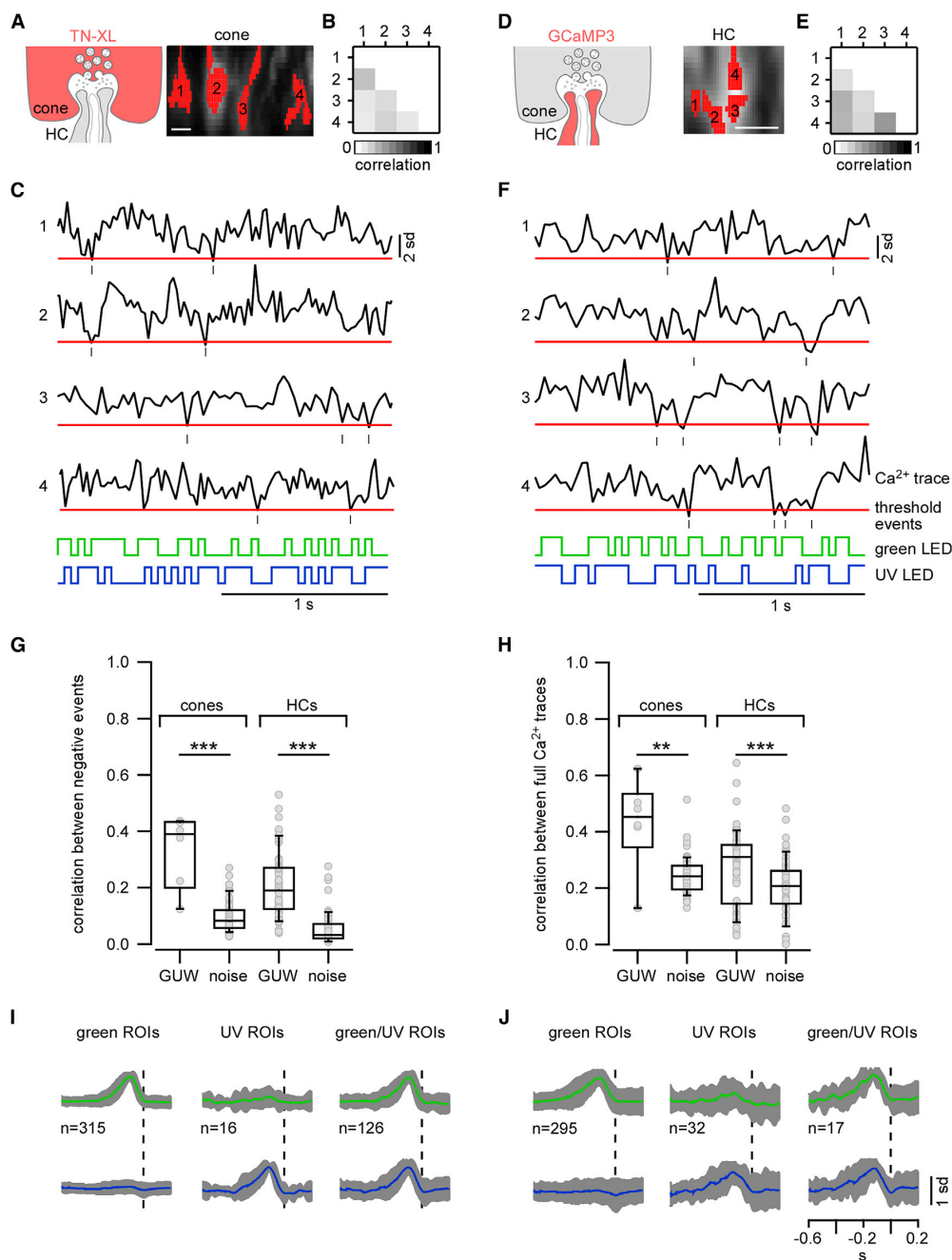


Figure 4. In the Dorsal Retina, Light-Evoked Ca²⁺ Signals in Neighboring Cone Axon Terminals and Neighboring HC Dendrites Show Similar Degrees of Decorrelation

(A–F) Exemplary neighboring cone axon terminals in the HR2.1:TN-XL retina (A) and HC dendritic processes in the Cx57^{+cre} × Ai38 retina (D) with respective Ca²⁺ signals (C and F) in response to 25-Hz colored noise (STAR Methods), with threshold (red line) used to detect negative events. Correlation of events for exemplary cones and HCs are shown in (B) and (E).

(legend continued on next page)

dendritic morphology supports electrical isolation of distal tips and, thereby, local signaling.

Local HC Feedback May Shape Temporal Properties of Cone Responses

Finally, we assessed the effect of local HC feedback on the cone response. We presented a 60-Hz full-field binary noise stimulus to slices prepared from HR2.1:TN-XL mice (Figures 6A and 6C) and iGluSnFR-transduced C57BL/6J mice (Figures 6B and 6D) (STAR Methods; [37]). We estimated time kernels of Ca^{2+} signals in cones and glutamate signals in the OPL as described above (cf. Figure 4). The averaged time kernels were more transient for iGluSnFR in comparison to those for Ca^{2+} (Figure 6E), likely reflecting differences in signal (Ca^{2+} versus glutamate) and biosensor kinetics ($\tau_{\text{decay}} \approx 200$ ms for TN-XL versus 92 ms for iGluSnFR; [22]). For further analysis, we computed the periodograms of the time kernels using discrete Fourier transforms [14], and we examined the difference in their power spectral density for each frequency component (STAR Methods; Figure 6F). We first performed two consecutive recordings with an interval of 5 min as controls. No significant differences were found between controls for time kernels from both cone Ca^{2+} ($n = 61$ ROIs, 11 slices, 3 mice) and glutamate release ($n = 76/15/3$). Next, we deprived HCs from their input by bath application of NBQX, and we assessed the effect on the time kernels and their corresponding periodograms for cone Ca^{2+} ($n = 48/15/3$) and glutamate release ($n = 47/18/3$). Although the time kernels looked narrower after NBQX application, no significant differences were found between these kernels with respect to time to peak and F_{Area} . However, the analysis of the periodograms revealed a significant reduction of the power spectral density at low frequencies (cone Ca^{2+} , at 1 Hz, $p = 3 \cdot 10^{-4}$, dependent samples t test; glutamate release, at 0 Hz, $p = 3.2 \cdot 10^{-7}$, at 1 Hz, $p = 4.7 \cdot 10^{-5}$), indicating that local HC feedback contributes to temporal shaping of cone output by increasing the sensitivity of the cone signal to low-frequency signal components.

DISCUSSION

HCs are traditionally thought to play a role in global processing and to provide lateral inhibition, e.g., for contrast enhancement (reviewed in [19]). Recent studies, however, suggest the existence of a local processing mode, in which HCs provide locally tailored feedback to individual cones [14, 18], reminiscent of the local dendritic processing in amacrine cells (e.g., [4]).

Here we recorded light stimulus-evoked pre- and postsynaptic activity at the cone-HC synapse in the mouse retina, and we present three lines of evidence supporting that mouse HCs can process cone input in a highly local and independent manner. First, neighboring dendritic tips, which presumably contact neighboring cones, differed in their chromatic preferences. While the ubiquitous GCaMP3 expression in HCs did not allow

us to assign ROIs to individual HCs, it is unlikely that our data are solely explained by recording two overlapping kinds of HCs with opposite spectral preference, simply because mice feature only one type of HC, which indiscriminately contacts all cones within its dendritic field [29, 38]. Second, the correlation levels of Ca^{2+} signals measured in neighboring HC dendritic tips were similar to those recorded in neighboring cone axon terminals. If cone inputs were already averaged at the level of the distal HC dendrite, we would have expected an increase in correlation from cones to HCs. Hence, our correlation data support local signaling (and possibly processing) in HC dendritic tips. Third, a simple, biophysically realistic model confirms that the HC morphology supports electrical isolation between dendritic tips.

By isolating HCs pharmacologically from their cone input, we showed that the HC feedback may shape the temporal filtering properties of the cone synapse, i.e., by modulating the power at low-stimulus frequencies. Taken together, our study extends the traditional view of global HC signaling by a powerful local component, indicating that dendritic processing already happens at the first synapse of the retina.

Local versus Global HC Feedback

Byzov and Shura-Bura [39] were first to suggest that HCs provide local feedback to cones. Following experimental confirmation, it was then proposed that both local and global feedback are triggered by the activation of AMPA/KA receptors on HCs [18], but with local feedback being mediated by the local Ca^{2+} in the dendritic tip and global feedback relying on depolarization and possibly amplification by VGCCs [40]. While we did not find interactions between distal HC dendrites, the mixing of S- and M-signals we observed in proximal HC dendrites hints at some degree of global signal integration. We cannot exclude the possibility that the slice preparation introduces a bias toward local signaling; however, earlier work in rabbit HCs suggests that local feedback suffers more from slicing than global feedback [18]. Furthermore, more global-scale interactions have been successfully demonstrated in mouse retinal slices; these include, for instance, lateral inhibition between cones [12] and electrical coupling within the All amacrine cell network [41]. Global signal integration within the HC network requires Cx57-mediated gap-junction coupling [17]. In the $\text{Cx57}^{+/cre} \times \text{Ai38}$ mice used here, one Cx57 allele is replaced by a *cre* gene, resulting in a reduced Cx57 expression. The HCs in these mice feature smaller receptive fields (RFs) and elevated resting potentials; but, since HC coupling is intact and cone-HC synapses seem unaltered [42], we do not expect this genetic modification to substantially affect our conclusions.

Mechanism(s) of Local Ca^{2+} Signaling in HC Dendrites

What is the cellular basis of the local Ca^{2+} signaling we observed in HC dendrites? In line with previous studies [28, 29, 31], we show that these signals are mediated by a combination of

(G and H) Average correlation per field for events only (G) and full Ca^{2+} traces (H) for cones and HCs in response to green, UV, and white (GUW) light (cones, $n = 6$ fields; HCs, $n = 60$ fields) and to colored noise (cones, $n = 65$ fields; HCs, $n = 57$ fields).

(I and J) Normalized time kernels of green ROIs (amplitude green kernel > 2 SD noise, left), UV ROIs (amplitude UV kernel > 2 SD noise, middle), and mixed ROIs (amplitude green and UV kernel > 2 SD noise, right) for cones (I) and HCs (J) (with 2 SD in gray). ** $p \leq 0.01$ and *** $p \leq 0.001$. Scale bars, 5 μm .

See also Figures S4 and S5 and Table S2.

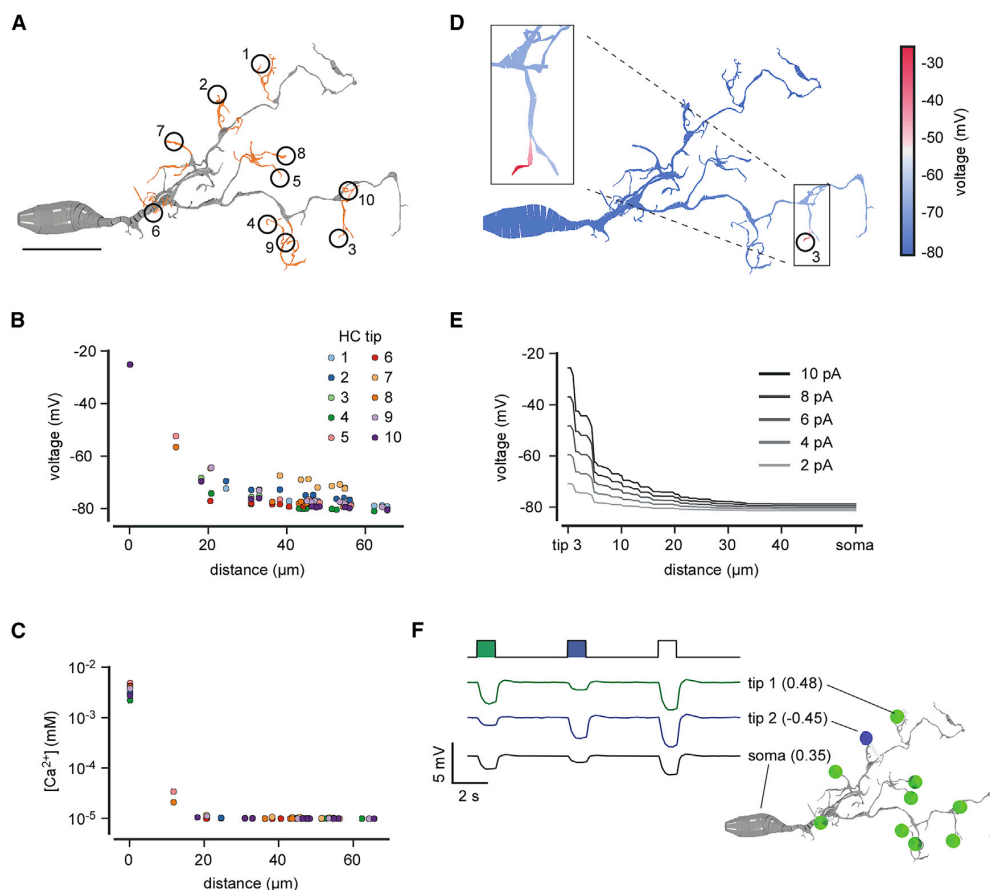


Figure 5. Dendritic Morphology of HCs Supports Electrical Isolation of Dendritic Tips

(A) Reconstruction of an HC dendrite. Distal tips (orange) that invaginate cone axon terminals are numbered (1–10). Dataset from [36].

(B and C) Voltage (B) and resulting Ca^{2+} level (C) measured in all cone-contacting HC tips as a function of distance from the current-injected tip.

(D) Voltage distribution across the branch after current injection into HC tip 3.

(E) Voltage drop along the dendrite between injected tip (from D) and soma.

(F) Simulated voltage responses to green/UV/white light flashes measured in two HC tips (1 and 2, contacting a green and a UV cone, respectively) and the soma. Inset: branch with connected cones (colored by spectral preference, which is also given in brackets) is shown.

Scale bar in (A), 10 μm .

Ca^{2+} -permeable AMPA/KA-type glutamate receptors, VGCCs, and Ca^{2+} released from stores. This combination is reminiscent of another reciprocal synapse with local signaling, the synapse between rod bipolar cells (RBCs) and A17 amacrine cells [43]. Here, Ca^{2+} enters a dendritic amacrine cell (AC) varicosity via AMPA receptors and triggers GABA release, with the necessary amplification of the Ca^{2+} signal generated by Ca^{2+} -induced Ca^{2+} release from stores. To keep the signal from spreading to neighboring varicosities, A17 cells express Ca^{2+} -activated potassium (BK) channels that hyperpolarize the varicosity and suppress the activation of VGCCs. In addition, varicosities are spaced with an average distance of $\sim 20 \mu\text{m}$ along the dendrite to increase electrical isolation.

Local signaling in HCs may employ a similar mechanism. (1) As shown for several species, local HC feedback can be trig-

gered by AMPA receptor activation without requiring VGCCs [18]. If this is also true for mouse HCs is still unclear. The Ca^{2+} signals evoked by AMPA/KA puffs mainly involved L-type VGCCs and Ca^{2+} stores; but, for weaker, more physiological stimuli (i.e., light), the direct contribution of AMPA/KA receptors to the Ca^{2+} signals may be greater, as it seems to be the case in A17 cells [43]. Moreover, activity of VGCCs in HCs is suppressed by dopamine, which is released in a light-dependent fashion [44], suggesting that VGCCs contribute less to the Ca^{2+} signal under our light conditions. (2) HCs express BK channels that limit membrane depolarization in a voltage- and Ca^{2+} -dependent manner [45]. (3) Ca^{2+} signals in HC dendrites partially rely on Ca^{2+} stores [28]. (4) The HC morphology enhances electrical isolation between dendritic tips, as supported by our modeling data.

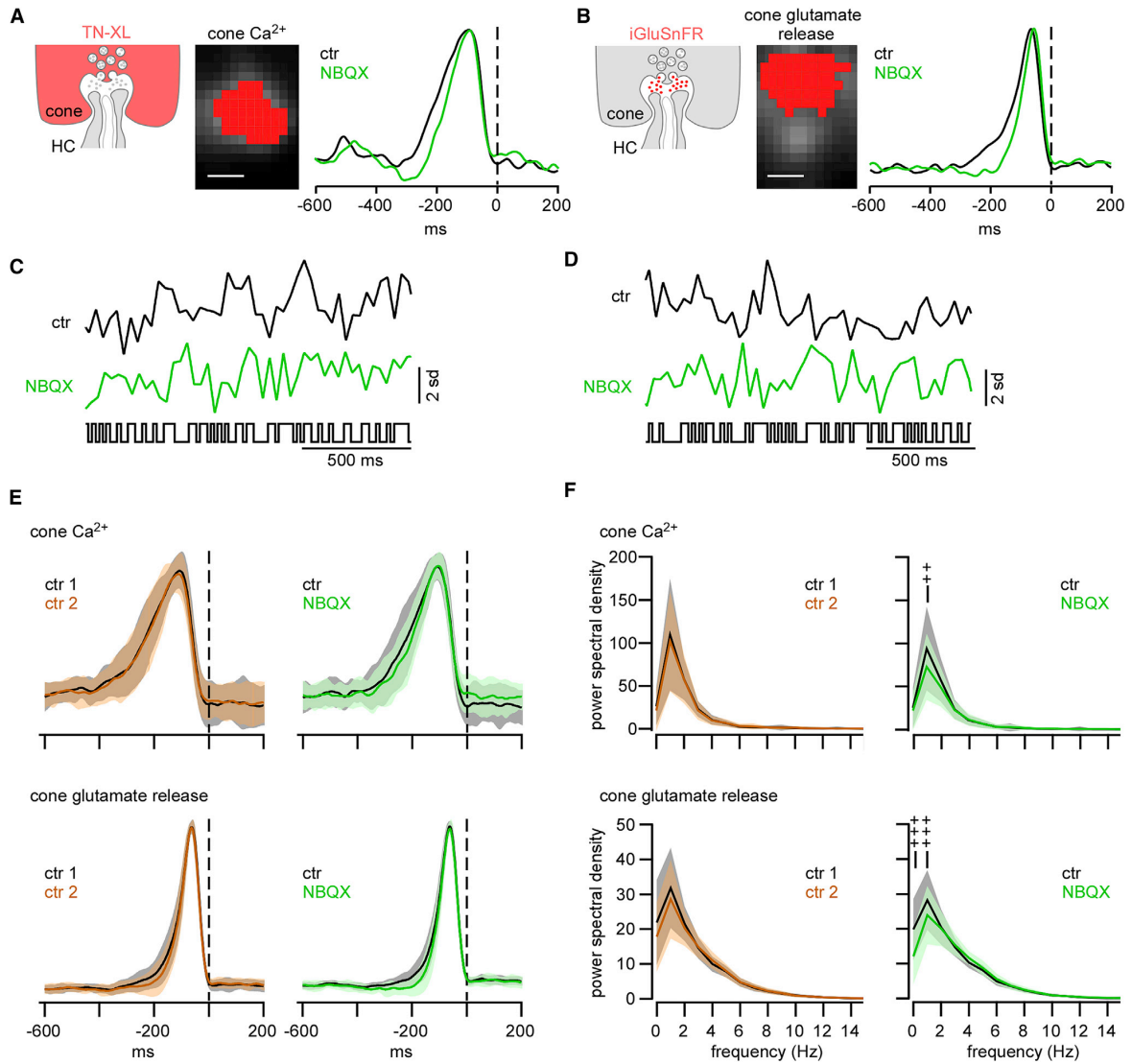


Figure 6. Local HC Feedback Modulates Temporal Properties of Cone Response

(A–D) Exemplary ROIs of cone axon terminals, defined by TN-XL expression (A) or by iGluSnFR activity (B; STAR Methods), with respective temporal receptive field kernels calculated from response to a full-field 60-Hz binary noise stimulus (raw traces in C and D; STAR Methods) for control condition (black traces in A–D) and during bath application of NBQX (green traces in A–D).

(E) Normalized time kernels for cone Ca^{2+} (upper panel) and glutamate release (lower panel) for control condition (ctr1, ctr2; left) and with NBQX (right) (cone Ca^{2+} : ctr, n = 61 ROIs; NBQX, n = 48 ROIs; cone glutamate release: ctr, n = 76 ROIs; NBQX, n = 47 ROIs; shaded areas indicate 1 SD).

(F) Periodograms (STAR Methods) generated from cone kernels (E) using a discrete Fourier transform: cone Ca^{2+} (upper panel) and glutamate release (lower panel) for control condition (left) and with NBQX (right) (shaded areas indicate 1 SD) (++) $\leq 6.66 \cdot 10^{-4}$ and (+++) $\leq 6.66 \cdot 10^{-5}$, Bonferroni-corrected significance threshold). Scale bars, 2.5 μ m.

Do Rods Contribute to the Ca^{2+} Signals in HC Dendrites?

The transgenic mouse expresses GCaMP3 in all HC compartments, and because dendritic and axonal HC processes are intermingled, we could not distinguish them solely based on their morphological appearance. Yet, our conclusions rely on the assumption that the measured Ca^{2+} signals reflect cone input

and that rod input (either mediated by direct rod-HC contacts or by rod-cone coupling) can be neglected. We think that this was the case for three reasons. (1) We measured the largest Ca^{2+} signals at the OPL level where HC dendrites invaginate the cone axon terminal base [19, 27]. (2) The chromatic tuning of these Ca^{2+} signals reflected the local ratio of S- versus

M-opsin expression along the retina's dorsoventral axis. If rods had substantially responded to either UV or green, we would have expected an additional UV response in dorsal HCs and/or an additional green response in ventral HCs. (3) Laser-evoked photoreceptor excitation alone generated a background illumination equivalent to $\sim 10^4$ P \cdot s $^{-1}$ /cone (STAR Methods; [32]), which is probably similar in rods [25]. Electrical recordings from mouse rods in slices indicate that rod photoresponses disappear at $\sim 10^4$ P \cdot s $^{-1}$ /rod [46], suggesting that rods were not operational under our stimulation conditions. Our earlier finding that RBCs respond to light-on stimuli under similar conditions [37] may be explained by direct (or indirect) cone input to RBCs, as in mice $\sim 70\%$ of the RBCs contact at least one cone [47], and cones and rods are at least weakly coupled at our light levels [48].

Functional Consequences of Local Dendritic Processing for HC Feedback to Cones

What could be the purpose of local HC feedback to cones? Our pharmacological data indicate that (local) HC feedback boosts low-frequency signals in the cone output, consistent with a general role of HC feedback in dynamically shaping/adapting the time course of cone transmission, e.g., as a function of stimulus configuration (e.g., center versus surround stimulation; [49, 50]). Specifically, our finding is consistent with earlier work showing that activation of HCs (by a dark annular stimulus) shifts the frequency sensitivity of an HC in the stimulus center toward lower frequencies [51]. That we could not also find a shift at higher frequencies may well be due to temporal limitations both of the imaging system and the biosensors (cf. Results).

In theory, the objective of sensory neurons is often considered to be the relative enhancement of relevant information content from a sensory input, given a limited metabolic capacity [52]. Adaptational mechanisms allow the circuitry to robustly meet this objective despite changing natural scene statistics [53], whether by enhancing features (increasing information content) or removing redundancy (reducing metabolic cost). For HCs, these elements have typically been considered for adaptation to spatial properties, through mechanisms such as the center-surround RF and background luminance subtraction. Here, the local adaptation we observed appears to operate in the time domain; the effect is made visible by changes in sensitivity to (at least but probably not solely) low-frequency components, which might convey little information content in natural scenes where they are strongly present and more information otherwise. In this sense, local feedback may serve temporal contrast enhancement. That the feedback can occur at the level of individual photoreceptors is perhaps not surprising, as such a cell driven in isolation is still subject to trade-offs in information and metabolic cost. In natural scenes, spatial and temporal statistics are not independent, and the interplay between their respective adaptational mechanisms, such as here the potential interplay between local and global feedback mechanisms in HCs, is an attractive subject for further study (see discussion in [19]). A promising approach to tackle these questions may be a combination of voltage biosensors [54] to probe the voltage distribution across an HC's dendritic arbor with biophysically realistic models.

STAR★METHODS

Detailed methods are provided in the online version of this paper and include the following:

- KEY RESOURCES TABLE
- CONTACT FOR REAGENT AND RESOURCE SHARING
- EXPERIMENTAL MODEL AND SUBJECT DETAILS
 - Animals
- METHOD DETAILS
 - Retinal tissue preparation
 - Virus injection
 - Two-photon imaging
 - Light stimulation
 - Immunohistochemistry
 - Pharmacology and drug application
 - Data analysis
- QUANTIFICATION AND STATISTICAL ANALYSIS
- DATA AND SOFTWARE AVAILABILITY

SUPPLEMENTAL INFORMATION

Supplemental Information includes five figures and two tables and can be found with this article online at <https://doi.org/10.1016/j.cub.2017.10.050>.

AUTHOR CONTRIBUTIONS

C.A.C., T.S., and T.E. designed the study. C.A.C. and S.P. established the experimental approach. C.A.C. performed experiments and pre-processing. C.A.C. analyzed the data with input from T.S., T.B., L.E.R., P.B., and T.E. C.B. generated and analyzed the model with input from T.S., P.B., and T.E. C.A.C., T.S., T.E., and L.E.R. wrote the manuscript with input from P.B., C.B., and T.B.

ACKNOWLEDGMENTS

This work was supported by the Deutsche Forschungsgemeinschaft (EXC 307, CIN to T.E. and T.S., SCHU 2243/3-1 to T.S., and BE5601/1-1 to P.B.) and the German Ministry of Science and Education (BMBF) through the Bernstein Award to P.B. (FKZ: 01GQ1601). We thank G. Eske for excellent technical assistance and K. Franke for performing the intravitreal virus injection, Y. Zhang for tracing the HC dendrite, and R.G. Smith for help in setting up the NeuronC model. We thank L.L. Looger, the Janelia Research Campus of the Howard Hughes Medical Institute, and the Genetically Encoded Neuronal Indicator and Effector (GENIE) Project for making the viral construct AAV9.hSyn.iGluSnFR.WPRE.SV40 publicly available.

Received: June 12, 2017

Revised: September 1, 2017

Accepted: October 19, 2017

Published: November 22, 2017

REFERENCES

1. Denk, W., Sugimori, M., and Llinás, R. (1995). Two types of calcium response limited to single spines in cerebellar Purkinje cells. *Proc. Natl. Acad. Sci. USA* 92, 8279–8282.
2. Branco, T., Clark, B.A., and Häusser, M. (2010). Dendritic discrimination of temporal input sequences in cortical neurons. *Science* 329, 1671–1675.
3. Branco, T., Staras, K., Darcy, K.J., and Goda, Y. (2008). Local dendritic activity sets release probability at hippocampal synapses. *Neuron* 59, 475–485.

4. Grimes, W.N., Zhang, J., Graydon, C.W., Kachar, B., and Diamond, J.S. (2010). Retinal parallel processors: more than 100 independent microcircuits operate within a single interneuron. *Neuron* 65, 873–885.
5. Euler, T., Detwiler, P.B., and Denk, W. (2002). Directionally selective calcium signals in dendrites of starburst amacrine cells. *Nature* 418, 845–852.
6. Branco, T., and Häusser, M. (2010). The single dendritic branch as a fundamental functional unit in the nervous system. *Curr. Opin. Neurobiol.* 20, 494–502.
7. Remme, M.W.H., and Rinzal, J. (2011). Role of active dendritic conductances in subthreshold input integration. *J. Comput. Neurosci.* 31, 13–30.
8. Schachter, M.J., Oesch, N., Smith, R.G., and Taylor, W.R. (2010). Dendritic spikes amplify the synaptic signal to enhance detection of motion in a simulation of the direction-selective ganglion cell. *PLoS Comput. Biol.* 6, 1–24.
9. Oesch, N., Euler, T., and Taylor, W.R. (2005). Direction-selective dendritic action potentials in rabbit retina. *Neuron* 47, 739–750.
10. Hausselt, S.E., Euler, T., Detwiler, P.B., and Denk, W. (2007). A dendrite-autonomous mechanism for direction selectivity in retinal starburst amacrine cells. *PLoS Biol.* 5, e185.
11. Ding, H., Smith, R.G., Poleg-Polsky, A., Diamond, J.S., and Briggman, K.L. (2016). Species-specific wiring for direction selectivity in the mammalian retina. *Nature* 535, 105–110.
12. Kemmler, R., Schultz, K., Dedek, K., Euler, T., and Schubert, T. (2014). Differential regulation of cone calcium signals by different horizontal cell feedback mechanisms in the mouse retina. *J. Neurosci.* 34, 11826–11843.
13. Liu, X., Hirano, A.A., Sun, X., Brecha, N.C., and Barnes, S. (2013). Calcium channels in rat horizontal cells regulate feedback inhibition of photoreceptors through an unconventional GABA- and pH-sensitive mechanism. *J. Physiol.* 591, 3309–3324.
14. Vroman, R., Klaassen, L.J., Howlett, M.H.C., Cenedese, V., Klooster, J., Sjoerdsma, T., and Kamermans, M. (2014). Extracellular ATP hydrolysis inhibits synaptic transmission by increasing pH buffering in the synaptic cleft. *PLoS Biol.* 12, e1001864.
15. Peichl, L., and González-Soriano, J. (1994). Morphological types of horizontal cell in rodent retinae: a comparison of rat, mouse, gerbil, and guinea pig. *Vis. Neurosci.* 11, 501–517.
16. Thoreson, W.B., and Mangel, S.C. (2012). Lateral interactions in the outer retina. *Prog. Retin. Eye Res.* 31, 407–441.
17. Hombach, S., Janssen-Bienhold, U., Söhl, G., Schubert, T., Büssow, H., Ott, T., Weiler, R., and Willecke, K. (2004). Functional expression of connexin57 in horizontal cells of the mouse retina. *Eur. J. Neurosci.* 19, 2633–2640.
18. Jackman, S.L., Babai, N., Chambers, J.J., Thoreson, W.B., and Kramer, R.H. (2011). A positive feedback synapse from retinal horizontal cells to cone photoreceptors. *PLoS Biol.* 9, e1001057.
19. Chapot, C.A., Euler, T., and Schubert, T. (2017). How do horizontal cells ‘talk’ to cone photoreceptors? Different levels of complexity at the cone-horizontal cell synapse. *J. Physiol.* 595, 5495–5506.
20. Zariwala, H.A., Borghuis, B.G., Hoogland, T.M., Madisen, L., Tian, L., De Zeeuw, C.I., Zeng, H., Looger, L.L., Svoboda, K., and Chen, T.-W. (2012). A Cre-dependent GCaMP3 reporter mouse for neuronal imaging in vivo. *J. Neurosci.* 32, 3131–3141.
21. Wei, T., Schubert, T., Paquet-Durand, F., Tanimoto, N., Chang, L., Koepfen, K., Ott, T., Griesbeck, O., Seeliger, M.W., Euler, T., and Wissinger, B. (2012). Light-driven calcium signals in mouse cone photoreceptors. *J. Neurosci.* 32, 6981–6994.
22. Marvin, J.S., Borghuis, B.G., Tian, L., Cichon, J., Harnett, M.T., Akerboom, J., Gordus, A., Renninger, S.L., Chen, T.-W., Bargmann, C.I., et al. (2013). An optimized fluorescent probe for visualizing glutamate neurotransmission. *Nat. Methods* 10, 162–170.
23. Haverkamp, S., Wässle, H., Duebel, J., Kuner, T., Augustine, G.J., Feng, G., and Euler, T. (2005). The primordial, blue-cone color system of the mouse retina. *J. Neurosci.* 25, 5438–5445.
24. Szél, A., Röhlich, P., Caffé, A.R., Juliusson, B., Aguirre, G., and Van Veen, T. (1992). Unique topographic separation of two spectral classes of cones in the mouse retina. *J. Comp. Neurol.* 325, 327–342.
25. Euler, T., Hausselt, S.E., Margolis, D.J., Breuninger, T., Castell, X., Detwiler, P.B., and Denk, W. (2009). Eyecup scope-optical recordings of light stimulus-evoked fluorescence signals in the retina. *Pflugers Arch.* 457, 1393–1414.
26. Miller, R.F., Fagerson, M.H., Staff, N.P., Wolfe, R., Doerr, T., Gottesman, J., Sikora, M.A., and Schuneman, R. (2001). Structure and functional connections of presynaptic terminals in the vertebrate retina revealed by activity-dependent dyes and confocal microscopy. *J. Comp. Neurol.* 437, 129–155.
27. Haverkamp, S., Grünert, U., and Wässle, H. (2000). The cone pedicle, a complex synapse in the retina. *Neuron* 27, 85–95.
28. Schubert, T., Weiler, R., and Feigenspan, A. (2006). Intracellular calcium is regulated by different pathways in horizontal cells of the mouse retina. *J. Neurophysiol.* 96, 1278–1292.
29. Feigenspan, A., and Babai, N. (2015). Functional properties of spontaneous excitatory currents and encoding of light/dark transitions in horizontal cells of the mouse retina. *Eur. J. Neurosci.* 42, 2615–2632.
30. Hirano, A.A., Liu, X., Boulter, J., Grove, J., de Sevilla Müller, L.P., Barnes, S., and Brecha, N.C. (2016). Targeted deletion of vesicular GABA transporter from retinal horizontal cells eliminates feedback modulation of photoreceptor calcium channels. *eNeuro* 3, ENEURO.0148-15.2016.
31. Ströh, S., Sonntag, S., Janssen-Bienhold, U., Schultz, K., Cimiotti, K., Weiler, R., Willecke, K., and Dedek, K. (2013). Cell-specific cre recombinase expression allows selective ablation of glutamate receptors from mouse horizontal cells. *PLoS ONE* 8, e83076.
32. Baden, T., Schubert, T., Chang, L., Wei, T., Zaichuk, M., Wissinger, B., and Euler, T. (2013). A tale of two retinal domains: near-optimal sampling of achromatic contrasts in natural scenes through asymmetric photoreceptor distribution. *Neuron* 80, 1206–1217.
33. Baden, T., Berens, P., Franke, K., Román Rosón, M., Bethge, M., and Euler, T. (2016). The functional diversity of retinal ganglion cells in the mouse. *Nature* 529, 345–350.
34. Hendel, T., Mank, M., Schnell, B., Griesbeck, O., Borst, A., and Reiff, D.F. (2008). Fluorescence changes of genetic calcium indicators and OGB-1 correlated with neural activity and calcium in vivo and in vitro. *J. Neurosci.* 28, 7399–7411.
35. Tian, L., Hires, S.A., Mao, T., Huber, D., Chiappe, M.E., Chalasani, S.H., Petreanu, L., Akerboom, J., McKinney, S.A., Schreiner, E.R., et al. (2009). Imaging neural activity in worms, flies and mice with improved GCaMP calcium indicators. *Nat. Methods* 6, 875–881.
36. Helmstaedter, M., Briggman, K.L., Turaga, S.C., Jain, V., Seung, H.S., and Denk, W. (2013). Connectomic reconstruction of the inner plexiform layer in the mouse retina. *Nature* 500, 168–174.
37. Franke, K., Berens, P., Schubert, T., Bethge, M., Euler, T., and Baden, T. (2017). Inhibition decorrelates visual feature representation in the inner retina. *Nature* 542, 439–444.
38. Schubert, T., Huckfeldt, R.M., Parker, E., Campbell, J.E., and Wong, R.O. (2010). Assembly of the outer retina in the absence of GABA synthesis in horizontal cells. *Neural Dev.* 5, 15.
39. Byzov, A.L., and Shura-Bura, T.M. (1986). Electrical feedback mechanism in the processing of signals in the outer plexiform layer of the retina. *Vision Res.* 26, 33–44.
40. Ueda, Y., Kaneko, A., and Kaneda, M. (1992). Voltage-dependent ionic currents in solitary horizontal cells isolated from cat retina. *J. Neurophysiol.* 68, 1143–1150.
41. Veruki, M.L., Olstedal, L., and Hartveit, E. (2008). Electrical synapses between All amacrine cells: dynamic range and functional consequences of variation in junctional conductance. *J. Neurophysiol.* 100, 3305–3322.
42. Shelley, J., Dedek, K., Schubert, T., Feigenspan, A., Schultz, K., Hombach, S., Willecke, K., and Weiler, R. (2006). Horizontal cell receptive

- fields are reduced in connexin57-deficient mice. *Eur. J. Neurosci.* **23**, 3176–3186.
43. Grimes, W.N., Li, W., Chávez, A.E., and Diamond, J.S. (2009). BK channels modulate pre- and postsynaptic signaling at reciprocal synapses in retina. *Nat. Neurosci.* **12**, 585–592.
 44. Liu, X., Grove, J.C., Hirano, A.A., Brecha, N.C., and Barnes, S. (2016). Dopamine D1 receptor modulation of calcium channel currents in horizontal cells of mouse retina. *J. Neurophysiol.* **116**, 686–697.
 45. Sun, X., Hirano, A.A., Brecha, N.C., and Barnes, S. (2017). Calcium-activated BK_{Ca} channels govern dynamic membrane depolarizations of horizontal cells in rodent retina. *J. Physiol.* **595**, 4449–4465.
 46. Szikra, T., Trenholm, S., Drinnenberg, A., Jüttner, J., Raics, Z., Farrow, K., Biel, M., Awatramani, G., Clark, D.A., Sahel, J.-A., et al. (2014). Rods in daylight act as relay cells for cone-driven horizontal cell-mediated surround inhibition. *Nat. Neurosci.* **17**, 1728–1735.
 47. Behrens, C., Schubert, T., Haverkamp, S., Euler, T., and Berens, P. (2016). Connectivity map of bipolar cells and photoreceptors in the mouse retina. *eLife* **5**, e20041.
 48. Seeliger, M.W., Brombas, A., Weiler, R., Humphries, P., Knop, G., Tanimoto, N., and Müller, F. (2011). Modulation of rod photoreceptor output by HCN1 channels is essential for regular mesopic cone vision. *Nat. Commun.* **2**, 532.
 49. Reifsnider, E.S., and Tranchina, D. (1995). Background contrast modulates kinetics and lateral spread of responses to superimposed stimuli in outer retina. *Vis. Neurosci.* **12**, 1105–1126.
 50. VanLeeuwen, M., Fahrenfort, I., Sjoerdsma, T., Numan, R., and Kamermans, M. (2009). Lateral gain control in the outer retina leads to potentiation of center responses of retinal neurons. *J. Neurosci.* **29**, 6358–6366.
 51. Cadenas, I.D., Reifsnider, E.S., and Tranchina, D. (1994). Modulation of synaptic transfer between retinal cones and horizontal cells by spatial contrast. *J. Gen. Physiol.* **104**, 567–591.
 52. Borst, A., and Theunissen, F.E. (1999). Information theory and neural coding. *Nat. Neurosci.* **2**, 947–957.
 53. Atick, J.J. (1992). Could information theory provide an ecological theory of sensory processing? *Network* **3**, 213–251.
 54. Storace, D.A., Braubach, O.R., Jin, L., Cohen, L.B., and Sung, U. (2015). Monitoring brain activity with protein voltage and calcium sensors. *Sci. Rep.* **5**, 10212.
 55. Dorostkar, M.M., Dreosti, E., Odermatt, B., and Lagnado, L. (2010). Computational processing of optical measurements of neuronal and synaptic activity in networks. *J. Neurosci. Methods* **188**, 141–150.
 56. Smith, R.G. (1992). NeuronC: a computational language for investigating functional architecture of neural circuits. *J. Neurosci. Methods* **43**, 83–108.
 57. Mank, M., Reiff, D.F., Heim, N., Friedrich, M.W., Borst, A., and Griesbeck, O. (2006). A FRET-based calcium biosensor with fast signal kinetics and high fluorescence change. *Biophys. J.* **90**, 1790–1796.
 58. Macé, E., Caplette, R., Marre, O., Sengupta, A., Chaffiol, A., Barbe, P., Desrosiers, M., Bamberg, E., Sahel, J.-A., Picaud, S., et al. (2015). Targeting channelrhodopsin-2 to ON-bipolar cells with vitreally administered AAV Restores ON and OFF visual responses in blind mice. *Mol. Ther.* **23**, 7–16.
 59. Deniz, S., Wersinger, E., Schwab, Y., Mura, C., Erdelyi, F., Szabó, G., Rendon, A., Sahel, J.A., Picaud, S., and Roux, M.J. (2011). Mammalian retinal horizontal cells are unconventional GABAergic neurons. *J. Neurochem.* **116**, 350–362.
 60. Werblin, F.S. (1978). Transmission along and between rods in the tiger salamander retina. *J. Physiol.* **280**, 449–470.
 61. Denk, W., Strickler, J.H., and Webb, W.W. (1990). Two-photon laser scanning fluorescence microscopy. *Science* **248**, 73–76.
 62. Breuninger, T., Puller, C., Haverkamp, S., and Euler, T. (2011). Chromatic bipolar cell pathways in the mouse retina. *J. Neurosci.* **31**, 6504–6517.
 63. Chang, L., Breuninger, T., and Euler, T. (2013). Chromatic coding from cone-type unselective circuits in the mouse retina. *Neuron* **77**, 559–571.

STAR★METHODS

KEY RESOURCES TABLE

REAGENT or RESOURCE	SOURCE	IDENTIFIER
Antibodies		
rabbit anti-M-opsin	EMD Millipore	AB5405; RRID: AB_177456
goat anti-S-opsin	Santa Cruz Biotechnology	SC-14363; RRID: AB_2158332
donkey anti-rabbit conjugated to Alexa Fluor 568	Invitrogen	A10042; RRID: AB_2534017
donkey anti-goat conjugated to Alexa Fluor 660	Invitrogen	A21083; RRID: AB_10374427
Virus Strains		
AAV9.hSyn.iGluSnFR.WPRE.SV40	Penn Vector Core	AV-9-PV2723
Chemicals, Peptides, and Recombinant Proteins		
NaCl	Sigma-Aldrich	433209
KCl	Sigma-Aldrich	P9441
MgCl ₂ x 6 H ₂ O	Merck	105833
NaH ₂ PO ₄	Sigma-Aldrich	S5011
NaHCO ₃	Merck	1.06329
glucose	Sigma-Aldrich	G8270
CaCl ₂	Sigma-Aldrich	C3306
L-glutamine	Sigma-Aldrich	G3126
Pyridoxal 5-phosphate	Sigma-Aldrich	P9255
Sulforhodamine 101	Sigma-Aldrich	S7635
6,7-dinitroquinoxaline-2,3-dione (NBQX)	Tocris Bioscience	1044
α -amino-3-hydroxy-5-methyl-4-isoxazolepropionic acid (AMPA)	Sigma-Aldrich	A6816
Kainic acid (KA)	Sigma-Aldrich	K0250
Muscimol	Tocris Bioscience	0289
SR-95531 hydrobromide (gabazine)	Tocris Bioscience	1262
Verapamil	Tocris Bioscience	0654
Thapsigargin	Tocris Bioscience	1138
Isoflurane	CP-Pharma	1214
Ketamine	Bela-Pharm GmbH	NA
Xylazine	Rompun, Bayer Vital GmbH	NA
Experimental Models: Organisms/Strains		
Mouse: Cx57 ^{cre/cre}	[31]	NA
Mouse: B6;129S-Gt(ROSA)26Sor ^{tm38(CAG-GCaMP3)Hze/J}	[20]; Jackson Lab	Stock No. 029043
Mouse: HR2.1:TN-XL	[21]	NA
Mouse: C57BL/6J	Jackson Lab	Stock No. 000664
Software and Algorithms		
ScanM	M. Müller, MPI for Neurobiology; and T. Euler	NA
IgorPro 6.37	Wavemetrics	https://www.wavemetrics.com/products/igorpro/igorpro.htm
SARFIA	[55]	http://www.igorexchange.com/project/SARFIA
Fiji	http://fiji.sc/Fiji	NA
Arduino	http://www.arduino.cc	NA
Knossos	https://knossostool.org/	NA
NeuronC	[56]	http://retina.anatomy.upenn.edu/~rob/neuronc.html

CONTACT FOR REAGENT AND RESOURCE SHARING

Further information and requests for resources and reagents should be directed to and will be fulfilled by the Lead Contact, Timm Schubert (timm.schubert@cin.uni-tuebingen.de).

EXPERIMENTAL MODEL AND SUBJECT DETAILS

Animals

For the Ca^{2+} imaging experiments in retinal horizontal cells (HCs), we crossed the transgenic mouse lines Cx57^{cre/cre} [31] and B6;129S-Gt(ROSA)26Sor^{tm38(CAG-GCaMP3)Hze/J} (Ai38) [20], yielding Cx57^{+/cre} × Ai38 mice, which express the Ca^{2+} biosensor GCaMP3 [35] under the control of the promoter for the gap junction-forming connexin57 (Cx57) selectively in HCs. For Ca^{2+} imaging in cone axon terminals, we used the HR2.1:TN-XL mouse line [21], which expresses the FRET-based Ca^{2+} biosensor TN-XL [57] exclusively in cones. TN-XL enables ratiometric Ca^{2+} measurements by determining the ratio between the signals of its two fluorophores, eCFP (FRET donor) and citrine (FRET acceptor), which are linked by the Ca^{2+} sensor troponin C (for details, see [21]). For glutamate imaging, iGluSnFR [22] was ubiquitously expressed in the retina after intra-vitreous virus injection in C57BL/6J mice (see Virus injection). We observed iGluSnFR expression predominantly in HCs, likely because bipolar cells express AAV constructs less efficiently [58]. Both male and female adult mice (4–18 weeks of age) were used. Animals were deeply anesthetized with isoflurane (CP-Pharma, Germany) and killed by cervical dislocation. All procedures were performed in accordance with the law on animal protection (Tierschutzgesetz) issued by the German Federal Government and approved by the institutional committee on animal experimentation of the University of Tübingen, Germany.

METHOD DETAILS

Retinal tissue preparation

For all imaging experiments, mice were dark adapted for at least 2 hr and then killed. Under dim red light, both eyes were marked at the ventral side to maintain retinal orientation, quickly enucleated, and hemisected in carboxygenated (95% O_2 /5% CO_2) extracellular solution with (in mM): 125 NaCl, 2.5 KCl, 1 MgCl_2 , 1.25 NaH_2PO_4 , 26 NaHCO_3 , 20 glucose, 2 CaCl_2 , 0.5 L-glutamine and 150 μM pyridoxal 5-phosphate (a cofactor of the glutamic acid decarboxylase [59]) (Sigma-Aldrich or Merck, Germany). Cornea, lens and vitreous body were carefully removed. The retina was separated from the eye-cup, cut in half, flattened, and mounted photoreceptor side-up on a nitrocellulose membrane (0.8 μm pore size, Millipore, Ireland). Using a custom-made slicer [60], acute vertical slices (300 μm thick) were cut parallel to the naso-temporal axis. Slices attached to filter paper were transferred on individual glass coverslips, fixed using high vacuum grease and kept in a storing chamber at room temperature for later use. For all imaging experiments, individual retinal slices were transferred to the recording chamber, where they were continuously perfused with warmed ($\sim 36^\circ\text{C}$), carboxygenated extracellular solution containing 0.5 μM sulforhodamine 101 (SR101; Sigma-Aldrich, Germany) to visualize cone axon terminals.

Virus injection

Before the injection of AAV9.hSyn.iGluSnFR.WPRE.SV40 (Penn Vector Core, PA, USA), mice (5–7 weeks) were anaesthetized with 10% ketamine (Bela-Pharm GmbH, Germany) and 2% xylazine (Rompun, Bayer Vital GmbH, Germany) in 0.9% NaCl (Fresenius, Germany). A Hamilton syringe (syringe: 7634-01, needle: 207434, point style 3, length 51 mm, Hamilton Messtechnik GmbH) containing the virus was fixed on a micromanipulator (M3301, World Precision Instruments, Germany) at an angle of 15° . Then, 1 μl of the virus was injected into the naso-ventral part of the vitreous body [37]. Recordings were performed 3 weeks after the injection.

Two-photon imaging

Ca^{2+} and glutamate signals were recorded on a customized MOM-type two-photon microscope (Sutter Instruments, Novato, CA; designed by W. Denk, MPI for Neurobiology, Martinsried, Germany) [25, 61], equipped with a mode-locked Ti:Sapphire laser (MaiTai-HP DeepSee; Newport Spectra-Physics, Germany) tuned to either 860 or 927 nm for TN-XL and GCaMP3/iGluSnFR excitation, respectively, and a 20x water-immersion objective (XLUMPlanFL, 0.95 NA, Olympus, Germany, or W Plan-Apochromat 20x/1.0 DIC M27, Zeiss, Germany). Two PMTs with appropriate band-pass filters were used to detect the fluorescence emission of (a) TN-XL/citrine, GCaMP3 (538 BP 50, AHF, Germany) or iGluSnFR (510 BP 84), and (b) TN-XL/eCFP (483 BP 32) or SR101 (630 BP 60). We acquired time-lapsed image series with the custom software ScanM (by M. Müller, MPI for Neurobiology, and T. Euler) running under IgorPro 6.37 (Wavemetrics, Lake Oswego, OR, USA). Images of 128 × 64 pixels (51.8 × 28.2 μm or 38.7 × 20.8 μm) at a frame rate of 7.8125 Hz were recorded for all visual stimuli except the “coloured noise” and binary noise stimuli (see below), where we used images of 128 × 16 pixels (51.8 × 7.1 μm or 38.7 × 5.2 μm , at 31.25 Hz; Figure S1A). Recording fields were always located at the outer plexiform layer (OPL) to prevent bleaching of the cone outer segments by the scanning laser [21, 32].

Because SR101 is endocytosed by terminals of synaptically active cells such as photoreceptors [26], we performed control experiments to rule out that SR101 fluorescence in the “red” channel contributed to the activity signals measured in the “green” channels. To this end, we presented light flashes to retinal slices from C57BL/6 mice bathed in SR101 and recorded the fluorescence signal in

both channels. Indeed, we did not find any light stimulus-dependent signal modulation in the red channel (data not shown). Furthermore, we did not detect any substantial SR101 fluorescence in the green channel.

Light stimulation

Full-field light stimuli were generated by two band-pass-filtered LEDs (UV, 360 BP 12; green, 578 BP 10; AHF) driven by an open-source microprocessor board (<http://www.arduino.cc>) and synchronized with the scanner retrace to avoid light stimulus artifacts during image acquisition. The light from the two LEDs was combined by a beam-splitter (400 CDLP, AHF) and focused on the retinal slice through the bottom of the recording chamber via a condenser lens (H DIC, 0.8 NA, Zeiss). The intensity of each LED was adjusted such that the photoisomerisation (P^*) rate in S-cones elicited by the UV LED was equal to the P^* rate elicited by the green LED in M-cones [62, 63]. The light intensity generated by each LED was equivalent to P^* rates (in P^*s^{-1}/cone) ranging from $0.5 \cdot 10^3$ (I_{MIN}) to $6.5 \cdot 10^3$ (I_{MAX}) for all stimuli except the binary noise stimulus ($I_{\text{MIN}} = 0.6 \cdot 10^3$, $I_{\text{MAX}} = 19 \cdot 10^3$), where a different light stimulator was used (for details, see [37]). Note that the two-photon excitation laser caused an additional steady background illumination (I_{BKG}) of approx. $10^4 P^*s^{-1}/\text{cone}$ [21, 32], which likely amounts to a similar P^* rate in rods [25]. Under these stimulus conditions, it is unlikely that rods are operational (see Discussion).

Note that we use the term “white” to refer to the simultaneous stimulation with both LEDs with the same P^* rate. All following 5 stimulus protocols were preceded by a 15 s period that allowed the photoreceptors adapting to the background ($I_{\text{MIN}} + I_{\text{BKG}}$):

- A white flash protocol consisting of 1 s bright flashes (from a background of I_{MIN} to I_{MAX}) of “mouse-white” (both LEDs on) at 0.2 Hz. This protocol was used to assess drug effects on light-evoked Ca^{2+} responses.
- A color flash protocol consisting of bright green, UV and white 1 s flashes (“GUW”) at 0.2 Hz and repeated 10 times for each color (same intensity levels as for (a)). This protocol was used to determine the spectral contrast (SC, see below) preference.
- A contrast and color flash protocol consisting of 1 s bright and dark flashes, with the respective LED combinations (green, UV, and white) at I_{MAX} or I_{MIN} , respectively, at 0.2 Hz and repeated 8 times for each condition (Intensity between flashes: $3 \cdot 10^3 P^*s^{-1}/\text{cone}$). This protocol was used to determine the SC and the dark-light index (DLi , see below).
- A “coloured noise” stimulus protocol consisting of a 25 Hz pseudo-random sequence of green, UV, white, and dark flashes. This protocol was used to probe correlation between neighboring cones and HC processes and to calculate time kernels (see below).
- A binary noise stimulus protocol consisting of a 60-Hz pseudo-random sequence of dark and bright flashes. This protocol was also used to calculate time kernels.

Immunohistochemistry

After two-photon imaging, a subset of retinal slices were fixed with 4% paraformaldehyde (PFA) in 0.1 M phosphate-buffered saline (PBS) at 4°C for 15 min. Slices were then washed in 0.1 M PBS, and submerged in blocking solution (0.1 M PBS, 0.3% Triton X-100, 10% donkey serum) overnight at 4°C . Afterward, slices were incubated for 4 days at 4°C with primary antibodies (rabbit anti-M-opsin (1:1,000) from EMD Millipore, Billerica, MA, USA; goat anti-S-opsin (1:500) from Santa Cruz Biotechnology (Germany) in 0.1 M PBS, 0.3 Triton X-100, and 5% donkey serum. The following day, slices were washed in 0.1 M PBS and incubated with the secondary antibodies (donkey anti-rabbit conjugated to Alexa Fluor 568 (1:1000) and donkey anti-goat conjugated to Alexa Fluor 660 (1:1000), both Invitrogen, Carlsbad, CA, USA). Image stacks (15 frames of 1024×1024 pixels, $15 \mu\text{m}$ Z-steps) were acquired on a confocal laser-scanning microscope (Leica TCS SP8, Germany) which was equipped with green (552 nm) and far-red (638 nm) lasers and a 10×0.3 NA objective lens (Leica). Maximum-intensity projections of the image stacks were performed using Fiji (<http://fiji.sc/Fiji>).

Pharmacology and drug application

All drugs were prepared as stock solutions in distilled water or, in the case of thapsigargin, in DMSO (0.1% in the extracellular medium), and were stored at -20°C . Before each experiment, drugs were freshly diluted from stock solution in carboxygenated extracellular solution. For puff application, a glass electrode (tip diameter: 1–2 μm) was placed approx. 100 μm above the recorded region of the slice and drug solution was puffed for 10 s using a pressure application system (0.2–1 bar, Sigmam Elektronik GmbH, Germany). The lateral spread of the puff was about 200 μm in diameter, as measured by puffing a fluorescent dye (SR101). For bath application, the tissue was perfused with the drug added to the bathing solution for 5 min or, in the case of thapsigargin, for 20 min (perfusion rate of ~ 1.5 mL/min). For puff application, the following concentrations were used (in μM): 200 6,7-dinitroquinoxaline-2,3-dione (NBQX), 50 α -amino-3-hydroxy-5-methyl-4-isoxazolepropionic acid (AMPA), 25 kainic acid (KA), 100 muscimol and 100 SR-95531 hydrobromide (gabazine). For bath application, we used (in μM): 100 verapamil, 5 thapsigargin and 100 NBQX. All drugs were purchased from Tocris Bioscience (Bristol, England) except for KA, which was purchased from Sigma-Aldrich.

Data analysis

To analyze light-evoked Ca^{2+} signals in HCs and cones, as well as glutamate release in the OPL, we used custom-written scripts in IgorPro (Wavemetrics) and SARFIA [55]. For GCaMP3 and TN-XL fluorescence (Ca^{2+} in HCs and cones, respectively), regions-of-interest (ROIs) were anatomically defined using SARFIA’s automatic Laplace operator feature on the averaged, filtered image series and manually corrected if required (e.g., if two nearby structures shared one ROI); ROIs with an area < 10 pixels were discarded.

For iGluSnFR fluorescence (glutamate release), the correlation over time between neighboring pixels was measured and ROIs were determined based on a correlation threshold (defined for each recording depending on the signal-to-noise ratio). ROI diameters were limited to range between 5 to 8 μm (diameter of a cone axon terminal).

To determine the spatial resolution of our system, we measured the point spread function (PSF) using fluorescent beads (0.17 μm in diameter; Invitrogen) and found the resolution (Abbe) limited to 0.6 μm in the x-y plane and 4.1 μm along the z axis (FWHM of Gaussian fit, green channel). Cone axon terminals measure approx. 5 μm in diameter, distal HC dendrites between 1 to 2 μm [38]. Therefore, both can be resolved in the x-y plane. Due to the limited z resolution, it is possible that a ROI averaged across multiple fine distal HC dendrites stacked along the z axis. In case of the much larger cone axon terminals, averaging across two stacked ones is unlikely but cannot be excluded. In any case, however, since such averaging is not expected to increase functional diversity between individual ROIs, it should not have affected our conclusions.

To estimate each ROI's "vertical" position within OPL, the positions of cone axon terminals were visualized using SR101 fluorescence (Figures 1C and 1D). Here, cone axon terminals can be identified because they are more brightly stained compared to rod axon terminals and HC processes, and because they are organized along the OPL like beads on a string. A ROI's distance to the cone axon terminal base (d_{base}) was estimated relative to a manually drawn straight line tracing the base of all cone axon terminals in a recorded field, using the shape transition in brightness between the cone axon terminals and the weakly labeled HC dendrites below as a landmark.

For TN-XL, the ratio between acceptor (citrine) and donor fluorescence (eCFP) was calculated on the image series, prior to signal extraction. For all indicators, time traces were extracted for each ROI, de-trended by high-pass filtering at ~ 0.1 Hz (except for the analysis of drug effects on the baseline) and z-normalized ($F'_i = (F_i - \mu) / \sigma$, with samples F_i , and mean (μ) and SD (σ) of the trace). For all flash stimuli, we determined response amplitude (ΔF), area-under-the-curve (F_{Area}) and, in case of NBQX, muscimol and gabazine puffs, as well as for the contrast and color flash protocol, also the Ca^{2+} baseline level (F_0). These parameters were measured on the trace smoothed using IgorPro's boxcar algorithm with 2 passes for all stimuli (except for drug experiments, where 5 passes were used).

Two quality criteria were defined to identify responsive ROIs: The **quality index** (Q_i) is defined as the ratio between ΔF in response to a white flash and the SD of the noise of the trace (= raw trace minus the trace smoothed using IgorPro's boxcar algorithm with 2 passes). For stimulus protocol (c), Q_i was calculated independently for dark and bright flashes. Depending on stimulus and experiment type, we used different Q_i thresholds applied to the responses to white stimuli ($Q_i \geq 1$ for all flash protocols except (c) which employed fewer stimulus repeats, where we used $Q_i \geq 1.5$, and for AMPA/KA puffs, where we used $Q_i \geq 3$). The **consistency index** (C_i) is defined as the ratio between the variance of the mean and the mean of the variance across $n = 8$ to 10 stimulus trials [33]. ROIs with $C_i \geq 0.2$ were considered to show consistent light-evoked Ca^{2+} responses over time. For all experiments involving light stimuli, only ROIs that passed both criteria were included for further analysis.

Depending on the stimulus protocol, we determined additional parameters for each ROI: We calculated the **spectral contrast preference**, $SC = (F_{\text{Area}(G)} - F_{\text{Area}(UV)}) / (F_{\text{Area}(G)} + F_{\text{Area}(UV)})$, using the F_{Area} for the responses to green and UV flashes (protocol (b)). The **dark-light index**, $DLi = (F_{\text{Area}(B)} - F_{\text{Area}(D)}) / (F_{\text{Area}(B)} + F_{\text{Area}(D)})$ [32], was determined using the F_{Area} for the responses to bright and dark white flashes (protocol (c)).

The data recorded with the colored noise stimulus (protocol (d); cf. Figure 4) were analyzed by calculating the negative transient-triggered average from the de-trended and z-normalized Ca^{2+} traces, weighted by the transients' amplitudes, yielding a temporal receptive field (time kernel) for each ROI. A ROI was considered light-responsive if the maximum amplitude of the kernel (A_{LRF}) for green and/or UV was $A_{\text{LRF}} > 2$ SD of the noise. All kernels were then normalized to 1. We then calculated the correlation between ROIs present in the same field either for the full Ca^{2+} traces or for negative events (with amplitudes < -2 SD of the noise) in a time window of -750 to 250 ms around the event (at 0 ms). The mean correlation for each field was then used for further analysis. An equivalent approach was used to analyze the data recorded with the binary noise (protocol (e); cf. Figure 6); with ROIs considered responsive if $A_{\text{LRF}} > 3$ SD noise. A periodogram was generated by applying a discrete Fourier transform (DFT) to the time-series of each kernel without zero padding. The power spectral densities at each frequency component followed approximately a log-normal distribution, and so to improve Gaussianity (assumed in the subsequent t tests), a log transform was applied to each periodogram, and the transformed data were used for statistical comparisons.

Modeling voltage and Ca^{2+} spread across HC dendrites

To evaluate the voltage and Ca^{2+} spread across HC dendrites (Figure 5), we built a biophysically realistic model using the simulation language NeuronC [56]. To this end, we reconstructed an HC dendritic branch and its cone contacts from a published EM dataset (e2006; [36]) using Knossos (<https://knossos-tool.org>). The model includes AMPA-type glutamate receptors at the cone synapses and voltage-gated Ca^{2+} and K^+ channels modeled as Markov state machines with different densities for tips and dendrites (for parameters, see Table below). Photoreceptors are already pre-defined in NeuronC; they were modeled as single compartments that included voltage-gated Ca^{2+} and Ca^{2+} -activated Cl^- channels. We adjusted channel densities such that the model's membrane voltage stays in a physiologically plausible range but did not further tune the model. However, changing the membrane resistance and channel densities within the physiological range did not alter voltage and Ca^{2+} spread considerably (data not shown).

Parameters of biophysical model of HC dendritic branch

Rm	[Ω cm ²]		2,500
Ri (Ω cm ²)	[Ω cm ²]		200
Channel densities			
L-type Ca ²⁺ channels	[S/cm ²]	Soma and proximal dendrites	3e-4
		Distal dendrites	1e-3
K ⁺ channels	[S/cm ²]	Soma and proximal dendrites	1e-5
		Distal dendrites	1e-5

QUANTIFICATION AND STATISTICAL ANALYSIS





All statistical tests (except for the ones for the periodograms) were performed using the Wilcoxon signed-rank test or the Wilcoxon rank-sum test. Alpha was set to 0.05 and p values (p) < 0.05 were considered as significant (*), p < 0.01 (**), p < 0.001 (***). For multiple comparisons, Bonferroni correction was used and p < 0.025 was considered as significant (+), p < 0.005 (++) , p < 0.0005 (+++). For periodograms, a dependent sample t test was computed for each positive frequency component and Bonferroni correction was used (15 comparisons, cf. Figure 6). Spearman rank correlation test was used to estimate the correlation between negative events and distance along the slice (cf. Figure 4) as well as the relationships between DLi , SC , slice position and F_o (cf. Figure S1). Differences between dorsal and ventral DLi were assessed with t test and Bartlett test. Errors are given as standard error of the mean (SEM), median absolute deviation (MAD) or standard deviation (SD).

DATA AND SOFTWARE AVAILABILITY

Data analysis was coded in Igor Pro and NeuronC. Data and model code are available at <http://retinal-functomics.net/>.

SYMPOSIUM REVIEW

Connectomics of synaptic microcircuits: lessons from the outer retina

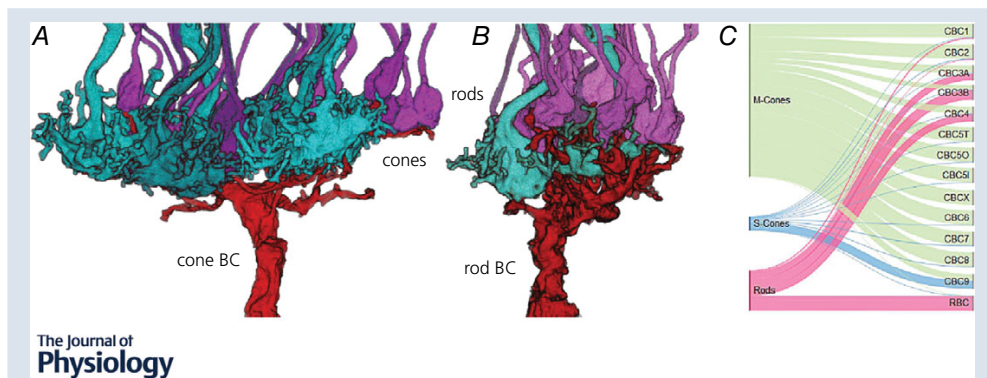
Luke Edward Rogerson^{1,2,3,4}, Christian Behrens^{1,2,3,4} , Thomas Euler^{1,2,3} , Philipp Berens^{1,2,3}  and Timm Schubert^{1,2} 

¹Institute for Ophthalmic Research, University of Tübingen, 72076 Tübingen, Germany

²Centre for Integrative Neuroscience, University of Tübingen, 72076 Tübingen, Germany

³Bernstein Center for Computational Neuroscience, University of Tübingen, 72076 Tübingen, Germany

⁴Graduate Training Centre of Neuroscience, University of Tübingen, 72076 Tübingen, Germany



Abstract Photoreceptors form a sophisticated synaptic complex with bipolar and horizontal cells, transmitting the signals generated by the phototransduction cascade to downstream retinal circuitry. The cone photoreceptor synapse shows several characteristic anatomical connectivity motifs that shape signal transfer: typically, ON-cone bipolar cells receive photoreceptor input through invaginating synapses; OFF-cone bipolar cells form basal synapses with photoreceptors.

Luke Rogerson obtained a BSc in Human Genetics at the University of Nottingham and an MSc in Computational Neuroscience at the University of Birmingham before starting a PhD at the University of Tübingen. **Christian Behrens** studied Theoretical Physics in Heidelberg and Munich before starting a PhD at the University of Tübingen. **Thomas Euler** obtained a diploma in Biology and a PhD in Neuroscience at the University of Mainz and the Max-Planck Institute for Brain Research in Frankfurt. After being a postdoctoral fellow at the Harvard Medical School in Boston and the MPI for Medical Research in Heidelberg, he is now a full professor for Ophthalmology at the Institute for Ophthalmic Research/Centre for Integrative Neuroscience in Tübingen. **Philipp Berens** studied Bioinformatics and Philosophy in Tübingen and obtained a PhD from the International Max Planck Research School at the University of Tübingen. He was a postdoctoral researcher at the Bernstein Center for Computational Neuroscience in Tübingen before he became a group leader at the Institute for Ophthalmic Research at the University of Tübingen. **Timm Schubert** studied Biology in Oldenburg, where he also obtained his PhD in Neuroscience. He was a postdoctoral fellow at the University of Washington in Seattle, and is now a senior researcher at the Institute for Ophthalmic Research and the Centre for Integrative Neuroscience in Tübingen.



L. E. Rogerson and C. Behrens contributed equally to this work.

This review was presented at the symposium “Phototransduction and synaptic transmission” which took place at the Phototransduction UK workshop, Sheffield, 31 August – 2 September 2016.

Both ON- and OFF-cone bipolar cells are believed to sample from all cone photoreceptors within their dendritic span. Electron microscopy and immunolabelling studies have established the robustness of these motifs, but have been limited by trade-offs in sample size and spatial resolution, respectively, constraining precise quantitative investigation to a few individual cells. 3D-serial electron microscopy overcomes these limitations and has permitted complete sets of neurons to be reconstructed over a comparatively large section of retinal tissue. Although the published mouse dataset lacks labels for synaptic structures, the characteristic anatomical motifs at the photoreceptor synapse can be exploited to identify putative synaptic contacts, which has enabled the development of a quantitative description of outer retinal connectivity. This revealed unexpected exceptions to classical motifs, including substantial interaction between rod and cone pathways at the photoreceptor synapse, sparse photoreceptor sampling and atypical contacts. Here, we summarize what was learned from this study in a more general context: we consider both the implications and limitations of the study and identify promising avenues for future research.

(Received 30 November 2016; accepted after revision 10 February 2017; first published online 10 March 2017)

Corresponding author Timm Schubert: Institute for Ophthalmic Research, Centre for Integrative Neuroscience, University of Tübingen, 72076 Tübingen, Germany. Email: timm.schubert@cin.uni-tuebingen.de

Abstract figure legend Photoreceptor-Bipolar Cell Connectivity A,B Volume-rendered cone bipolar cell dendritic tree (A, cone BC, red) and rod bipolar cell dendritic tree (B, rod BC, red) with cone (cyan) and rod (purple) contacts, from the Helmstaedter *et al.* (2013) and Behrens *et al.* (2016) electron microscopy dataset. C, Connectivity map between M- and S-cones, rods and BCs, as developed in Behrens *et al.* (2016) demonstrating the high level of interconnectivity between the 'parallel' rod and cone pathways. Connectivity is scaled to show proportion of BC input received from each photoreceptor type.

Abbreviations BC, bipolar cell; CBC, cone bipolar cell; EM, electron microscopy; OPL, outer plexiform layer; RBC, rod bipolar cell.

Introduction

The mammalian photoreceptor synapse. The mouse is a crucial model system for retinal research. From three types of photoreceptors, the visual signal rapidly diverges into multiple parallel functional pathways comprising 14 types of bipolar cell and over 30 types of ganglion cell (Euler *et al.* 2014; Baden *et al.* 2016) (Fig. 1A and B). Each pathway differs in its preference for light stimulus features, with some encoding colour, changing luminance or motion. The photoreceptor synapse is one of the most complex synaptic structures in the central nervous system, exhibiting a high degree of both divergent and convergent connectivity with postsynaptic neurons (Haverkamp & Waesle, 2000) (see for example Fig. 1C).

Anatomical investigations into mouse photoreceptor circuitry have revealed a diverse system of synapses, with as many as 10 distinct (ribbon) release sites per photoreceptor (Tsukamoto *et al.* 2001) synapsing onto bipolar cells, the downstream partners in this circuit (Helmstaedter *et al.* 2013; Greene *et al.* 2016) (Fig. 1B and C). Laterally organized inhibitory interneurons, the horizontal cells, play a critical role in this synapse through excitatory and inhibitory modulation of neurotransmitter release at the photoreceptor axon terminal (reviewed in Thorson & Mangel, 2012; Vroman *et al.* 2013; Kramer &

Davenport, 2015) (Fig. 1A and D). In all, the evidence suggests that the photoreceptor synapse is the site of highly sophisticated functionality, with the subtleties of its connectivity having only recently become a subject of systematic approaches.

Though progress had been made towards a complete systematic connectivity map of the inner retina (Anderson *et al.* 2011; Helmstaedter *et al.* 2013), in this respect the outer retina had been mostly neglected, barring the dendritic connectivity for a few bipolar cell types (Tsukamoto & Omi, 2014). The recent availability of serial block face scanning electron microscopy datasets of retinal tissue, alongside advances in electrophysiological and functional imaging methods, presents an opportunity to address this deficit (Tsukamoto *et al.* 2007; Denk *et al.* 2012; Helmstaedter *et al.* 2013; Kim *et al.* 2014). Several factors also lend themselves to this goal, not least of which is the growing body of literature characterizing each of the neurons in the retina in terms of their anatomy, physiology and function, with a growing emphasis on the pre- and postsynaptic elements of the photoreceptor synapse (Baden *et al.* 2013; Grabner *et al.* 2016). Isolating the contribution of the photoreceptor microcircuitry to the dynamics of signalling in the outer plexiform layer (OPL) is becoming an attainable, though nonetheless challenging, goal.

Structural insights into the microcircuit complexity of the outer plexiform layer. The collection of major anatomical motifs constitute a ‘classical’ view of photoreceptor connectivity for which there is a widespread consensus and considerable support in the literature. In this classical view, bipolar cells densely sample from all photoreceptors within their dendritic field, chromatic pathways are strictly segregated, rod and cone bipolar cell pathways are largely independent at the photoreceptor synapse, but are interconnected in the inner retina, and synaptic transmission occurs exclusively through invaginating and basal contacts.

However, systematic investigations into the generality of these motives so far have been hampered by the limited resolution of (standard) microscopy used for immuno-

labelling studies or by small sample sizes (due to the relatively labour-intensive task of cell tracing) in the case of electron microscopy (EM) data. Motifs identified in these parallel approaches have therefore lacked either the spatial resolution to show they are not spurious connections or the sample size to confirm that they are robustly expressed. Both issues were addressed in a recent study by Behrens *et al.* (2016), which identified additional ‘atypical’ motifs in the wiring between photoreceptors and bipolar cells.

The quantitative study by Behrens *et al.* (2016) exploited a published EM dataset which reconstructed a volume of the mouse retina (Helmstaedter *et al.* 2013). They found that the cone and the rod pathway, responsible for day and night vision, respectively, display a high degree of overlap at the level of the photoreceptor synapse. This

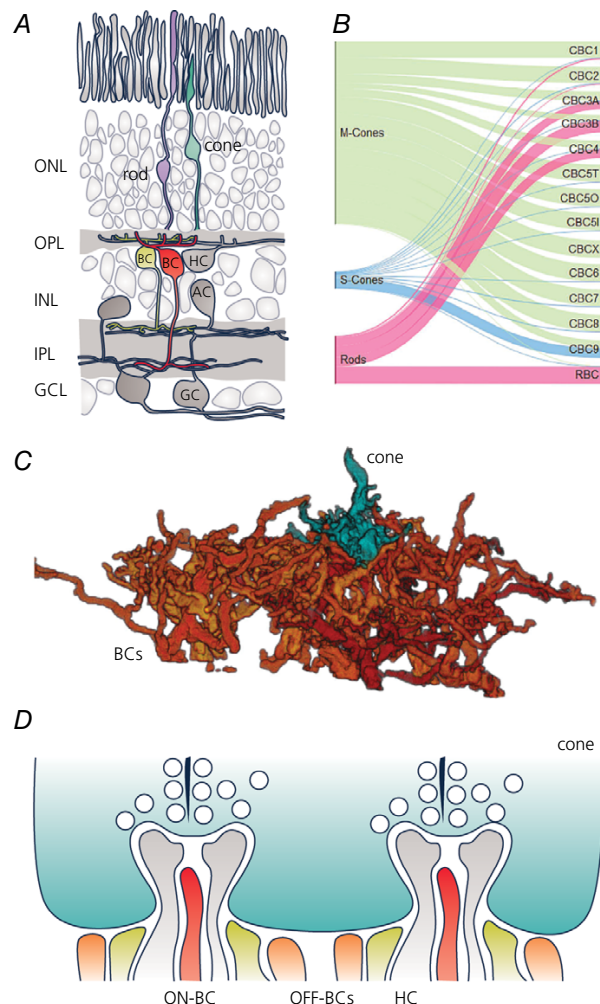


Figure 1. Connectivity of cone photoreceptors and cone bipolar cells

A, vertical view of the mouse retina with five classes of retinal neurons organized by stratification. *B*, quantitative connectivity map between cones, rods and bipolar cells (BCs). Photoreceptor types are shown on the left, and BC types are shown on the right. Connectivity is scaled to show proportion of BC input received from each photoreceptor type. *C*, cone axon terminal (cyan) and contacted postsynaptic cone BC dendrites (red, orange), demonstrating the divergence at the photoreceptor synapse. *D*, two ribbon synapses from a single mouse cone axon terminal (cyan) with postsynaptic partners: invaginating ON-cone bipolar cells (CBCs) (red) and horizontal cells (grey). OFF-CBCs (yellow, orange indicate dendrites from different cells) forming basal contacts. Note that only two cone ribbon synapses are shown, from the total set of 10. AC, amacrine cell; GC, ganglion cell; GCL, ganglion cell layer; HC, horizontal cell; INL, inner nuclear layer; IPL, inner plexiform layer; ONL, outer nuclear layer; OPL, outer plexiform layer.

suggests that these two pathways are also functionally more intertwined than was previously assumed. Another finding was that several ON-cone bipolar cell types do not sample all cones within their dendritic span, but rather a subset; why some cones are left out by these cells remains unclear. The findings of Behrens *et al.* (2016) built on the classical view of photoreceptor connectivity. One aspect of this, the segregation of the chromatic signals in two bipolar cell types in the mouse retina (Haverkamp *et al.* 2005; Breuninger *et al.* 2011; Mills *et al.* 2014), was confirmed by the data; the only wavelength-selective cone bipolar cell (CBC) types are the M-cone selective CBC1 and the S-cone selective CBC9, whereas all other bipolar cell (BC) types contact both S- and M-cones to varying degrees and are therefore achromatic.

In addition, Behrens and co-workers identified several motifs which were often overlooked in the classical view. Some ON-CBC types (CBC5T, 5O, 8) sampled sparsely from their large dendritic field, and many cones in turn sparsely contact these BC types. Assuming that ON-CBCs make synaptic connections only at their dendritic tips, these results imply that they can only get input from this subset of cones. One ON-CBC type, the CBCX, sampled only from one or two cones within its dendritic field; its dendrites often terminated a few micrometres below the base of other cone pedicles. Electrophysiological data, however, suggest that CBCX cells receive robust input from cones (Ichinose *et al.* 2014); the relevance of the seemingly blindly ending CBCX dendrites remains uncertain. In addition, the independence of the cone and rod pathways at the photoreceptor synapse was called into question, with conserved anatomical connections being highly indicative of a functional relevance. There is some precedence for this in the literature, both for the connectivity of cones to rod bipolar cells (RBCs) and rods to OFF-CBCs (Tsukamoto *et al.* 2001; Pang *et al.* 2010), although the extent to which RBCs sampled from cones and CBC3B cells sampled from rods was unanticipated (Figs 1B and 2).

Heuristics for the identification of synapses. A notable deficiency of this EM dataset was that it did not contain labelling for synaptic markers, and so identification of synapses based on objective criteria was inapplicable. Consequently, such a dataset presents several interpretive difficulties. The existence of a contact point between two cells does not necessarily imply a functional (synaptic) connection, and similarly the absence of a clear anatomical contact does not indicate the absence of synaptic communication (for a more detailed discussion see Helmstaedter, 2013; Morgan & Lichtman, 2013). In fact, a straightforward automated approach which treats the likelihood of a synapse as a function of the area of the contacting surface, which Helmstaedter *et al.* (2013) used in the inner retina, misclassifies many (probable) non-synaptic contacts in the OPL, such as dendrites

passing by the sides of a photoreceptor axon terminal or contacting cone telodendria, while missing the basal contacts that have a low surface area but are known to be central to the system.

This absence of labelled synapses in the dataset could be addressed to a large degree by identifying contacts that match the well-known stereotypical anatomy of the cone pedicle, which had been shown through EM with synaptic labelling and immunohistochemistry to have invaginating synapses, with the OFF-CBCs making basal contacts close to the synaptic cleft. Behrens *et al.* (2016) trained a support vector machine to classify each photoreceptor–bipolar cell pair as having a contact or not, using seven distinct features, including contact area, height and eccentricity. Their method allowed true and false contacts to be distinguished with around 90% accuracy (by using a cross-validation of performance with a manually labelled training dataset and using separate classifiers for OFF-, ON-CBCs and RBCs; for details, see original publication), suggesting that an automated approach to synapse identification is highly feasible for contacts in the OPL (see also Staffler *et al.* 2017). Unfortunately, a validation of the method on a dataset with synaptic markers was not possible at this point due to the lack of a publicly available large-scale EM dataset with conventional staining that includes the outer plexiform layer.

The utility of large electron microscopy datasets. Interestingly, the study by Behrens *et al.* (2016) illustrates that when approached with a specific question, large EM datasets can yield useful insights into neural circuits even without crowd-sourced large scale tracing efforts (Helmstaedter *et al.* 2011, 2013; Kim *et al.* 2014). The anatomical tracing of photoreceptor axon terminals required for the project could be achieved by two scientists within a few weeks. In this case, the well-known stereotypical photoreceptor anatomy allowed relatively straightforward tracing. Similar results have been obtained when focusing on certain cell types like starburst amacrine cells that can be recognized relatively easily by their morphology (Briggman *et al.* 2011; Ding *et al.* 2016). This is not to call into question the value of large-scale EM based explorations of anatomical diversity in the retina, which fundamentally require exhaustive tracing of all neurons in the circuitry (Helmstaedter, 2013; Kim *et al.* 2014; Greene *et al.* 2016; museum.eyewire.org). In addition, the study highlights the value of open data sharing, allowing others to build on the existing work in a straightforward manner. This is particularly important for labour-intensive datasets like EM with anatomical annotations.

Discussion

Anatomical features, ranging in scale from tens of nanometres through to hundreds of micrometres, play

a pivotal role in the functionality of outer retinal circuitry. Though similar complexity has been observed in other neural structures, the experimental accessibility and growing body of literature associated with the outer retina make it a particularly appealing model for exploring the broader functional implications of highly conserved anatomical motifs that are present on a scale of nanometres.

Evidence for a previously underemphasized interaction between rod and cone pathways has grown in the past few years, with considerable interconnectivity present in both the inner and outer retina: cones and rods are electrically coupled and can transmit signals via gap junctions (Asteriti *et al.* 2014), horizontal cells can switch between cone and rod signalling (Szikra *et al.* 2014), AII amacrine cells form connections with both rod and cone bipolar cells (reviewed in Anderson *et al.* 2011; Demb & Singer, 2012), and finally, both AII and A8 amacrine cells are electrically coupled to ON-CBCs (Lee *et al.* 2015). This latter connection suggests that other direct lateral signalling pathways between the rod and cone pathways exist, a

theory supported by anatomical evidence for crossover inhibition between the cone and rod pathways in the inner retina (Lauritzen *et al.* 2017). Other studies (Tsukamoto *et al.* 2001; Pang *et al.* 2010) anticipated, to some degree, an atypical connectivity between photoreceptors and bipolar cells now described by Behrens *et al.* (2016), but the extent of this connectivity was unexpected, particularly the high number of rod-to-OFF-CBC contacts. On the other hand, the findings of Behrens *et al.* (2016) are in contrast to another study that could find only minor functional significance of the rod-to-OFF-CBC synapse in the mouse retina (Protti *et al.* 2005). In addition, the existence of rod-to-ON-CBC contacts as suggested by Pang *et al.* (2010) could not be confirmed.

The newly described connectivity at the photoreceptor synapse raises fundamental questions about the functional role of these anatomical features. Traditionally, the synapse between rods and RBCs was considered to be non-linear (Field & Rieke, 2002; Bernston *et al.* 2004; Taylor & Smith, 2004), with a putative non-linearity on the postsynaptic bipolar cell side (Okawa & Sampath, 2007), whereas the

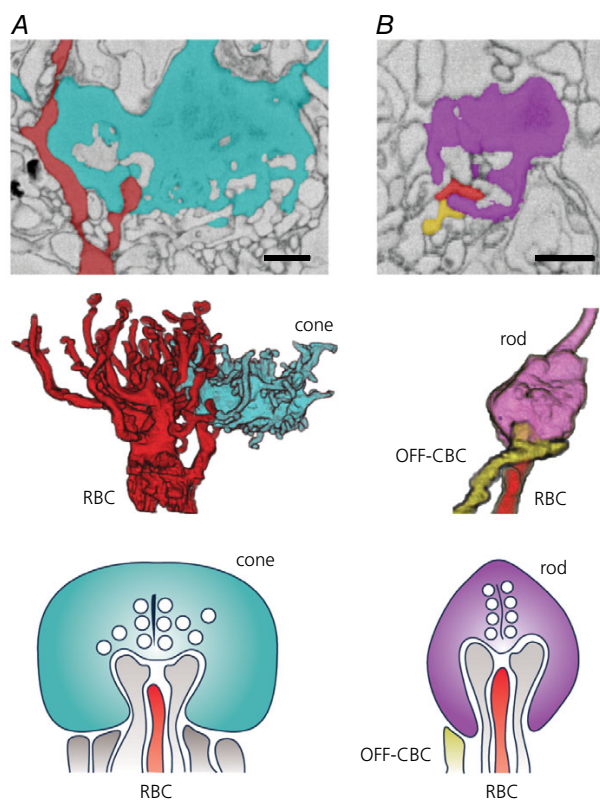


Figure 2. Crossover contacts between cones and rod photoreceptors and bipolar cells

A, vertical electron microscopy image (top), 3D-volume-rendered cells (middle) and representative scheme (bottom) showing a cone axon terminal (cyan) with an invaginating rod bipolar cell (RBC) dendrite (red). *B*, vertical electron microscopy image (top), 3D-volume-rendered cells (middle) and representative scheme (bottom) showing a rod axon terminal (purple) with invaginating RBC dendrite (red) and OFF-CBC making a basal contact (yellow). Scale bars: 1 μm .

synapse between cones and CBCs is often assumed to be linear (e.g. Euler *et al.* 2014). However, there is also evidence in favour of the rod-to-OFF-CBC synapse also being linear in some light stimulus regimes (Li *et al.* 2010). Moreover, the finding of invaginating cone-to-RBC synapses raises the question as to whether this synapse is linear or non-linear. Additionally, it is entirely unclear if the glutamate release at an invaginating cleft occupied by a RBC dendrite is modulated by feedback from horizontal cell dendrites. Thus, the functional relationship between cones and RBCs is ambiguous, and would benefit from targeted investigation.

Another synaptic feature, the transfer function relating the output of presynaptic neurons to the activity of post-synaptic cells, is a natural point of focus (Turrigiano, 2011; Lambo & Turrigiano, 2013). Photoreceptors possess ribbon synapses which support fast, synchronous vesicle release, enhancing the temporal precision of signal transmission. The proximity of the postsynaptic bipolar cell receptors to these release sites is highly indicative of their functional relationship: sites in close proximity (20–400 nm) typically express fast receptor isoforms which desensitize and recover very rapidly, permitting the detection of transient signals, while those further away (200–1800 nm) express slower isoforms which desensitize equally quickly, but recover more slowly, rendering them more sensitive to gradual changes (Rao-Mirotnik *et al.* 1998; DeVries *et al.* 2006; Sterling & Laughlin, 2015). It has been suggested that receptor saturation may also play a role in supporting the transmission of high frequency signals, reducing the dynamic range of the bipolar cell input while increasing its sensitivity to low levels of vesicle release, effectively counteracting the depletion of vesicles at the photoreceptor synapse (Grabner *et al.* 2016).

Of further interest is the horizontal cell, which is a central part of the circuitry underlying lateral inhibition in the OPL (Thoreson & Mangel, 2012). Horizontal cells densely contact cone photoreceptors across their dendritic arbour, invaginating with fine processes which terminate within 20 nm of the release sites (Haverkamp *et al.* 2001). These cells integrate over the signals from the photoreceptors, computing the ambient light level and subtracting this from the photoreceptor output. Diverse feedback mechanisms operating through hemichannel-based ephaptic feedback, pH changes in the synaptic cleft and GABA autoreception modulate the effect of ambient light levels and contrast on the cone signal dynamics (Liu *et al.* 2013; Kemmler *et al.* 2014). Although many aspects of their general role in shaping signal transmission at the photoreceptor-to-BC synapse are understood on this functional level, the horizontal cell is conspicuously absent from most functional models of the mammalian retina. How horizontal cells shape the response dynamics of their bipolar cell partners in a circuit-wide context is

still poorly understood. Indeed, it is not known to what extent horizontal cells selectively contact different bipolar cell types, or how these contacts are structured on a fine anatomical level (see also accompanying review in this issue by Chapot, Euler and Schubert).

Modern techniques such as labelling synaptic structures using genetically encoded biosensors (Dreosti & Lagnado, 2011; Song & Knöpfel, 2016) and super-resolution microscopy (Lu *et al.* 2013) could be used to develop a quantitative structural atlas based on synaptic features, perhaps also incorporating the features of proximal non-contacting dendrites which might, by some non-classical pathway, be functionally linked (DeVries *et al.* 2006; Herr *et al.* 2011; Szmajda & DeVries, 2011). In future, the application of such a combined approach to photoreceptor synapses could assess the prevalence and role of these synaptic motifs, exploring modes of convergence and divergence (Wässle, 2004), non-linear signalling properties (Field & Rieke, 2002; Berntson *et al.* 2004; Taylor & Smith, 2004), specificity of subsynaptic structures (MacGillavry *et al.* 2013; Perez de Arce *et al.* 2015), synaptic scaling (Turrigiano, 2011), and local and global reciprocal feedback.

A final, promising route for capturing fine-grain sub-cellular circuit dynamics is through biophysical modelling. Electron microscopy studies provide detailed knowledge about the structure of the photoreceptor-to-BC synapse, with precise renderings of the synaptic volumes, including the varying thickness along dendritic and axonal branches which may be critical for local processing. Additionally, large datasets provide multiple morphologies for each cell type, making it possible to distinguish features that are robustly conserved from cell-to-cell variability. Together with the active membrane properties, based on already described receptors and channels, this information could be used to generate a model of the complex synaptic architecture below a single photoreceptor axon terminal. If the challenges involved in setting up such complex models and constraining their parameters can be met (see e.g. O'Leary & Marder, 2016), such modelling could bring together the somewhat disparate threads of functional and anatomical research, yielding insight into the many factors that shape the activity at the very beginning of the visual system.

References

- Anderson JR, Jones BW, Watt CB, Shaw MV, Yang JH, Demill D & Marc RE (2011). Exploring the retinal connectome. *Mol Vis* **17**, 355–379.
- Asteriti S, Gargini C & Cangiano L (2014). Mouse rods signal through gap junctions with cones. *eLife* **3**, e01386.
- Baden T, Berens P, Franke K, Román Rosón M, Bethge M & Euler T (2016). The functional diversity of retinal ganglion cells in the mouse. *Nature* **529**, 345–350.

- Baden T, Schubert T, Chang L, Wei T, Zaichuk M, Wissinger B & Euler T (2013). A tale of two retinal domains: Near-optimal sampling of achromatic contrasts in natural scenes through asymmetric photoreceptor distribution. *Neuron* **80**, 1206–1217.
- Behrens C, Schubert T, Haverkamp S, Euler T & Berens P (2016). Connectivity map of bipolar cells and photoreceptors in the mouse retina. *eLife* **5**, e20041.
- Bertson A, Smith RG & Taylor WR (2004). Transmission of single photon signals through a binary synapse in the mammalian retina. *Vis Neurosci* **21**, 693–702.
- Breuninger T, Puller C, Haverkamp S & Euler T (2011). Chromatic bipolar cell pathways in the mouse retina. *J Neurosci* **31**, 6504–6517.
- Briggman KL, Helmstaedter M & Denk W (2011). Wiring specificity in the direction-selectivity circuit of the retina. *Nature* **471**, 183–188.
- Demb JB & Singer JH (2012). Intrinsic properties and functional circuitry of the AII amacrine cell. *Vis Neurosci* **29**, 51–60.
- Denk W, Briggman KL & Helmstaedter M (2012). Structural neurobiology: missing link to a mechanistic understanding of neural computation. *Nat Rev Neurosci* **13**, 351–358.
- DeVries SH, Li W & Saszik S (2006). Parallel processing in two transmitter microenvironments at the Cone Photoreceptor Synapse. *Neuron* **50**, 735–748.
- Ding H, Smith RG, Polog-Polsky A, Diamond JS & Briggman KL (2016). Species-specific wiring for direction selectivity in the mammalian retina. *Nature* **535**, 105–110.
- Dreosti E & Lagnado L (2011). Optical reporters of synaptic activity in neural circuits. *Exp Physiol* **96**, 4–12.
- Euler T, Haverkamp S, Schubert T & Baden T (2014). Retinal bipolar cells: elementary building blocks of vision. *Nat Rev Neurosci* **15**, 507–519.
- Field GD & Rieke F (2002). Nonlinear signal transfer from mouse rods to bipolar cells and implications for visual sensitivity. *Neuron* **34**, 773–785.
- Grabner CP, Ratliff CP, Light AC & DeVries SH (2016). Mechanism of high-frequency signaling at a depressing ribbon synapse. *Neuron* **91**, 133–145.
- Greene MJ, Kim JS & Seung HS (2016). Analogous convergence of sustained and transient inputs in parallel on and off pathways for retinal motion computation. *Cell Rep* **14**, 1892–1900.
- Haverkamp S, Grünert U & Wässle H (2001). The synaptic architecture of AMPA receptors at the cone pedicle of the primate retina. *J Neurosci* **21**, 2488–2500.
- Haverkamp S & Wässle H (2000). Immunocytochemical analysis of the mouse retina. *J Comp Neurol* **23**, 1–23.
- Haverkamp S, Wässle H, Duebel J, Kuner T, Augustine GJ, Feng G & Euler T (2005). The primordial, blue-cone color system of the mouse retina. *J Neurosci* **25**, 5438–5445.
- Helmstaedter M (2013). Cellular-resolution connectomics: challenges of dense neural circuit reconstruction. *Nat Methods* **10**, 501–507.
- Helmstaedter M, Briggman KL & Denk W (2011). High-accuracy neurite reconstruction for high-throughput neuroanatomy. *Nat Neurosci* **14**, 1081–1088.
- Helmstaedter M, Briggman KL, Turaga SC, Jain V, Seung HS & Denk W (2013). Connectomic reconstruction of the inner plexiform layer in the mouse retina. *Nature* **500**, 168–174.
- Herr S, Ngo IT, Huang TM, Klug K, Sterling P & Schein S (2011). Cone synapses in macaque fovea: II. Dendrites of OFF midget bipolar cells exhibit inner densities similar to their outer synaptic densities in basal contacts with cone terminals. *Vis Neurosci* **28**, 17–28.
- Ichinose T, Fyk-Kolodziej B & Cohn J (2014). Roles of ON cone bipolar cell subtypes in temporal coding in the mouse retina. *J Neurosci* **34**, 8761–8771.
- Kemmler R, Schultz K, Dedek K, Euler T & Schubert T (2014). Differential regulation of cone calcium signals by different horizontal cell feedback mechanisms in the mouse retina. *J Neurosci* **34**, 11826–11843.
- Kim JS, Greene MJ, Zlateski A, Lee K, Richardson M, Turaga SC, Purcaro M, Balkam M, Robinson A, Behabadi BF, Campos M, Denk W, Seung HS & Eyewirers (2014). Space-time wiring specificity supports direction selectivity in the retina. *Nature* **509**, 331–336.
- Kramer RH & Davenport CM (2015). Lateral inhibition in the vertebrate retina: The case of the missing neurotransmitter. *PLoS Biol* **13**, e1002322.
- Lambo ME & Turrigiano GG (2013). Synaptic and intrinsic homeostatic mechanisms cooperate to increase L2/3 pyramidal neuron excitability during a late phase of critical period plasticity. *J Neurosci* **33**, 8810–8819.
- Lauritzen JS, Sigulinsky CL, Anderson JR, Kalloniatis M, Nelson NT, Emrich DP, Rapp C, McCarthy N, Kerzner E, Meyer M, Jones BW & Marc RE (2017). Rod-cone crossover connectome of mammalian bipolar cells. *J Comp Neurol* (in press; doi: 10.1002/cne.24084).
- Lee SCS, Meyer A, Schubert T, Hüser L, Dedek K & Haverkamp S (2015). Morphology and connectivity of the small bistratified A8 amacrine cell in the mouse retina. *J Comp Neurol* **523**, 1529–1547.
- Li W, Chen S & DeVries SH (2010). A fast rod photoreceptor signaling pathway in the mammalian retina. *Nat Neurosci* **13**, 414–416.
- Liu X, Hirano A, Sun X, Brecha NC & Barnes S (2013). Calcium channels in rat horizontal cells regulate feedback inhibition of photoreceptors through an unconventional GABA- and pH-sensitive mechanism. *J Physiol* **591**, 3309–3324.
- Lu RW, Wang BQ, Zhang QX & Yao XC (2013). Super-resolution scanning laser microscopy through virtually structured detection. *Biomed Opt Express* **4**, 1673–1682.
- MacGillavry HD, Song Y, Raghavachari S & Blanpied TA (2013). Nanoscale scaffolding domains within the postsynaptic density concentrate synaptic AMPA receptors. *Neuron* **78**, 615–622.
- Mills SL, Tian LM, Hoshi H, Whitaker CM & Massey SC (2014). Three distinct blue-green color pathways in a mammalian retina. *J Neurosci* **34**, 1760–1768.
- Morgan JL & Lichtman JW (2013). Why not connectomics? *Nat Methods* **10**, 494–500.

- Okawa H & Sampath AP (2007). Optimization of single-photon response transmission at the rod-to-rod bipolar synapse. *Physiology (Bethesda)* **22**, 279–286.
- O’Leary T & Marder E (2016). Temperature-robust neural function from activity-dependent ion channel regulation. *Curr Biol* **26**, 2935–2941.
- Pang JJ, Gao F, Lem J, Bramblett DE, Paul DL & Wu SM (2010). Direct rod input to cone BCs and direct cone input to rod BCs challenge the traditional view of mammalian BC circuitry. *Proc Natl Acad Sci USA* **107**, 395–400.
- Perez de Arce K, Schrod N, Metzbowler SWR, Allgeyer E, Kong GKW, Tang AH, Krupp AJ, Stein V, Liu X, Bewersdorf J, Blanpied T, Lucic V & Biederer T (2015). Topographic mapping of the synaptic cleft into adhesive nanodomains. *Neuron* **88**, 1165–1172.
- Protti DA, Flores-Herr N, Li W, Massey SC & Wässle H (2005). Light signaling in scotopic conditions in the rabbit, mouse and rat retina: a physiological and anatomical study. *J Neurophysiol* **93**, 3479–3488.
- Rao-Mirotznik R, Buchsbaum G & Sterling P (1998). Transmitter concentration at a three-dimensional synapse. *J Neurophysiol* **80**, 3163–3172.
- Song C & Knöpfel T (2016). Optogenetics enlightens neuroscience drug discovery. *Nat Rev Drug Discov* **15**, 97–109.
- Staffler B, Berning M, Boergens KM, Gour A, van der Smagt P & Helmstaedter M (2017). SynEM: Automated synapse detection for connectomics. *Neuron* **87**, 1193–1206.
- Sterling P & Laughlin S (2015). *Principles of Neural Design*. MIT Press, Cambridge, MA, USA.
- Szikra T, Trenholm S, Drinnenberg A, Jüttner J, Raics Z, Farrow K, Biel M, Awatramani G, Clark DA, Sahel JA, da Silveira RA & Roska B (2014). Rods in daylight act as relay cells for cone-driven horizontal cell-mediated surround inhibition. *Nat Neurosci* **17**, 1728–1735.
- Szmajda BA & DeVries SH (2011). Glutamate spillover between mammalian cone photoreceptors. *J Neurosci* **31**, 13431–13441.
- Taylor WR & Smith RG (2004). Transmission of scotopic signals from the rod to rod-bipolar cell in the mammalian retina. *Vision Res* **44**, 3269–3276.
- Thoreson WB & Mangel SC (2012). Lateral interactions in the outer retina. *Prog Retin Eye Res* **100**, 130–134.
- Tsukamoto Y, Morigiwa K, Ishii M, Takao M, Iwatsuki K, Nakanishi S & Fukuda Y (2007). A novel connection between rods and ON cone bipolar cells revealed by ectopic metabotropic glutamate receptor 7 (mGluR7) in mGluR6-deficient mouse retinas. *J Neurosci* **27**, 6261–6267.
- Tsukamoto Y, Morigiwa K, Ueda M & Sterling P (2001). Microcircuits for night vision in mouse retina. *J Neurosci* **21**, 8616–8623.
- Tsukamoto Y & Omi N (2014). Some OFF bipolar cell types make contact with both rods and cones in macaque and mouse retinas. *Front Neuroanat* **8**, 105.
- Turrigiano G (2011). Too many cooks? Intrinsic and synaptic homeostatic mechanisms in cortical circuit refinement. *Annu Rev Neurosci* **34**, 89–103.
- Vroman R, Klaassen LJ & Kamermans M (2013). Ephaptic communication in the vertebrate retina. *Front Hum Neurosci* **7**, 612.
- Wässle H (2004). Parallel processing in the mammalian retina. *Nat Rev Neurosci* **5**, 747–757.

Additional information

Competing interests

None declared.

Author contributions

All authors have approved the final version of the manuscript and agree to be accountable for all aspects of the work. All persons designated as authors qualify for authorship, and all those who qualify for authorship are listed.

Funding

The authors have received the following funding. Deutsche Forschungsgemeinschaft (DFG): T.E., T.S., EXC 307; Bernstein Center for Computational Neuroscience Tübingen: P.B., FKZ 01GQ1002; Deutsche Forschungsgemeinschaft (DFG): P.B., BE 5601/1-1; Bernstein Center for Computational Neuroscience Tübingen and the German Ministry of Science and Education (BMBF) through the Bernstein Award to PB (FKZ: 01GQ1601).

Horizontal cells use different synaptic sites for global and local signaling

Christian Behrens¹⁻⁴, Yue Zhang^{1,2,4}, Shubhash Chandra Yadav⁵, Silke Haverkamp⁶, Stephan Irsen⁷, Maria M. Korympidou^{1,2,4}, Anna Schaedler^{1,2,4}, Karin Dedek⁵, Robert G. Smith⁸, Thomas Euler¹⁻³, Philipp Berens^{1-3,9}, Timm Schubert^{1,2}

¹*Institute for Ophthalmic Research, University of Tübingen, 72076 Tübingen, Germany*

²*Center for Integrative Neuroscience, University of Tübingen, 72076 Tübingen, Germany*

³*Bernstein Center for Computational Neuroscience, University of Tübingen, 72076 Tübingen, Germany*

⁴*Graduate Training Centre of Neuroscience, University of Tübingen, 72076 Tübingen, Germany*

⁵*Institute for Biology and Environmental Sciences, Research Center Neurosensory Science, University of Oldenburg, 26111 Oldenburg, Germany*

⁶*Department of Computational Neuroethology, Center of Advanced European Studies and Research (caesar), 53175 Bonn, Germany*

⁷*Department of Electron Microscopy and Analytics, Center of Advanced European Studies and Research (caesar), 53175 Bonn, Germany*

⁸*Department of Neuroscience, University of Pennsylvania, Philadelphia, PA 19104, USA*

⁹*Department of Computer Science, University of Tübingen, 72076 Tübingen, Germany*

Abstract

In the outer plexiform layer of the mouse retina, two types of cone photoreceptors (cones) provide input to more than a dozen types of cone bipolar cells (CBC). This vertical signal transfer is modulated by laterally oriented horizontal cells (HCs) that represent the only type of interneuron in the outer retina. Horizontal cells form feedback synapses with cones and feedforward synapses with BCs. However, the exact computational role of HCs is still unclear. Apart from performing global lateral signaling within their laterally organized network, HCs also provide local, cone-specific feedback. However, it has been not clear, which synaptic structures HCs use to provide both local feedback to cone and global tasks, lateral forward signaling to BCs.

Here, we used a serial block-face electron microscopy volume in which we reconstructed the dendritic trees of five HCs as well as cone axon terminals and bipolar cells and quantitatively analyzed their connectivity. Apart from the already fine varicosities invaginating into cone axon terminals, we identified “bulbs”, short segments of increased dendritic diameter on the primary dendrites of the horizontal cells. These structures are located clearly below the cone axon terminal base and make contact to other cells mostly identified as other HCs or CBCs. Immunolabeling showed evidence for GABA receptor gamma2 subunits related to horizontal cell structures in this depth. Together, this suggests a second synaptic stratum in the outer plexiform layer exists that may underlie global feedforward signaling to BCs whereas the fine varicosities provide local, cone-specific feedback. A biophysical model of a HC dendritic branch confirms the hypothesis that HCs provide global feedforward input at the bulb structures to BCs while providing localized feedback to cones at their fine dendritic tips.

Introduction

Interneurons show a remarkable heterogeneity and diversity in both function and morphology in all parts of the brain (Cardin 2018). As for neurons in general, it is thought that the morphology of an interneuron reflects its function. In the retina, for instance, bipolar cells relay signals from the outer to the inner synaptic layer, whereas wide-field amacrine cells usually relay information laterally across the retina (reviewed in Euler et al. 2014; Masland 2012). However, morphology can be deceiving; for example, the very symmetric starburst amacrine cells in the mammalian retina compute the direction of image motion (Taylor and Smith 2012). Moreover, interneurons were shown to serve more than one functional role but rather sequentially in a context-dependent manner. The common AII amacrine cells for example are at the heart of rod vision in low light conditions while they change role and contribute to approach sensitivity under photopic conditions (Münch et al. 2009). Here, we show that horizontal cells in the retina may provide distinct functions in parallel at different highly specialized synapses.

At the very first synapse of the mouse visual system the signal from the light-sensitive cone photoreceptors (cones) is relayed to second order neurons: Each cone axon terminal has more than 10 largely independent output sites, contacting a sample of the 13 types of cone bipolar cells (Behrens et al. 2016), which relay the signal vertically to retinal output neurons. In complement, the laterally-organized horizontal cells modulate the complex photoreceptor-bipolar cell synapse (Fig. 1A; Haverkamp, Grünert, and Wässle 2000). ON-cone bipolar cell dendrites invaginate into the cone axon terminals to contact an individual output site and form a triad with HC dendritic processes, whose distal dendritic tips invaginate the synaptic cleft flanking ON-cone bipolar cell dendrites. In contrast, OFF-cone bipolar cell dendrites contact the cone axon terminal base not forming contacts with HCs.

Horizontal cells play a major role in global visual processing and contribute to contrast enhancement and generation of center-surround receptive fields, providing global feedback signals (Thoreson and Mangel 2012; Drinnenberg et al. 2018). Moreover, recent functional measurements indicate that horizontal cells can provide local feedback to photoreceptors (Chapot, Euler, and Schubert 2017), modulating each cone's output individually. However, it is unclear how this local feedback can be reconciled with the HC's traditional role of providing global feedback. In addition, despite our knowledge of the complex interplay of different synaptic mechanisms underlying horizontal cell feedback (Kemmler et al. 2014; Liu et al. 2013; Vroman et al. 2014), a quantitative anatomical picture of outer retinal connectivity with the horizontal cell as a central player is missing.

Here, we make use of the serial block face electron microscopy dataset e2006 (Helmstaedter et al. 2013; Behrens et al. 2016) to reconstruct the mouse outer retina with a focus on horizontal cell circuitry and identify the connectivity motifs made between horizontal cells and other neuron types. In addition to the invaginating contacts between cones and HCs in the cone axon terminal, we identified – at the level of primary HC dendrites – putative GABAergic synaptic sites among HCs as well as between HCs and bipolar cells as suggested before (Yang and Wu 1991; Duebel et al. 2006). Based on

biophysical models of HC signaling, we propose that the role of this putative second synaptic site in HCs is to provide global signals in the form of GABAergic input to postsynaptic bipolar cells. This suggests that a single interneuron can simultaneously provide local reciprocal feedback and global feedforward signals.

Results

Reconstruction of horizontal cells and connectivity with cone photoreceptors

Using the publicly available serial block-face electron microscopy dataset e2006 (Helmstaedter et al., 2013, Fig. 1B), we reconstructed five complete dendritic arbors of HCs in the outer mouse retina (Fig. 1C,D). We analyzed the contacts of all three classes of neurons in the outer retina – cones, bipolar cells and HCs (Helmstaedter et al. 2013; Behrens et al. 2016) – to gain a complete picture of outer retinal connectivity. The reconstructed HCs had a dendritic area of $4.200 \pm 400 \mu\text{m}^2$ with 4 to 6 primary dendrites leaving the soma ($n=5$ HCs) and extended fine dendritic varicosities towards cone axon terminals (Fig. 1 E). Each HC contacted on average 59 ± 5 (between 47 and 76) cones within its dendritic field, all cones within reach of the horizontal cells' dendrites (Fig. 2A). Remarkably, the number of fine HC tips contacting an individual cone was larger towards the horizontal cell soma and smaller for more peripheral contacts (Fig. 2B, C). To analyze the contact area between cones in direct proximity of a horizontal cell soma and cones contacted in the periphery of the horizontal cell dendritic field, we quantified the contacting area of volume-rendered cone axon terminals and all horizontal dendritic tips (Fig. 2D). The contact area between an individual HC and cones strongly decreased towards the periphery, suggesting that the synaptic interaction is largest for cones in close neighborhood to the horizontal cell soma.

Invaginating contacts between cones, ON-cone bipolar cells and horizontal cells

The invaginating synapse at the cone pedicel as a site of contacts between horizontal cells and different types ON-cone bipolar cells has never been quantitatively investigated in detail. In a previous study, we found that some types such as CBC5T, 5O, 8 and X sampled sparsely from the cones (Fig. 2E). In addition, the type X ON-cone bipolar cell makes rather small and basal but not “typical” invaginating contacts at the cone axon terminal resembling more an OFF-cone bipolar cell contact (Behrens et al. 2016). If these bipolar cell types contacted cones more sparsely, the number of contacts with the invaginating horizontal cell dendrites should be lower as well. We checked all ON-CBC contacts ($n=36$) on five central cones and could identify one or two contacting HC dendritic tips per ON-CBC tip, implying that the number of contacts between HC and ON-CBCs matches the number of cone contacts per CBC. This implicates that the number of contacts between horizontal cells and BC types CBC5T, 5O, 8 and X within the cone axon terminal is lower than for the other ON-cone bipolar cell types (Fig. 2F). Moreover, comparing the contact height of a non-invaginating CBCX and the invaginating S-cone-selective CBC9 shows that most contacts between horizontal cells and CBCX are

at the level of the cone axon terminal whereas the CBC9 contacts are deeper in the invaginating cleft (Fig. 2G). Thus, the connectivity between ON-cone bipolar cells and horizontal cells in the synaptic cleft follows the general contact motif pattern between cones and ON-cone bipolar cells.

Non-invaginating (bulb) contacts between horizontal cells and bipolar cells

Signal transfer at the cone-to-bipolar cell synapse can be modulated in two ways: First, horizontal cell feedback can modulate the cones' glutamate release directly within the invaginating cleft (Kamerlings et al. 2001) which would affect ON- and OFF-cone bipolar cells in a similar way. This type of feedback has been shown to be highly localized to individual cones (Chapot et al. 2017), thus it is unlikely that this pathway is responsible for global feedback signals traditionally suggested for HCs (Thoreson and Mangel 2012). Second, horizontal cells may provide direct synaptic input to bipolar cell dendrites independent from the invaginating cleft, possibly providing a route for global inhibitory signals to be relayed. A synaptic site for this latter mechanism has not been identified so far.

To test this idea, we systematically examined the five volume-rendered horizontal cells and found regularly distributed, dendritic swellings along the primary dendrites (Fig. 3A, B). These dendritic swellings (bulbs) showed a marked increase in dendritic diameter (Fig. 3C). Almost all bulbs were located clearly below the cone axon terminal base but not in direct contact with it (Fig. 3D). In contrast to invaginating dendritic tips that show a higher density towards the soma of the HC, the bulbs were more evenly distributed along the primary dendrites (Fig. 3E).

Most of the identified bulbs contacted either bulbs of other volume-rendered horizontal cells (72 out of 554, Fig. 4A) or dendrites of ON- and OFF-cone bipolar cells (224 out of 554; Fig. 4B) or both (67), suggesting that the bulb structures may represent HC-HC and/or HC-BC synapses. For the remaining 189 bulbs, we had no information about the identity of the contacted cells. As nearly all BCs in the field were traced, but only five HCs, these contacts may well represent contacts to other HCs.

Interestingly, we found a difference in bulb-level connectivity between HCs and OFF- and ON cone bipolar cells: While except for type 5T, the majority of ON-CBCs contacted HCs at the bulb site, all OFF-CBC types but 3A make considerably less contacts (Fig.4C). However, the overall number of contacts per BC is expected to be higher since contacts to unreconstructed HCs which reach only partially into the dataset are missing. Furthermore, our quantification shows that the number of BCs contacted at bulbs per HC was lowest for the CBC types 8, 9, X and 5T and highest for CBC6 and 7 (Fig. 4D). For types 8, 9 and X, the low numbers likely originate in their lower cell count while for 5T it is a consequence of the low number of contacts per BC. Comparing the bulb-to-ON-CBC contacts with the cone-to-ON-CBC contacts taken from Behrens et al (2016) (Fig. 4E) showed that both connectivity patterns are almost identical for nearly all bipolar cell types: Interestingly, the only striking difference was found for the type 5O bipolar cells. This cell type samples from very few cones but establishes strong contacts with bulbs. Thus, while the three CBC5 types do not differ much in

dendritic field size, axon terminal size and stratification depth, they can be distinguished based on their connectivity pattern in the outer retina.

Pre- and postsynaptic proteins at horizontal cell dendrites

If the bulbs identified on primary dendrites of volume-rendered horizontal cells indeed form presynaptic sites, we would expect presynaptic proteins in bulb-like HC structures. In horizontal cells, several presynaptic proteins such as SNAP25 mediating vesicular transmitter release have been found (Hirano et al. 2011). However, most of these immunolabeling experiments have not been conducted with an emphasis on primary dendritic expression of these proteins, rather focusing on the distal tips. We therefore aimed at identifying presynaptic sites in HCs using calbindin antibodies for HCs and SNAP25 for visualizing presynaptic regions in HCs (Fig. 5A). Indeed, we found intense SNAP25 staining in thickened dendritic sites at the same depth at which bulbs were found in the EM data. Since the calbindin labeling does not reveal individual bulbs but rather likely aggregations we cannot directly conclude that the SNAP25 labeling is located directly at the bulb. However, in any case, the presynaptic marker SNAP25 is expressed not only at fine varicosity tips but also on swellings along the primary HC dendrites.

If bulbs contained GABAergic synapses between HCs, GABA receptors should be present. In the mouse retina, different GABA receptor subunits are expressed in the outer retina. A dashed band of $\alpha 1$ subunit GABA receptors can be seen at the level of the cone axon terminals (Haverkamp and Wässle 2000) indicating that $\alpha 1$ subunits are prominently expressed by HC dendrites invaginating in the synaptic cleft (Kemmler et al. 2014). $\gamma 2$ subunits have a broader expression profile (Haverkamp and Wässle 2000) that clearly stratifies below the cone axon terminals. We therefore asked whether $\gamma 2$ GABA receptors are expressed close to bulbs on primary horizontal cell dendrites. To this end, we injected HCs with the fluorescent dye Alexa Fluor 568 and performed GABA receptor labeling for these individual horizontal cells (Fig. 5B, C). $\gamma 2$ subunit immunoreactivity is strong at the level of primary dendrites, which confirms the presence of synaptic sites and GABA release deeper in the OPL and not only at cone axon terminals. All identified bulbs (n=30 in 3 horizontal cells) revealed immunolabeling for $\gamma 2$ GABA receptors, indicating that they may provide or receive GABAergic input (Fig. 5C).

Horizontal cell bulbs are putative synaptic structures

The selective connectivity of bulbs with HCs or BCs as well as the observed GABA receptor distribution suggest that bulbs may indeed be presynaptic elements. For further evidence that the receptors bulbs may be synaptic structures, we performed focused ion beam scanning electron microscopy (EM) and reconstructed horizontal cells from their dendritic tips in the invaginating cleft (Fig. 5D) to the depth in the OPL where bulbs are located. In the EM images, bulbs could be easily identified base on their thickened structure (Fig. 5D, middle left). These structures contained

mitochondria as well as putative vesicles (Fig. 5D, middle right). However, compared with the vesicles in the cone axon terminal (Fig. 5D, far right), those vesicles in the bulbs were low in number and only faintly labeled as described before (Dowling and Boycott 1966). This supports the idea that horizontal cell bulbs form (likely GABAergic) synaptic contacts with other horizontal cells and/or cone bipolar cells.

Biophysical modelling indicates potential bulb function

To study the potential functional role of HC bulb contacts, we built a biophysical model of a HC dendritic branch with cone input (Fig. 6A, B; based on the model of Chapot, Behrens, et al., 2017). We stimulated the cones in the model with both full-field and checkerboard noise for spatially correlated and uncorrelated input and measured voltage and Ca^{2+} signals in the HC dendritic tips invaginating into cone axon terminals and in the bulb structures (Fig. 6C, D). For the full-field stimuli, we find high correlations between voltage signals from all recording points (0.85 ± 0.10). Due to vesicle release noise in the model which occurs independently at each synapse between cones and HC tips, correlations between signals in different tips (0.73 ± 0.07) and between signals in tips and bulbs (0.84 ± 0.06) are lower than those between signals in bulbs (0.94 ± 0.04) (Fig. 6E). However, correlations between bulbs and the average over the tip signals (0.97 ± 0.02) are at a similar level as the correlations between bulbs.

For the checkerboard noise, which is a spatially uncorrelated stimulus, this was different: The average correlation between voltage signals in tips was rather low (0.25 ± 0.14), confirming our previous results (Chapot et al. 2017). In contrast, the average correlation between voltage signals in bulbs was higher (0.71 ± 0.19) and they also show a high correlation of 0.80 ± 0.10 with the average over the signals in the tips. Together, this indicates that for spatially correlated stimulation the noise present at the level of individual tips is averaged out at bulb-level while for spatially uncorrelated stimulation the global component of the stimulus dominates the signal at the level of the bulbs.

Discussion

Here, we provide a quantitative picture of outer retina connectivity including HCs and describe a new putative type of synaptic site in retinal horizontal cells of the mouse retina. In contrast to the well-described feedback synapse that modulates the cone photoreceptor output this putative synapse is likely a feedforward or reciprocal synapse that provides GABAergic drive to other horizontal cells as well as to bipolar cells. On the functional level, this synaptic site likely ingrates the local signals from numerous cone photoreceptors, generates a global output signal and provides the basis for a global center-surround organization in the outer retina. Thus, retinal HCs are an example of interneurons that use two structurally distinct synaptic sites to provide both local synaptic feedback to their input neurons and global feedforward input to postsynaptic neurons.

Are horizontal cell bulbs synaptic structures?

Although direct synaptic connections between horizontal cells and bipolar cells have been suggested for a long time (Duebel et al. 2006), they have never been investigated in detail. One reason may be the lack of an adequate methodological approach facilitating a quantitative analysis of synaptic contacts. Here, we used the e2006 EM data set that was initially used to describe inner retinal connections (Helmstaedter et al., 2013) as well as photoreceptor-to-bipolar cell synapses (Behrens et al., 2016). In complement, to demonstrate that analyzed structures might indeed be synaptic sites, we employed another EM 3D stack in which organelles typically found in presynaptic sites are preserved. The finding that both mitochondria as well as putative vesicles are present in the bulbs suggests that these structures are presynaptic structures.

At the immunolabeling level, the distribution of gamma2 subunits of GABA_A receptors on bulbs indicates that GABA receptors are expressed in close proximity to the bulbs. However, here it is still unclear on which retinal cell type(s) these GABA receptors are expressed. Since bulbs contact other bulbs of horizontal cells as well as bipolar cell dendrites, we expect that bulbs represent a general output site to postsynaptic cells.

In this context, one open question is whether bulbs may not only be presynaptic sites but also presynaptic sites. Regarding the fact that bulbs contact each other it is conceivable that they establish GABAergic synapses between them. We cannot exclude the possibility that bulbs receive glutamatergic input by diffusion from the photoreceptor – like OFF-cone bipolar cells – however, the lack of GluR4 glutamate receptors at the bulb level argues against this possibility. Hence, we propose that GABA release at the bulbs results from electric propagation along the dendrites of the horizontal cells rather than being transmitted via diffusing glutamate.

Local and global synapses in a single retina interneuron

Recently, local signaling has been prominently featured in the discussion about the function of horizontal cells (Jackman et al. 2011; Chapot et al. 2017). On the other hand, horizontal cells are involved in global signal integration (Drinnenberg et al. 2018). However, how a laterally organized and strongly electrically coupled syncytium of a single type of interneuron can perform both local and global tasks, has remained unclear. For example, it has remained open, how lateral inhibition essential for center-surround organization in the outer retina can be generated by fine structures as the horizontal cell varicosities invaginating into the cone axon terminal (Yang and Wu 1991). A recent study suggested that these structures based on their thin diameter and high resistance are optimized for generation of local cone-specific feedback and to an lesser extent for lateral propagation of electrical signals (Chapot et al. 2017). With the here described new putative synaptic sites between horizontal cells and bipolar cells, we solve this long existing dilemma and propose – for the first time – an interneuron with two functional specializations: local feedback and global feedforward synapses.

Since synaptic function is not only determined by the specificity of the involved pre- and postsynaptic components but also depends on the dendritic architecture carrying the synapse, the requirements of local and global synapses are seemingly different: Thin, high resistance distal dendrites for local signaling and wider, low resistance proximal dendrites for more global synapses. Indeed, our modeling suggests that the incoming signals from individually activated cone photoreceptors are strongly attenuated towards the more proximal dendrites. Only under simultaneous activation of multiple cones the signal is summed up in the proximal dendrites and can easily be converted into a GABAergic output signal.

Selective connectivity with ON-cone bipolar cell types as a mechanism of synaptic scaling?

As previously reported, some ON-cone bipolar cells contact cone axon terminals in a very specific manner. For example, the CBCX, 8, 9, 5T and 5O contact considerably less cones than expected from their relatively large dendritic field whereas other types such as types 5I, 6 and 7 contact almost as many cones as located in the dendritic field (Behrens et al., 2017). Remarkably, this connectivity is also reflected in the number of bulbs connected by ON-cone bipolar cells: Types X, 9 and 5T contact less bulbs than the other types while type 8 contacts only slightly more bulbs than other cells despite its significantly larger dendritic field. This correlation of excitatory and inhibitory synapse number may be a form of synaptic scaling (Turrigiano 2011) that could have an effect on the organization of the receptive field of bipolar cells. The center of a receptive field is defined as the region that is driven by direct glutamatergic input from cones whereas the surround is formed by the lateral inhibition by interneurons in the periphery. A balanced synaptic weight between center and surround activation may support that the bipolar cell's ability to stay within its operational range.

The only exception is the bipolar cell type 5O; this one establishes only few contacts with cones but has relatively many bulb contacts which is in strong contrast to the types 5T and 5I which make little and many contacts to cones and horizontal cell bulbs, respectively. Based on their morphology and their stratification depth in the inner plexiform layer, these three bipolar cell types are very hard to distinguish. However, they differ in their connectivity with cones and horizontal cells in the outer retina, and thus, may be functionally distinct (Franke et al. 2017). Whether the size and efficiency of synaptic contacts is different and whether or how synaptic scaling plays a role in type 5T cells, or whether the cells of this type receive a stronger inhibitory surround in the outer retina has to be addressed in a functional study.

The horizontal cell – an interneuron with multiple functions

Multiple functions implemented by a single neuron have only been demonstrated for few interneuron types. For example, in the wealth of functionally distinct amacrine cell types and their synaptic connections in the inner retina it is hardly feasible to attribute for example local and global function to a specific amacrine cell type. However, for some better investigated amacrine cell types such as the

AII or starburst amacrine cells the functions as well as the underlying circuit are clear (Demb and Singer 2012; Taylor and Smith 2012). For some others such as the A17 amacrine cells (Hartveit 1999) forming reciprocal synapses with rod bipolar cells a functional switch between local and more global processing has been suggested (Schubert and Euler 2010). In any case, here, the synaptic site would be identical. Therefore, the finding of multiple functions within one type of interneuron is not surprising. More intriguing is our finding that different synaptic performances such as feedforward and feedback signaling are apparently performed at different synaptic sites as previously shown for an amacrine cell type that provides excitatory and inhibitory drive at distinct synaptic sites (Lee et al. 2016; Tien, Kim, and Kerschensteiner 2016).

A crucial question is why these two synaptic tasks are performed in the same interneuron. In the inner retina distinct amacrine cell types appear mostly to be responsible for different computational tasks. Why is this motif not implemented in the outer retina? Two possible explanations may play a role here: First, the cone axon terminal system is among the most complex synaptic structures in the brain. Therefore, integrating another interneuron type during evolution might have been avoided for the sake of space limitation and circuitry simplification. The hypothesis is supported by the fact that also the reciprocal feedback synapses are not provided by an additional interneuron type but by an intraretinal axon terminal system of horizontal cells. Second, because of the shared cone input but spatial separation of local feedback and global feedforward output synapses both synaptic systems can employ the same input signals and use the (more or less independently generated) output signal to modulate activity of different sets of postsynaptic neurons in the outer retinal circuitry.

Methods

Dataset

Our analysis is based on the SBEM dataset e2006 published by Helmstaedter et al, 2013 (<http://www.neuro.mpg.de/connectomics>). The dataset covers a piece of retina of 80 μm x 114 μm x 132 μm with a resolution of 25 x 16.5 x 16.5 nm. We identified the somata of 15 horizontal cells and skeletonized the dendrites of the five central HC in KNOSSOS (Helmstaedter, Briggman, and Denk 2011, www.knossostool.org). We used algorithms published with the dataset to reconstruct the volumes of HCs, BCs and cone pedicles in the OPL and to identify their contacts (for details see Behrens et al. 2016).

We manually identified HC bulbs and their contacts. To compare the dendritic diameter profile around the bulbs with the one of random points on the dendrite (Figure 3C), we used the Vaa3D-Neuron2 auto-tracing to get a simplified representation of the HC morphologies from the volume reconstruction, consisting of a regularly spaced grid of nodes and with diameters. For each bulb position we identified the closest node and extracted the dendritic diameter profile around it. For a fair comparison to average points on the dendrite, we draw a random set of nodes with distributions of average distances from soma and tips matching the bulb locations.

To calculate the statistics of HC BC contacts at bulbs, we included only bipolar cells where the mean of the BC dendritic field lies within the dendritic field of at least one of the reconstructed HC. With this, the numbers in figures 4 C&D are a lower bound. For the HCs, additional contacts on branches ending outside the dataset are possible as well as contacts from BCs with soma outside of the dataset, especially for larger types such as CBC 8 and 9. The number of bulb contacts per BC are underestimated as well since the true coverage factor of HC dendrites lies at about 5-7 while we have only five overlapping cells in the center and coverage going down to one towards the edges of the dataset.

Horizontal cell injections and immunolabeling for GABA receptors and SNAP25

Horizontal cells were injected using Alexa Fluor 568 as described before (Meyer, Yadav, and Dedek 2018). In brief, cell nuclei in the retinal whole-mount preparation were visualized with DAPI labeling. Based on depth and size of the nuclei, horizontal cells were identified and thus injected with Alexa Fluor 568 and subsequently fixed using 4% paraformaldehyde. Retinal whole mounts were then incubated in primary antibodies, and immunolabeling for the GABA receptor subunit gamma 2 was carried as previously described (Ströh et al. 2013). Immunolabeling for SNAP25 was carried out using fixed 12 μm thick vertical retina sections using standard protocols with primary antibodies against SNAP25 and calbindin and secondary antibodies. All images were taken with a Leica TCS SP8 confocal microscope. Whole mount data was deconvolved with Huygens Essential software, using a theoretical point spread function.

Three-Dimensional Electron Microscopy using FIB-SEM

Focused ion beam - scanning electron microscopy (FIB-SEM tomography) allows efficient, complete, and automatic 3D reconstruction of horizontal cell dendrites with a resolution comparable to that of TEM (Xu et al. 2017; Bosch et al. 2015). An adult mouse (male, 14 weeks) was deeply anesthetized with isoflurane and decapitated before the eyes were dissected. All procedures were approved by the local animal care committee and were in accordance with the law for animal experiments issued by the German government (Tierschutzgesetz). The posterior eyecups were immersion fixed in a solution containing 0.1 M cacodylate buffer, 4% sucrose and 2% glutaraldehyde, and then rinsed in 0.15 M cacodylate buffer. A 1×1 mm² retina piece was stained in a solution containing 1% osmium tetroxide, 1.5% potassium ferrocyanide, and 0.15 M cacodylate buffer. The osmium stain was amplified with 1% thiocarbohydrazide and 2% osmium tetroxide. The retina was then stained with 2% aqueous uranyl acetate and lead aspartate. The tissue was dehydrated through an 70-100% ethanol series, transferred to propylene oxide, infiltrated with 50%/50% propylene oxide/Epon Hard, and then 100% Epon Hard. The Epon Hard block was hardened at 60°C.

Afterwards, the block was prepared for FIB-SEM tomography. The sample was trimmed using an ultramicrotome (Leica UC 7) and afterwards glued onto a special sample stub (caesar workshop) using conductive silver paint. To avoid charge artifacts, all surfaces of the block were sputter-coated with 30 nm AuPd (80/20). A focused ion dual beam (FIB) workstation (XB 1540, Carl Zeiss Microscopy, Oberkochen, Germany) was used for tomogram acquisition. This instrument uses a focused gallium ion beam that can mill the sample at an angle of 54° with respect to the electron beam. A digital 24-bit scan-generator (ATLAS5, Carl Zeiss) was used to control ion and electron beam. The sample was milled using an ion beam of 1nA at an energy of 30 kV. Images were collected at an energy of 2 kV using a pixel size of 5nm (x,y) and a layer thickness of 15 nm (z). Milling and imaging was performed simultaneously to compensate for charging effects.

The raw images were converted into an image stack, black areas were cropped, and the images were aligned using cross correlation (Mastrorade 1997).

Modelling

We built a biophysically realistic model of a HC dendritic branch using the simulation language NeuronC (Smith 1992). We used Vaa3D-Neuron2 auto-tracing to generate an .swc file from the volume reconstruction of one HC branch and manually refined it in Neuromantic. The model contains voltage-gated Ca²⁺ and K⁺ channels with different channel densities for proximal and distal dendrites and AMPA-type glutamate receptors at the cone synapses (Tab. 1). Photoreceptors are modelled as predefined in NeuronC with two compartments including voltage-gated Ca²⁺ and Ca²⁺-activated Cl⁻ channels. Cones were placed at the original positions with one synapse per invaginating HC dendritic tip found in the EM data. The synapses to the HC include postsynaptic AMPA channels modelled as Markov state-machines and include vesicle release noise. The model was stimulated for 60s with both

full-field and checkerboard noise with a temporal frequency of 2 Hz. The size of the checkerboard pixels was 5 μm such that all cones were stimulated independently. Voltage and Calcium signals were recorded in a dendritic tip below each of the 12 cones and in 14 bulbs identified along the dendrite.

Statistics

Error bars in all plots are 95% confidence intervals (CI) calculated as percentiles of the bootstrap distribution obtained via case resampling. In figure 2 B and C we fitted generalized additive models (R package *mgcv*, Wood 2017) with Poisson output distribution for skeleton tips (2B) and Gamma output distribution for contact area (2C). Both had a distance from soma as a smooth function and HC identity as smooth random effect.

Rm	[$\Omega \text{ cm}^2$]		2500
Ri	[$\Omega \text{ cm}$]		200
Channel densities			
L-type Ca^{2+} channels	[S/ cm^2]	Soma and proximal dendrites	3e-4
		Distal dendrites	1e-3
K^+ channels	[S/ cm^2]	Soma and proximal dendrites	1e-5
		Distal dendrites	1e-5

Table 1. Parameters of the biophysical model

References

- Behrens, Christian, Timm Schubert, Silke Haverkamp, Thomas Euler, and Philipp Berens. 2016. "Connectivity Map of Bipolar Cells and Photoreceptors in the Mouse Retina." *ELife* 5 (November): 065722. doi:10.7554/eLife.20041.
- Bosch, Carles, Albert Martí-nez, Nuria Masachs, Cátia M. Teixeira, Isabel Feraud, Fausto Ulloa, Esther Pérez-Martí-nez, et al. 2015. "FIB/SEM Technology and High-Throughput 3D Reconstruction of Dendritic Spines and Synapses in GFP-Labeled Adult-Generated Neurons." *Frontiers in Neuroanatomy* 9 (May). doi:10.3389/fnana.2015.00060.
- Cardin, Jessica A. 2018. "Inhibitory Interneurons Regulate Temporal Precision and Correlations in Cortical Circuits." *Trends in Neurosciences* 41 (10): 689–700. doi:10.1016/j.tins.2018.07.015.
- Chapot, Camille A., Christian Behrens, Luke E. Rogerson, Tom Baden, Sinziana Pop, Philipp Berens, Thomas Euler, and Timm Schubert. 2017. "Local Signals in Mouse Horizontal Cell Dendrites." *Current Biology* 27 (23). Elsevier Ltd.: 3603–3615.e5. doi:10.1016/j.cub.2017.10.050.
- Chapot, Camille A., Thomas Euler, and Timm Schubert. 2017. "How Do Horizontal Cells 'Talk' to Cone Photoreceptors? Different Levels of Complexity at the Cone–horizontal Cell Synapse." *Journal of Physiology* 595 (16): 5495–5506. doi:10.1113/JP274177.
- Demb, Jonathan B., and Joshua H. Singer. 2012. "Intrinsic Properties and Functional Circuitry of the AII Amacrine Cell." *Visual Neuroscience* 29 (01): 51–60. doi:10.1017/S0952523811000368.
- Dowling, J. E., and B. B. Boycott. 1966. "Organization of the Primate Retina: Electron Microscopy." *Proceedings of the Royal Society B: Biological Sciences* 166 (1002): 80–111. doi:10.1098/rspb.1966.0086.
- Drinneberg, Antonia, Felix Franke, Rei K Morikawa, Josephine Jüttner, Daniel Hillier, Peter Hantz, Andreas Hierlemann, Rava Azeredo da Silveira, and Botond Roska. 2018. "How Diverse Retinal Functions Arise from Feedback at the First Visual Synapse." *Neuron* 99 (1): 117–134.e11. doi:10.1016/j.neuron.2018.06.001.
- Duebel, Jens, Silke Haverkamp, Wolfram Schleich, Guoping Feng, George J. Augustine, Thomas Kuner, and Thomas Euler. 2006. "Two-Photon Imaging Reveals Somatodendritic Chloride Gradient in Retinal ON-Type Bipolar Cells Expressing the Biosensor Clomeleon." *Neuron* 49 (1): 81–94. doi:10.1016/j.neuron.2005.10.035.
- Euler, Thomas, Silke Haverkamp, Timm Schubert, and Tom Baden. 2014. "Retinal Bipolar Cells: Elementary Building Blocks of Vision." *Nature Reviews Neuroscience* 15 (8). Nature Publishing Group: 507–19. doi:10.1038/nrn3783.

- Franke, Katrin, Philipp Berens, Timm Schubert, Matthias Bethge, Thomas Euler, and Tom Baden. 2017. "Inhibition Decorrelates Visual Feature Representations in the Inner Retina." *Nature* 542 (7642). Nature Publishing Group: 439–44. doi:10.1038/nature21394.
- Hartveit, Espen. 1999. "Reciprocal Synaptic Interactions Between Rod Bipolar Cells and Amacrine Cells in the Rat Retina." *Journal of Neurophysiology* 81 (6): 2923–36. doi:10.1152/jn.1999.81.6.2923.
- Haverkamp, Silke, Ulrike Grünert, and Heinz Wässle. 2000. "The Cone Pedicle, a Complex Synapse in the Retina." *Neuron* 27 (1): 85–95. doi:10.1016/S0896-6273(00)00011-8.
- Haverkamp, Silke, and Heinz Wässle. 2000. "Immunocytochemical Analysis of the Mouse Retina." *The Journal of Comparative Neurology* 424 (1): 1–23. doi:10.1002/1096-9861(20000814)424:1<1::AID-CNE1>3.0.CO;2-V.
- Helmstaedter, Moritz, Kevin L Briggman, and Winfried Denk. 2011. "High-Accuracy Neurite Reconstruction for High-Throughput Neuroanatomy." *Nature Neuroscience* 14 (8). Nature Publishing Group: 1081–88. doi:10.1038/nn.2868.
- Helmstaedter, Moritz, Kevin L Briggman, Srinivas C Turaga, Viren Jain, H Sebastian Seung, and Winfried Denk. 2013. "Connectomic Reconstruction of the Inner Plexiform Layer in the Mouse Retina." *Nature* 500 (7461). Nature Publishing Group: 168–74. doi:10.1038/nature12346.
- Hirano, Arlene A., Johann Helmut Brandstätter, Catherine W. Morgans, and Nicholas C. Brecha. 2011. "SNAP25 Expression in Mammalian Retinal Horizontal Cells." *The Journal of Comparative Neurology* 519 (5): 972–88. doi:10.1002/cne.22562.
- Jackman, Skyler L., Norbert Babai, James J. Chambers, Wallace B. Thoreson, and Richard H. Kramer. 2011. "A Positive Feedback Synapse from Retinal Horizontal Cells to Cone Photoreceptors." *PLoS Biology* 9 (5). doi:10.1371/journal.pbio.1001057.
- Kamermans, Maarten, Iris Fahrenfort, Konrad Schultz, Ulrike Janssen-Bienhold, Trijntje Sjoerdsma, and Reto Weiler. 2001. "Hemichannel-Mediated Inhibition in the Outer Retina." *Science* 292 (5519): 1178–80. doi:10.1126/science.1060101.
- Kemmler, Robin, Konrad Schultz, Karin Dedek, Thomas Euler, and Timm Schubert. 2014. "Differential Regulation of Cone Calcium Signals by Different Horizontal Cell Feedback Mechanisms in the Mouse Retina." *Journal of Neuroscience* 34 (35): 11826–43. doi:10.1523/JNEUROSCI.0272-14.2014.
- Lee, Seunghoon, Yi Zhang, Minggang Chen, and Z. Jimmy Zhou. 2016. "Segregated Glycine-Glutamate Co-Transmission from VGlut3 Amacrine Cells to Contrast-Suppressed and Contrast-

Manuscripts

- Enhanced Retinal Circuits.” *Neuron* 90 (1). Elsevier Inc.: 27–34.
doi:10.1016/j.neuron.2016.02.023.
- Liu, Xue, Arlene A. Hirano, Xiaoping Sun, Nicholas C. Brecha, and Steven Barnes. 2013. “Calcium Channels in Rat Horizontal Cells Regulate Feedback Inhibition of Photoreceptors through an Unconventional GABA- and PH-Sensitive Mechanism.” *The Journal of Physiology* 591 (13): 3309–24. doi:10.1113/jphysiol.2012.248179.
- Masland, Richard H. 2012. “The Tasks of Amacrine Cells.” *Visual Neuroscience* 29 (01): 3–9.
doi:10.1017/S0952523811000344.
- Mastrorarde, David N. 1997. “Dual-Axis Tomography: An Approach with Alignment Methods That Preserve Resolution.” *Journal of Structural Biology* 120 (3): 343–52.
doi:10.1006/jsbi.1997.3919.
- Meyer, Arndt, Shubhash Chandra Yadav, and Karin Dedek. 2018. “Phenotyping of Gap-Junctional Coupling in the Mouse Retina.” In *Mouse Retinal Phenotyping. Methods in Molecular Biology*, edited by N Tanimoto, 1753:249–59. Humana Press, New York, NY. doi:10.1007/978-1-4939-7720-8_17.
- Münch, Thomas A., Rava Azeredo Da Silveira, Sandra Siebert, Tim James Viney, Gautam B. Awatramani, and Botond Roska. 2009. “Approach Sensitivity in the Retina Processed by a Multifunctional Neural Circuit.” *Nature Neuroscience* 12 (10). Nature Publishing Group: 1308–16. doi:10.1038/nn.2389.
- Schubert, Timm, and Thomas Euler. 2010. “Retinal Processing: Global Players Like It Local.” *Current Biology* 20 (11): R486–88. doi:10.1016/j.cub.2010.04.034.
- Smith, Robert G. 1992. “NeuronC: A Computational Language for Investigating Functional Architecture of Neural Circuits.” *Journal of Neuroscience Methods* 43 (2–3): 83–108.
doi:10.1016/0165-0270(92)90019-A.
- Ströh, Sebastian, Stephan Sonntag, Ulrike Janssen-Bienhold, Konrad Schultz, Kerstin Cimiotti, Reto Weiler, Klaus Willecke, and Karin Dedek. 2013. “Cell-Specific Cre Recombinase Expression Allows Selective Ablation of Glutamate Receptors from Mouse Horizontal Cells.” *PLoS ONE* 8 (12): 15–17. doi:10.1371/journal.pone.0083076.
- Taylor, W. Rowland, and Robert G. Smith. 2012. “The Role of Starburst Amacrine Cells in Visual Signal Processing.” *Visual Neuroscience* 29 (01): 73–81. doi:10.1017/S0952523811000393.
- Thoreson, Wallace B., and Stuart C. Mangel. 2012. “Lateral Interactions in the Outer Retina.” *Progress in Retinal and Eye Research* 31 (5). Elsevier Ltd: 407–41.

doi:10.1016/j.preteyeres.2012.04.003.

Tien, Nai Wen, Tahnbee Kim, and Daniel Kerschensteiner. 2016. "Target-Specific Glycinergic Transmission from VGluT3-Expressing Amacrine Cells Shapes Suppressive Contrast Responses in the Retina." *Cell Reports* 15 (7). The Authors: 1369–75. doi:10.1016/j.celrep.2016.04.025.

Turrigiano, Gina. 2011. "Stabilizing Neuronal Function Homeostatic Synaptic Plasticity: Local and Global Mechanisms for Homeostatic Synaptic Plasticity: Local and Global Mechanisms for Stabilizing Neuronal Function." *Cold Spring Harb Perspect Biol*, 1–18.
doi:10.1101/cshperspect.a005736.

Vroman, Rozan, Lauw J. Klaassen, Marcus H.C. Howlett, Valentina Cenedese, Jan Klooster, Trijntje Sjoerdsma, and Maarten Kamermans. 2014. "Extracellular ATP Hydrolysis Inhibits Synaptic Transmission by Increasing PH Buffering in the Synaptic Cleft." *PLoS Biology* 12 (5).
doi:10.1371/journal.pbio.1001864.

Wood, Simon N. 2017. *Generalized Additive Models: An Introduction with R, Second Edition*. 2nd ed. Chapman and Hall/CRC.

Xu, C. Shan, Kenneth J. Hayworth, Zhiyuan Lu, Patricia Grob, Ahmed M. Hassan, José G. García-Cerdán, Krishna K. Niyogi, Eva Nogales, Richard J. Weinberg, and Harald F. Hess. 2017. "Enhanced FIB-SEM Systems for Large-Volume 3D Imaging." *ELife* 6: 1–36.
doi:10.7554/eLife.25916.

Yang, XL, and SM Wu. 1991. "Feedforward Lateral Inhibition in Retinal Bipolar Cells: Input-Output Relation of the Horizontal Cell-Depolarizing Bipolar Cell Synapse." *Pnas* 88 (8): 3310–13.
doi:10.1073/pnas.88.8.3310.

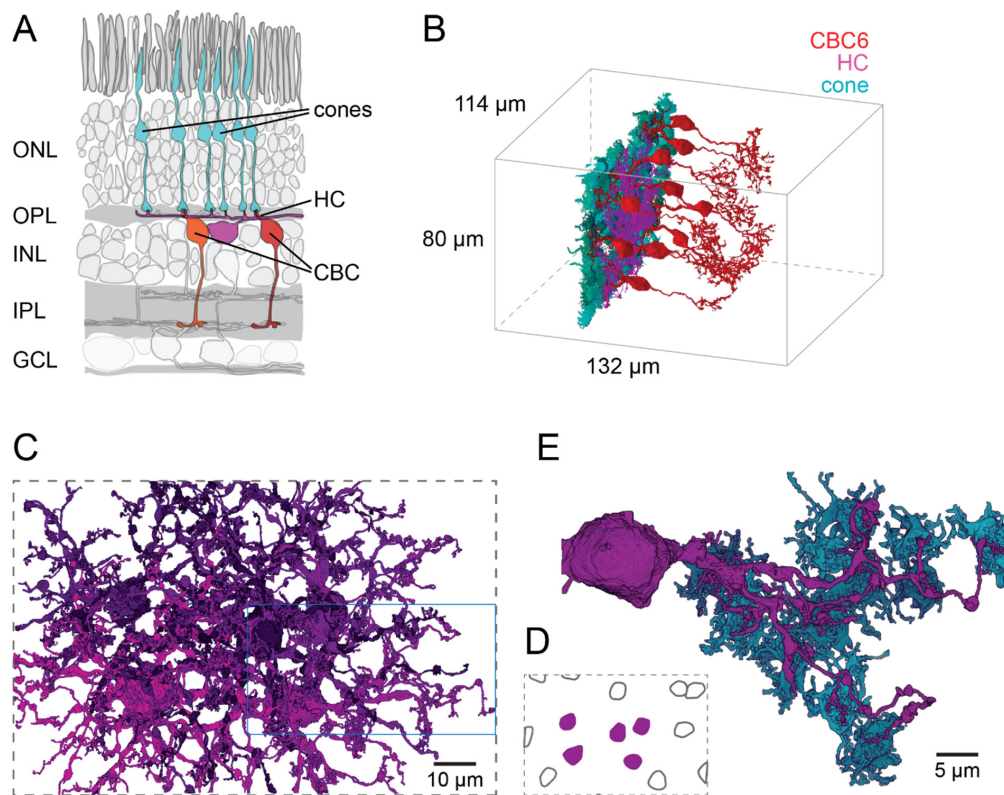


Figure 1. Horizontal cell reconstruction. (A) Schematic of a vertical section through the mouse retina showing the reconstructed cell types. (B) Outlines of the dataset with volume reconstructed cones, one HC and several CBC6 (X/Y in total). (C) Volume reconstructions of five HCs, blue rectangle: location of dendrite shown in (E). (D) Soma locations of five reconstructed (magenta) and 11 unreconstructed (black outline) HCs. (E) Volume reconstruction of an HC branch (magenta) with contacted cones (cyan).

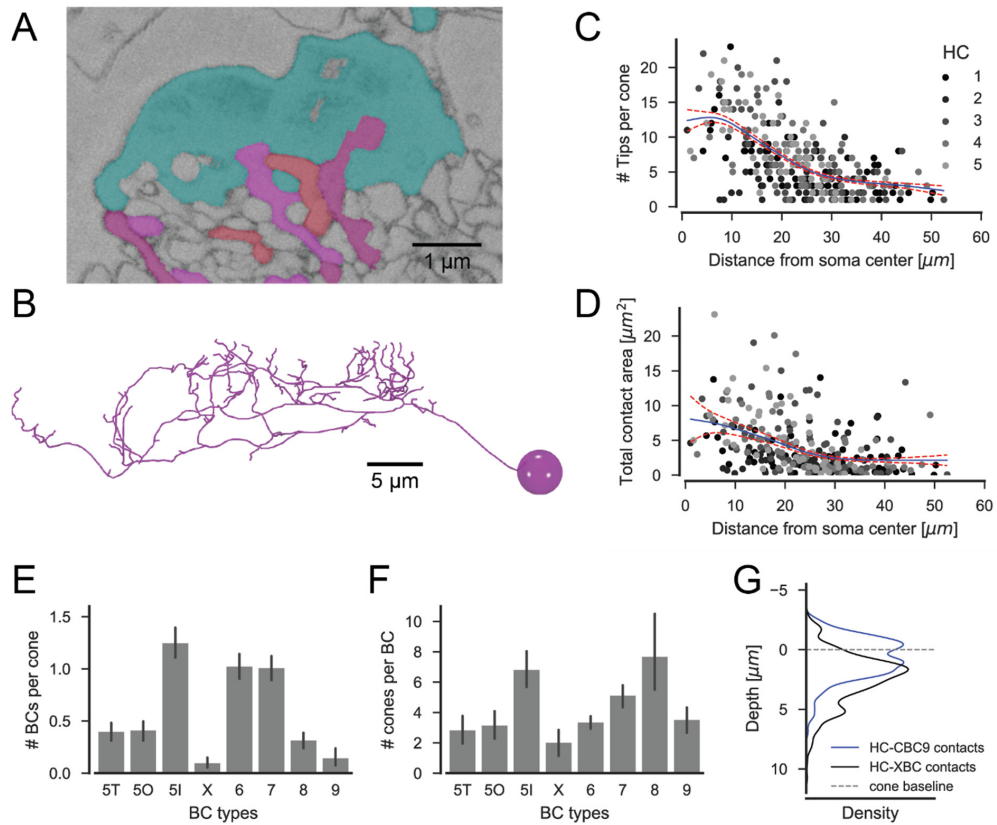


Figure 2. Horizontal cell – to - cone contacts (A) EM slice showing a cone pedicle (cyan) with invaginating contact from an ON-CBC (red) and a HC (magenta). (B) Skeleton model of the HC branch from fig. 1 (D) showing the increase of the number of dendritic tips towards the soma. (C) HC skeleton tips per contacted cone vs. distance from HC soma. Blue: Poisson GAM fit with confidence interval (red). (D) Contact area between HC and cone pedicle volume reconstructions per cone vs. distance from HC soma. Blue: Gamma GAM fit with confidence interval (red). (E) Number of BCs contacting each cone per type. (F) Number of cones contacted per ON-CBC type. Data from Behrens et al. 2016. Error bars show 95% CI. (G) Depths location of volume contacts between HC and CBC9 compared to HC-CBCX contacts.

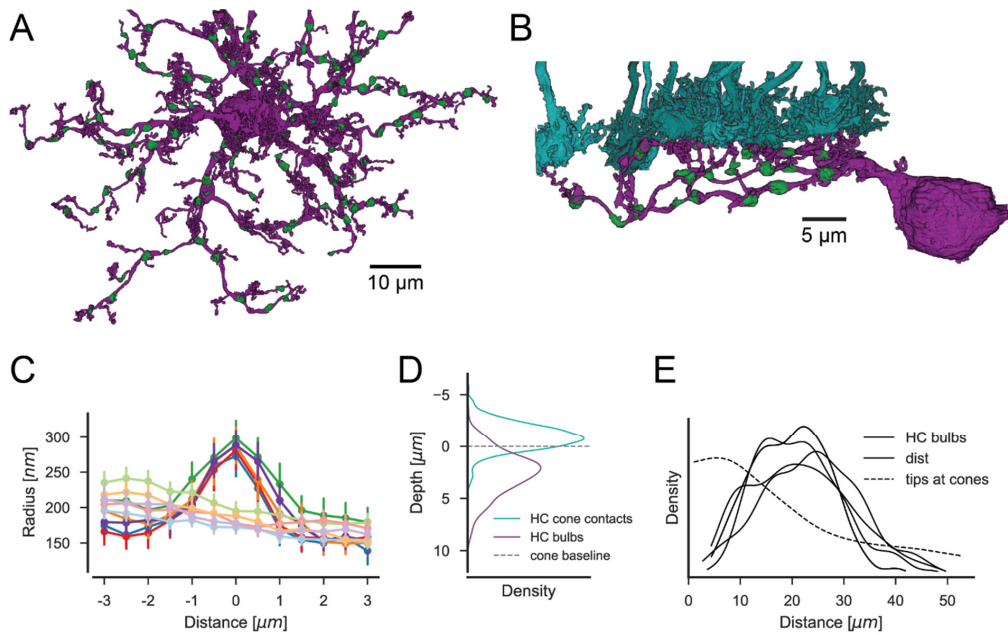


Figure 3. Identification of bulbs in horizontal cells. (A) Top view of a reconstructed HC with bulbs highlighted in green. (B) Side view of a branch from the same HC with bulbs (green). (C) Dendritic radius profile at bulb locations (high saturation) compared to randomized points on the dendrites (low saturation) with matching distribution of distances from soma and tips. (D) Depth of bulbs compared to HC cone contacts. (E) Distance distribution of bulbs relative to the soma. Dashed line: Model fit showing distribution of HC skeleton tips at cones from fig. 2 (C).

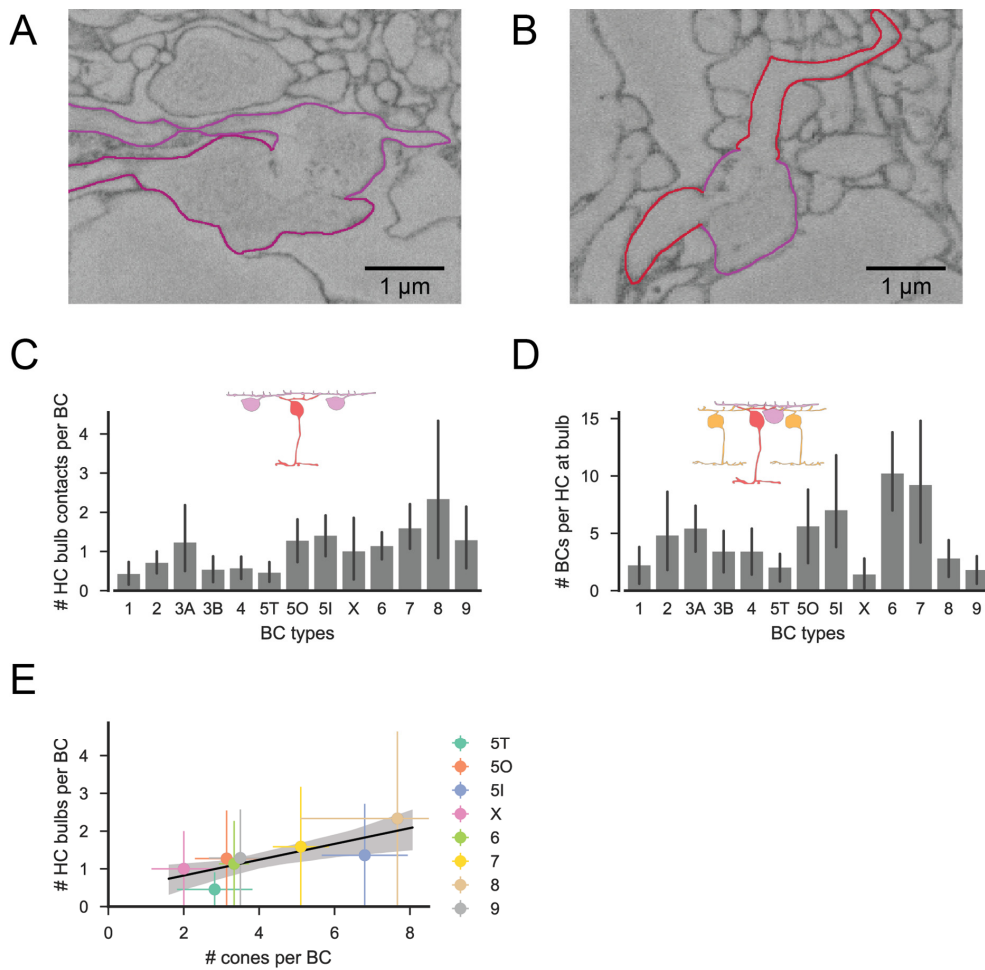


Figure 4. Bulb contacts with other neurons. (A) EM slice showing bulb contact between two HCs. (B) Bulb contact between HC (magenta) and BC (red). (C) Bulb contacts per BC for all CBC types. (D) BCs contacted by bulbs per HC for all CBC types. (E) Bulb contacts vs. contacted cones for all ON-CBC types (data from (C) and fig. 2 (D)) with linear regression. All error bars show 95% CIs.

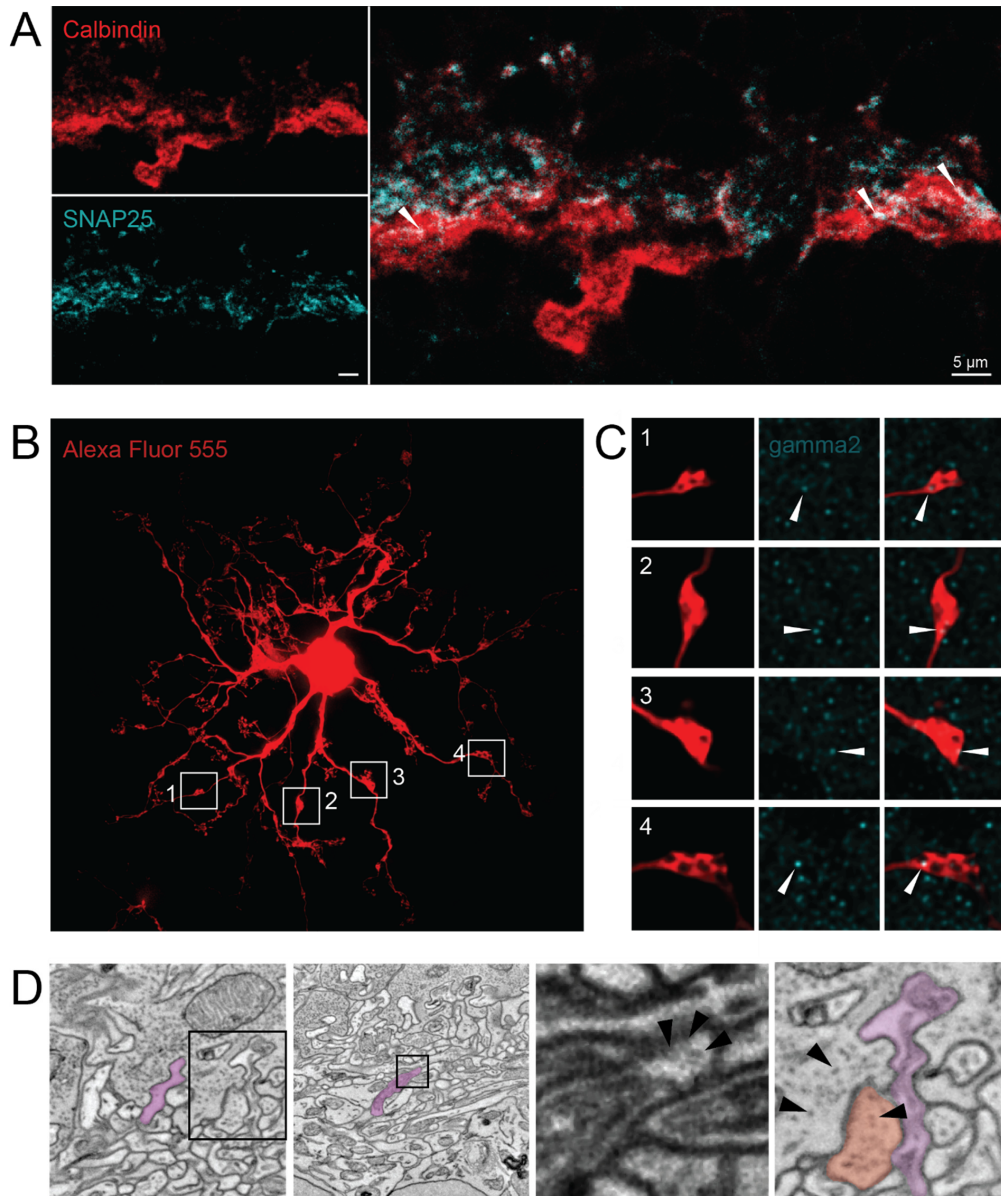


Figure 5. Synaptic structures at horizontal cell bulb contacts. (A) Calbindin labeled horizontal cells with SNAP25 immunolabeling in vertical retinal section. Arrowheads indicate co-localization on primary dendrites. (B) Alexa Fluor 565-injected horizontal cells with identified bulbs (white boxes). (C) Enlarged bulbs (red) from boxes in (B) with GABA receptor gamma2 immunolabelling (cyan). Arrowheads indicate co-localization. (D) Electron microscopy image showing traced horizontal cell (magenta) invaginating in cone axon terminal (far left), the dendritic network below cone axon terminal with horizontal cell bulb of the same cell (middle left), enlarged crop of the HC bulb with putative synaptic vesicles indicated by arrowheads (middle right, contrast enhanced) and enlarged crop showing clearly visible glutamatergic vesicles (arrowheads) in the cone axon terminal and a bipolar cell (red) but not in HC dendritic tips (magenta) (far right). Boxes on the left indicate positions of crops on the right.

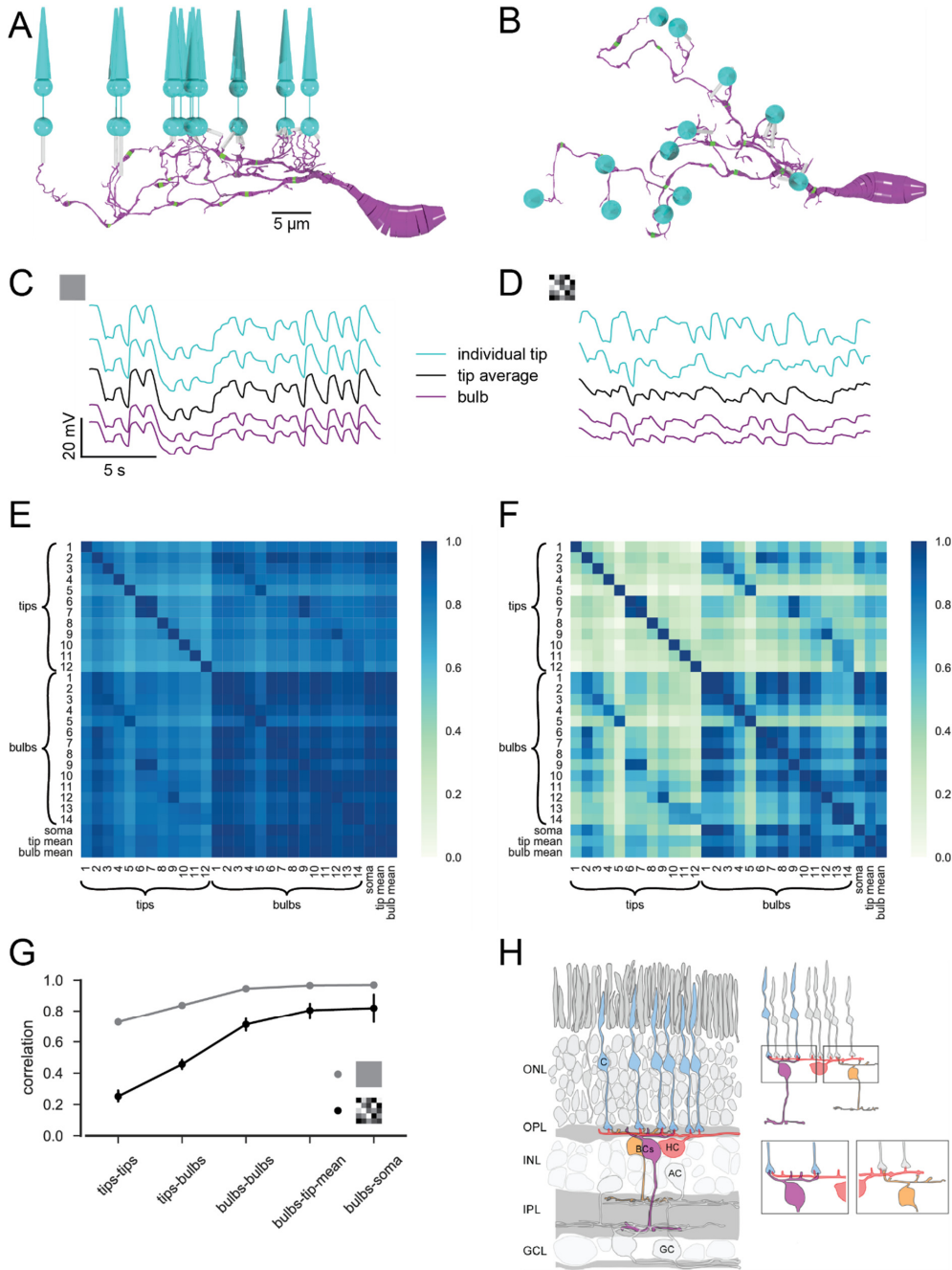


Figure 6. Biophysical modelling. (A) Side and (B) top view of the modelled HC dendrite with bulbs (green) and cones. (C) & (D) Example voltage traces recorded at dendritic tips below cones, at bulbs and average over all tips for (C) a full-field noise stimulus and (D) a checkerboard noise stimulus without internal noise. (E) & (F) Correlations from 60s of (E) full-field and (F) checkerboard stimulation including synaptic vesicle release noise. (G) Mean correlations between different tips, between tips and bulbs, between different bulbs, bulbs and the tip mean and bulbs and the soma for both stimuli. (H) Overview over different HC output sites.

Acknowledgements

Thanks

Philipp Berens, Thomas Euler, Timm Schubert, Luke E. Rogerson, Camille A. Chapot, Yue Zhang, Silke Haverkamp, Karin Dedek and all colleagues from the Berens, Euler and Bethge Labs, Moritz Helmstaedter and co-authors (2013) for making the EM dataset e2006 publicly available, the Graduate Training Center of Neuroscience of the University of Tübingen, and finally Simone Mölbert, my family and friends for your support during all stages of this dissertation project.